Pacific Northwest
NATIONAL LABORATORY

PNNL-34177

Model Advancements to Enable Impact Analysis of Climate Change on Streamflow Temperature

December 2022

Mark Wigmosta
Zhuoran Duan
William Perkins
Marshall Richmond
Brian Bellgraph
Xiaodong Chen
Lai-Yung Leung

U.S. DEPARTMENT OF ENERGY

Prepared for the U.S. Department of Energy
under Contract DE-AC05-76RL01830

PNNL-34177

Model Advancements to Enable Impact Analysis of Climate Change on Streamflow Temperature

December 2022

Mark Wigmosta
Zhuoran Duan
William Perkins
Marshall Richmond
Brian Bellgraph
Xiaodong Chen
Lai-Yung Leung

Prepared for
the U.S. Department of Energy
under Contract DE-AC05-76RL01830

Pacific Northwest National Laboratory
Richland, Washington 99354

PACIFIC NORTHWEST NATIONAL LABORATORY
operated by
BATTELLE
for the
UNITED STATES DEPARTMENT OF ENERGY
under Contract DE-AC05-76RL01830

Printed in the United States of America

Available to DOE and DOE contractors from
the Office of Scientific and Technical
Information,
P.O. Box 62, Oak Ridge, TN 37831-0062
www.osti.gov
ph: (865) 576-8401
fox: (865) 576-5728
email: reports@osti.gov

Available to the public from the National Technical Information Service
5301 Shawnee Rd., Alexandria, VA 22312
ph: (800) 553-NTIS (6847)
or (703) 605-6000
email: info@ntis.gov
Online ordering: http://www.ntis.gov

Abstract

With support from the Department of Energy's Water Power Technologies Office, Pacific Northwest National Laboratory (PNNL) has developed new tools that incorporate cutting-edge climate and hydrological science capabilities to assess the potential long-term impacts of future climate conditions on unregulated streamflow and water temperature within watershed-river-reservoir systems. The objectives of this project were achieved by enhancing key hydrologic and hydrodynamic models and transferring them to a high-performance computing environment to provide a high-spatiotemporal resolution, multi-scale modeling framework. The new modeling framework has the potential to quantify risks related to climate change impacts on runoff, unregulated streamflow, and water temperature. Initial development and demonstration of the modeling framework was conducted under historical and future climate conditions in the Columbia River Basin in the Pacific Northwest and the Connecticut River Basin in New England.

Executive Summary

With support from the Department of Energy's Water Power Technologies Office, Pacific Northwest National Laboratory (PNNL) has developed new tools that incorporate cutting-edge climate and hydrological science capabilities and tested them in two basins (i.e., the Columbia River Basin and the Connecticut River Basin) as a first step in modeling climate change impacts on runoff, unregulated streamflow, and water temperature at large, basin scales.

The research outlined in this report aims to advance climate science and numerical modeling methods and demonstrate new capabilities to assess the potential impacts of future climate conditions on streamflow and water temperature within watershed-river-reservoir systems. The objectives of this project were achieved by:

1. Modelling historical and future climate conditions to better understand the occurrence of extreme precipitation, including atmospheric rivers (ARs) in the Pacific Northwest, and integrating this into watershed-river models.

2. Advancing fine resolution, physics-based hydrologic models to allow detailed representation of small-scale hydrologic processes over large basins using decades long simulations.

3. Improving simulation of flow routing and stream temperature by integrating hydrologic and hydrodynamic models into a high-spatiotemporal resolution, multi-scale modeling framework.

4. Applying the above framework of future climate conditions and extreme precipitation to high-resolution hydrologic models and stream temperature models in the Columbia River Basin in the Pacific Northwest.

5. Applying a similar framework to evaluate the impacts of climate change on streamflow and water temperature in the Connecticut River Basin in New England.

Developing and leveraging the tools, like those developed in this report, in partnership with water managers, regulators, hydropower operators, and other stakeholders is key to understanding how ecological stressors across river basins may change over time and to ensuring that decisions around future water resource management are made with the best available information. High-performance computing environments, state of the art global climate simulations, and cutting-edge models developed for this project provide an example of capabilities and outline areas of future collaboration with potential end-users. These end-users are essential in providing local perspectives of unique river systems that support the application, refinement, and specification of these tools.

In this report, Section 2 examines future precipitation extremes driven by atmospheric rivers, a climatic phenomenon not considered in many studies. Understanding how precipitation and temperature changes impact river systems requires fine-scale hydrologic models, so Section 3 describes advancements made to the Distributed Hydrology Soil Vegetation Model, a PNNL-developed hydrologic model, that enables simulation of changing streamflow at small spatial scales across large river basins. A description of how this hydrologic model is linked to high-resolution hydrodynamic models that simulate water quality parameters like temperature is described in Section 4. The full framework was then tested in the Columbia River Basin (Section

5) where ARs are becoming increasingly common and in the Connecticut River Basin (Section 6). A summary of the report findings is provided below.

Impacts of Atmospheric Rivers on the Columbia River Basin

Heavy precipitation, intense snow melting, and flooding are among the most significant hydrological extremes in the western United States, and they cause huge societal and economic losses every year. Many of these extreme events are caused by or related to atmospheric rivers (ARs), which have rarely been included in studies of future climate impacts on hydrology. We used the Weather Research Forecasting (WRF) model to examine the physical mechanism responsible for these extreme events and their hydrologic impacts in the western United States. The WRF model is used to dynamically downscale scenarios from five global climate models (GCMs) for the present (1981–2015) and future (2041–2070) at 6 km grid spacing across the western United States.

In the first application, ARs were identified by the Atmospheric River Tracking Method Intercomparison Project (O'Brien, 2021) and precipitation was taken from a high-resolution regional climate simulation. We found the following:

- Extreme precipitation amount in West Coast watersheds is closely related to AR intensity and the relationship between ARs and precipitation is most significant in the Pacific Northwest and California.

- ARs explain 30% to 60% of the variability of annual total runoff and sharpen the seasonality of water resource availability in West Coast mountain watersheds. They can significantly control surface hydrological processes through the extreme precipitation they produce.

In the second application, the WRF model output for historical and future climate was bias-corrected and then used to evaluate changes in unregulated streamflow and water temperature in the Columbia River Basin.

- We found that the WRF future precipitation generally exceeds historical levels with more variation in December and January, while future air temperature exceeds historical levels in all months, by 3–5 degrees depending on the season and GCM.

Enhancing the Modeling Framework for the Columbia River Basin

The Distributed Hydrology Soil Vegetation Model (DHSVM) and the Modular Aquatic Simulation System 1D (MASS1) hydrodynamic model are key components of the modeling framework and provide information at much finer spatial scales (i.e., 90 m and channel reach) than the larger scale WRF analysis, but they are computationally intensive to run over large river basins. To allow for ultra-high-resolution simulation of watershed processes in large basins like that of the Columbia River, the DHSVM code was parallelized for distributed memory computers. Parallel code speedup was significant and run times for 1-year simulations were reduced by up to two orders of magnitude (10^2). This version of DHSVM is currently being used by several major universities and a National Laboratory.

MASS1 was also added to DHSVM, bringing full hydrodynamic routing and stream temperature simulation to the integrated model. In smaller tributaries, near stream vegetation strongly influences stream temperature by shading the channel, but most hydrodynamic river models ignore this effect on small streams. This effort linking MASS1 to DHSVM represents a significant advancement in modeling flow and vegetation effects on stream temperature and provides a seamless capability for analysis over a range of spatial scales.

Impacts of Climate Change in the Columbia River Basin

The full modeling framework described above was tested in the Columbia River Basin at 90 m spatial resolution to examine the impacts of climate change on **unregulated** flows. In the Columbia River Basin, projected future climate scenarios (2041-2070) included the effects of atmospheric rivers and resulted in the following observations:

- Earlier snowmelt resulting in higher unregulated winter and early spring flows and reduced summer flows. Higher January through April flows could generate more hydropower and produce more spill but production during the summer could decline at the same time increased temperatures drive greater summer power use.

- A one month earlier shift in the timing of the peak inflow was observed in some subbasins. This increase in cool-season system inflow to reservoirs will likely lead to an increase in typical cool-season water storage. However, reduced inflow during the warm season may lead to a greater reliance on stored water resulting in a decline in end-of-month water storage volumes by the end of the summer.

- Water temperature in the Columbia River Basin is generally increased under the future climate conditions throughout the year at most locations. The greatest increase typically occurs in August and ranges between 1 and 3ºC depending on location.

Impacts of Climate Change in the Connecticut River Basin

In the Connecticut River Basin, the downscaled projections of climate for the 2040–2070 period shows generally higher precipitation across the basin, while air temperature increases by 2–5ºC depending on location and GCMs. This resulted in the following impacts on **unregulated** flow and water resources:

- Unregulated winter flows in the Connecticut River Basin were generally increased under future climate conditions, while the flow is reduced in the spring.

- The seasonal peak flow occurs earlier and is reduced in the future.

- Water temperature is increased under the future climate conditions throughout the year at most locations. The greatest increase occurs in August and typically ranges between 3 and 5ºC depending on location but increases up to 6 degrees were simulated.

Acknowledgments

This study was supported by the U.S. Department of Energy, Office of Energy Efficiency and Renewable Energy (EERE), Water Power Technologies Office (WPTO). The authors wish to acknowledge the following WPTO staff who provided constructive comments for improving the Report: Charles Scaife, Simon Gore, and Hoyt Battey.

Acronyms and Abbreviations

API	application programming interface
AR	atmospheric river
AR6	Sixth Assessment Report
BCSD	bias-correct spatial downscaling
CDF	cumulative distribution function
CMIP5	Model Intercomparison Project Phase 5
CONUS	conterminous United States
CR	channel routing
CRUISE	Connecticut River UnImpacted Streamflow Estimator
DEM	digital elevation model
DHSVM	Distributed Hydrology Soil Vegetation Model
DOE	U.S. Department of Energy
EERE	Energy Efficiency and Renewable Energy
EPRI	Electric Power Research Institute
ET	evapotranspiration
EWB	energy/water balance
GA	Global Arrays
GCM	global climate model
GHG	greenhouse gas
GIS	geographic information system
GSS	Gilbert Skill Scores
HUC	hydrologic unit code
IDA	intensity-duration-area
I/O	input/output
IPCC	Intergovernmental Panel on Climate Change
JPL	Jet Propulsion Laboratory
LIDAR	Light Detection and Ranging
LPI	local partial inertia
MACA	Multivariate Adaptive Constructed Analogs
MASS1	Modular Aquatic Simulation System 1D
MIMD	multiple instruction, multiple data
MPI	Message Passing Interface
NARCCAP	North American Regional Climate Change Assessment Program
NASA	National Atmospheric and Space Administration
NRNI	No Regulation-No Irrigation
NSE	Nash-Sutcliffe model Efficiency coefficient

PGAS	partitioned global address space
R&D	research and development
RC	regional climate model
RCP	Representative Concentration Pathway
ROS	rain-on-snow
SHEDS	Spatial Hydro-Ecological Decision System
SR	surface routing
SSR	subsurface and surface routing
SSURGO	Soil Survey Geographic Database S
SWE	snow water equivalent
TSI	time-step initialization
TVD	total variation diminishing
USGS	U.S. Geological Survey
WPTO	Water Power Technologies Office
WRF	Weather Research Forecasting
WY	water year

Contents

Figures

Tables

1.0 Introduction

Understanding the effects of future climates on water availability and quality, and how those variables could inform activities like water resource management, long-term hydropower planning, new infrastructure investment and upgrades, and the management of environmental resources is essential to ensuring the continued viability of our power and water systems and the sustainability of our riverine environments. Where studies like the U.S. Department of Energy’s (DOE’s) Secure Water Act 9505 (DOE 2013, 2017) and the Bureau of Reclamation’s (Reclamation) 9503 (Reclamation 2011) focused on water availability, this Pacific Northwest National Laboratory (PNNL) project examines water temperature, which is a key indicator of water quality. Implementing a watershed scale approach, as done in this study, rather than site-specific stream temperature assessments recognizes ecology as an interconnected system through the river network and aims to promote an integrated water-river-reservoir assessment and management of resources.

1.1 Objectives

The goal of this research is to model the impacts of climate change on streamflow and water temperature across two large basins to test a tool for better understanding future water reliability. This goal was achieved by enhancing key existing fine resolution hydrology and stream temperature models and transferring them to a high-performance computing environment to provide a high-spatiotemporal resolution, multi-scale modeling framework. This was accomplished through five main objectives:

1. Model historical and future climate conditions using the Weather Research and Forecasting (WRF) model for dynamical downscaling applied to a multi-model general circulation model (GCM) ensemble to: 1) better understand and help predict the occurrence of extreme precipitation and hydrologic impacts associated with Atmospheric Rivers (ARs) in the western United States; and 2) drive the integrated watershed-river model in the Columbia River Basin (Section 2.0).

2. Advance the use of physics-based, fine resolution hydrologic models through the parallelization of the Distributed Hydrology Soil Vegetation Model (DHSVM) allowing detailed representation of critical small scale hydrologic processes over relatively large basins using decades long simulations (Section 3.0).

3. Improve high-resolution simulation of channel routing and stream temperature through the integration of DHSVM and the Modular Aquatic Simulation System 1D (MASS1) hydrodynamic model to complete a high-spatiotemporal resolution, multi-scale modeling framework (Section 4.0).

4. Apply the analysis framework that includes extreme events, fine resolution hydrologic models, and high-resolution routing of stream temperature to evaluate the impacts of climate change on unregulated streamflow and water temperature in the Columbia River Basin in the Pacific Northwest (Section 5.0).

5. Apply a similar analysis framework to evaluate the impacts of climate change on unregulated streamflow and water temperature in the Connecticut River Basin in New England (Section 6.0).

The resulting modeling and analysis framework is a first step in developing tools that quantify the impacts of altered climate on runoff, streamflow, and water temperature. Future studies should apply these findings to explicitly enhance our understanding of climate-induced risks to integrated water and power systems.

1.1.1 Synergistic Activities

The objectives of this project support two ongoing initiatives at DOE's Water Power Technologies Office (WPTO). The first initiative focuses on WPTO's ecological aims as reflected in the Environmental R&D and Hydrologic Systems Science strategic objectives:

- Develop technologies and strategies that avoid, minimize, or mitigate ecological impacts.
- Assess the potential impacts of long-term hydrologic variations on hydropower generation and flexibility.
- Better identify opportunities and weigh potential tradeoffs across multiple objectives at basin scales.

Second, the objectives of this project are reflected in WPTO's HydroWIRES initiative, particularly Area 3 to "develop operational strategies and associated tools that enable hydropower to better optimize its operations to support evolving grid needs" and "quantify hydropower plant- and fleet-level contributions to system-level water availability, environmental flows, and other non-power but system-level goals." This project addresses several HydroWIRES roadmap Domains including:

- Domain 2: Capabilities and Constraints
  - 2.3: Advance hydrologic forecasting (water as fuel) at intervals and horizons that facilitate planning and dispatch through high-spatiotemporal hydrologic modeling. Computational advances made under this project provide a computational platform for high spatial (30–90 m) and temporal (hourly or sub-hourly) hydrologic forecasting. Of particular importance is the ability for data assimilation of evolving remotely sensed products, such as (30 m) Light Detection and Ranging (LIDAR) estimates of snow depth, at their native scale without having to aggregate and lose important spatial information.
- Domain 3: Operations and Planning
  - 3.3: Advance hydropower optimization across fleet and plant operations and planning practices by considering multiple objects (power, flow, and water temperature) at the plant and system scales.

1.2 Background

The Columbia River and Connecticut River Basins are two of the most hydrodynamically controlled river basins in the United States. Both contain a series of hydroelectric and non-powered dams that control and affect water volume and water quality characteristics throughout their watersheds. Consequently, the water, electricity, and ecosystem services that these river networks provide will be challenged as climate change is predicted to cause large changes in the timing and volume of water availability over the next hundred years resulting in a need to understand the flow dynamics more precisely within these basins.

In the Columbia River Basin of the Pacific Northwest, about 40% of the nation's total hydropower generation is already facing water quality adaptation issues due to changing climate. The summer of 2015 in the Columbia River Basin may serve as a preview of the impacts these changes could have on critical ecosystems.[1] In the summer of 2015, water temperatures in many locations throughout the mainstem and major tributaries were physiologically unsustainable for salmon, resulting in the death of a quarter million sockeye salmon.[2] Annual direct and indirect spending on salmon recovery in the Columbia Basin is at least $1.25 Billion per year (Rice 2019) and future investments are expected based on the ongoing need to manage ecosystem services in coordination with water users and the hydropower system under the Federal Power Act (U.S. Congress 1940). These investments in ecosystem service management may see their expected benefits at stake under current climate projections of the Pacific Northwest. Increases in average annual temperature of 0.1ºC to 0.6ºC per decade (Mote and Salathe 2010) coupled with reductions in snowpack (up to −65%; Elsner et al. 2010) and glacial volume are expected over the next 50 to 70 years.

Changes in the seasonality of precipitation as well as the form in which it falls (rain or snow) may also significantly affect human infrastructure in the Columbia Basin. Tohver et al. (2014) predict that the size of the 100-year floodplain will increase by 10 to 70% in many portions of the river by the year 2080, which would pose problems for metropolitan areas within the floodplain including the Tri-Cities (Richland, Kennewick, and Pasco) of Washington State as well as Hood River and Portland, Oregon metro areas. Understanding the impact of the potential increase in flooding events on our human-ecosystem infrastructure, and how water storage and hydroelectric power in the Columbia Basin can be managed to withstand these future flooding events, is one important benefit of higher quality water modeling tools.

In the Connecticut River Basin of the northeast United States, the projected future climate includes a shift to more rainfall during winter, earlier snowmelt, increased precipitation intensity with more flooding potential and earlier dates of peak discharges (Parr et al. 2015). Similar to the Columbia River, these changes in the timing, quantity, and quality (e.g., temperature) of the Connecticut River and its tributaries will result in changes in the timing of aquatic species life cycles. Consequently, water resources in the basin will need to be adaptively managed to meet ecosystem and other water needs in the basin (Kennedy et al. 2018). Several ongoing efforts in the Connecticut River Basin are focusing on developing more flexible hydropower operating regimes so that the basin can adapt to a changing climate (Julian et al. 2015; Kennedy et al. 2018).

One potential response to the reduction in natural, cold water availability in the Columbia, Connecticut, and other basins in the United States is to manage the existing river-reservoir system in a manner in which control of temperature is a higher management objective. Two options are possible: (1) the existing system configuration can be managed for this objective and (2) structural modifications to the existing dams could be made to allow for controlled releases of cooler water from lower elevations within each reservoir. In addition, the potential new development of small/modular hydropower systems is likely to occur in small or upper watershed tributaries that could be disproportionally affected by changes in streamflow and water temperature due to climate change. New hydropower developments could enable alternative temperature management strategies, such as providing coordinated hypolimnetic releases in basin headwaters. Reservoirs created by new hydropower development could be used to mitigate climate change-induced stream warming by releasing cold water throughout the summer, while also providing a source of renewable energy.

[1] http://www.seattletimes.com/seattle-news/environment/last-years-heat-wave-doomed-nearly-all-okanogan-sockeye-salmon/

[2] http://www.nwcouncil.org/news/blog/drought-and-streamflow-research-may-2016/

The operational strategies described above require the ability to predict (under current and future climate) streamflow characteristics and water temperature from headwater tributaries through the mainstem. Informal interviews with end users (e.g., Seattle City Light, United States Bureau of Reclamation Central California Region) confirmed this, emphasizing that evaluation of water temperature at plant scale or within headwater tributaries requires finer spatial scale analysis than the 12–6 km typically used by semi-distributed hydrologic models (e.g., Variable Infiltration Capacity model; even larger for the Soil & Water Assessment Tool). The simple reality is that models and approaches developed for national-scale analysis are insufficient for decision-making at the plant scale in many locations.

The coarse modeling scale currently employed for national-scale assessments is inconsistent with current national data products such as 30 m digital elevation model (DEM), soils, and vegetation data required to represent key hydrologic processes at scales appropriate for this project. The structure and process representation in these models precludes the appropriate use of these current data products anywhere near their native scale; significant data aggregation is required for use by these models along with associated smoothing and loss of fidelity. This data/model discrepancy will increase dramatically as next-generation data come online. For example, some utilities in California are currently using ultra-high-resolution National Aeronautics and Space Administration Jet Propulsion Laboratory airborne snow data (3–50 m) to estimate snowpack water storage. In addition, current national-scale approaches to routing flow and computing water temperatures are insufficient for evaluating plant-scale operational and structural modifications at scales relevant for water quality analyses (e.g., 401 certification) and fish habitat at biologically relevant scales.

2.0 Impacts of Atmospheric Rivers in the Western United States

Before discussing the projected climate change impacts to runoff and streamflow in the Columbia River Basin, it is important to understand the physical-dynamical mechanisms responsible for these changes. Unique to this research effort, the regional dynamical WRF simulations provided the opportunity to illustrate and analyze the physical mechanisms responsible for extreme events at fine spatial resolution – a significant improvement on statistically downscaled GCM data which only provides information on a limited set of climate variables. Here we focused on investigating the impacts of ARs on extreme events because extreme precipitation is often associated with ARs in the western United States. Additional detail is provided in Chen et al. (2018, 2019).

2.1 Methods

2.1.1 Climate Modeling

Global climate models (GCMs) are the primary tools for understanding and projecting future climate under different greenhouse gas (GHG) emissions at the global scale, with their spatial resolutions constrained by computational resources. Hence, even for the Coupled Model Intercomparison Project Phase 5 (CMIP5) (Taylor et al. 2012) that provided climate change scenarios for the most recent Intergovernmental Panel on Climate Change (IPCC) Sixth Assessment Report (AR6), most GCMs were applied at a resolution between 1° to 2° latitude-longitude (~110-220km), which is not sufficient for resolving mesoscale features key to the generation of extreme precipitation. Two downscaling approaches were used here to develop regional climate change scenarios for assessing climate change impacts: statistical downscaling and dynamical downscaling. Because of the low computational cost, statistical downscaling approaches can be applied to a large ensemble of GCM projections to estimate uncertainty. However, they suffer from the inherent assumption of stationarity as statistical relationships developed from historical data are applied to future climates. In contrast, dynamical downscaling based on regional climate models (RCMs) is physically based but computationally demanding. Past efforts have mostly used a single RCM driven by a single GCM scenario, thereby limiting the evaluation of uncertainty. In this project, we took advantage of both approaches to project future climate change.

2.1.2 WRF Dynamical Downscaling

We used an RCM based on the WRF model (Chen et al. 2018) to dynamically downscale scenarios from North American Regional Reanalysis (NARR; Mesinger et al., 2006) for the present (1981–2015), and five GCMs selected from CMIP5 for the present (1981–2015) and future (2041–2070) across the western United States (Figure 2.1). Following the North American Regional Climate Change Assessment Program (Mearns et al. 2013), we included five GCMs in this project:

- the second-generation Canadian Earth System Model (*CanESM2*),
- the Community Earth System Model version 1 that includes the Community Atmospheric Model version 5 (*CESM1_CAM5*),
- the Geophysical Fluid Dynamics Laboratory Earth System Model Version 2M (*GFDL_ESM2M*),

- the Hadley Global Environment Model 2-Earth System (*HadGEM2_ES*), and
- the Max Planck Institute for Meteorology Earth System Model MR (*MPI_ESM_MR*).

The five GCMs selected represented a good diversity of models because their Earth system components generally followed different developmental paths and approaches. They were chosen based on the extensive evaluation of CMIP5 model performance for the historical simulations over the Pacific Northwest region (Rupp et al. 2013; Gao et al. 2015). For the mid-century time frame, uncertainty in climate projections due to emission scenarios is less important than uncertainty related to the use of different GCMs (Hawkins and Sutton 2009), so only the Representative Concentration Pathway mitigation scenario 8.5 (RCP8.5) was used in our modeling and analysis. The WRF simulations covered the western United States at about 6 km grid resolution to adequately resolve key regional forcing such as orography.

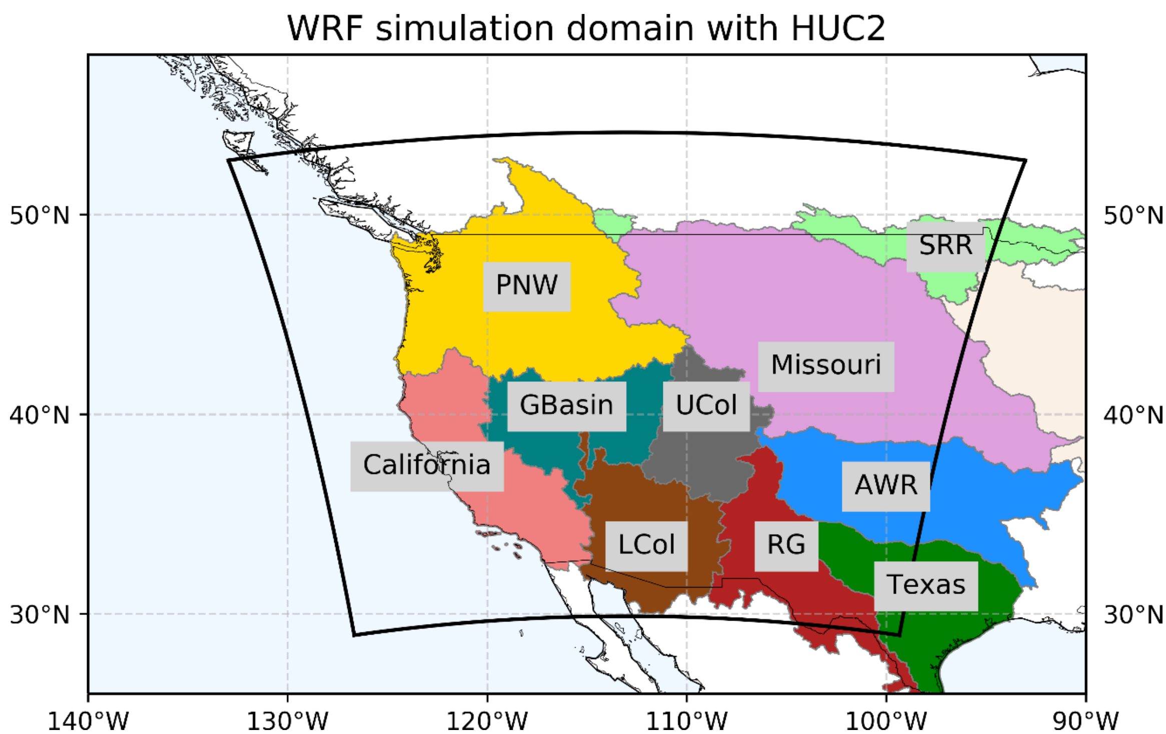

Figure 2.1. WRF simulation domain. The colored regions are the 2-digit Hydrological Unit (HUC2) watersheds. "SRR": Souris-Red-Rainy region; "AWR": Arkansas-White-Red region; "RG": Rio Grande region; "UCol": Upper Colorado region; "LCol": Lower Colorado region; "PNW": Pacific Northwest region.

2.1.2.1 Atmospheric Rivers

Heavy precipitation, intense snow melting, and flooding are among the most significant hydrological extremes in the western United States, and they cause huge societal and economic losses every year. Many of these extreme events are caused by or related to atmospheric rivers (ARs), which feature bands of high precipitable water in the atmosphere spanning thousands of kilometers long and are responsible for over 90% of poleward moisture transport.

In this study, we conduct and evaluate a 35-year regional climate simulation at 6-km grid spacing of the hydroclimate in the western United States during 1981–2015. Winds, temperature, water vapor, pressure, and surface variables from the NARR (Mesinger et al.,

2006) at 32-km horizontal resolution and 3-hourly time intervals were used and interpolated to provide initial and boundary conditions for the WRF simulations.

This high-resolution simulation was analyzed to understand the atmospheric conditions associated with ARs and how they influence surface hydrological processes. More specifically, we address the following questions (Chen et al., 2018, 2019):

- How are ARs related to extreme precipitation both in occurrence and magnitude?
- How do landfalling ARs from the Northeast Pacific Ocean modify the surface meteorological conditions and their spatial distribution in the western United States?
- What are the impacts of landfalling ARs on the surface water budget components, and how are they related to the surface meteorological conditions associated with ARs?
- What is the overall surface hydrological response to landfalling AR events compared to non-AR events in the western United States?

With improvements in forecasting ARs in global models, quantitatively relating the AR occurrence and intensity to extreme precipitation represents an important predictability that can be exploited for hydrologic forecasting and emergency preparedness.

To characterize uncertainty in projecting precipitation extremes, the regional WRF simulations were also analyzed to identify the physical-dynamical mechanisms responsible for changes in extreme precipitation in different climate regimes. In California and the Pacific Northwest, extreme precipitation is often associated with atmospheric rivers (ARs) (Chen et al. 2019) that transport warm, moist air of tropical origin in narrow bands that produce heavy precipitation upon landfall over the coastal mountains. These are predominantly cold-season processes because frontogenesis plays an important role in the development of ARs. Because ARs can significantly modulate surface hydrological processes (e.g., snow) through the extreme precipitation they produce, we quantified the relationship between ARs and the magnitude of extreme precipitation, and their impacts on land-surface hydrologic process.

One of the largest uncertainties in relating extreme precipitation to ARs is how ARs are defined and tracked. To quantify how differences in AR-tracking methods may influence the attribution of moisture transport, precipitation, and hydrologic extremes to ARs, the Atmospheric River Tracking Method Intercomparison Project (ARTMIP) has been initiated (Shields et al., 2018). As part of this effort, participants applied their AR- tracking methods to the Modern-Era Retrospective Analysis for Research and Applications, version 2 (MERRA-2) reanalysis data (Gelaro et al., 2017) and identified all ARs between 1981 and 2016. We selected six methods that produced relatively higher and lower numbers of AR events along the U.S. west coast, with the total numbers of detected AR events varying by one order of magnitude, (as summarized in supporting information Table S1; Chen et al., 2018). Overall, the Rutz, Gershunov, and Guan algorithms identified the largest number of ARs, while the other three (Goldenson, PNNL1 (Pacific Northwest National Laboratory method 1), and PNNL2 (Pacific Northwest National Laboratory method 2) identified the lowest number of ARs, so our selection of these six methods represents the full range of AR-tracking results from ARTMIP. All the AR events are classified as north or south depending on their landfalling locations along the west coast between 40°N and 60°N (Pacific Northwest [PNW]) and 25°N and 40°N (California), respectively, to better present their localized effect.

Precipitation data is from the WRF simulations over the western United States during 1981–2015. Analysis of precipitation in watersheds at the Hydrological Units level provides a connection to the surface hydrological processes because watersheds are closed systems (i.e., each watershed has only one outlet for runoff) for soil hydrology. The raw hourly precipitation output at a 6-km grid spacing is then aggregated to 1,080 eight-digit Hydrological Unit (HUC8) watersheds at a daily scale. The WRF simulations captured the spatial variability of daily mean and 95% extreme precipitation realistically compared to the PRISM (Parameter-elevation Relationships on Independent Slopes Model) observations (Daly et al., 2008).

Predictability of extreme precipitation is considered for both occurrence and magnitude. Here *extreme precipitation events* are defined as 95% percentile daily precipitation events (i.e., days with precipitation amount higher than 95% of the daily records during 1981–2015) at each HUC8 watershed. From the occurrence perspective, we used the occurrence of ARs to predict the occurrence of extreme precipitation events. The skill is quantified using Gilbert Skill Score (GSS). GSS evaluates how well the predicted events (hit or miss) correspond to the observations, with an adjustment for the correct forecast due to random chance (e.g., more ARs identified increase the chance of overlapping with extreme P days), making it more appropriate for our analysis than other measures of skill score.

On the correlation between ARs and precipitation magnitude, we developed a higher-level metric, hereafter referred to as *Intensity-Duration-Area* (IDA), to characterize the overall intensity of landfalling ARs at the event scale. This metric is based on integrated vapor transport (IVT) and each landfalling AR event is characterized by one IDA value that defines its intensity, duration, and area of influence over land. We investigate the relationship between IDA and extreme precipitation at a monthly scale because at daily and weekly scales, the relationship between extreme precipitation events and IDA would be dominated by the concurrence of non-AR days/weeks and nonextreme precipitation days/weeks. At each HUC8 watershed, we identified the extreme daily precipitation events and summed up the total for each month. We also summed up the IDAs of all the landfalling ARs in each month. Then the correlation between the monthly IDA and the monthly total extreme precipitation was computed to reveal their relationship.

To better understand the relationship between ARs and extreme precipitation, we used the K-means clustering method to classify the AR events into different categories that can be characterized as weak ARs (short duration and low intensity), flash ARs (short duration but high intensity), and prolonged ARs (long duration).

ARs can significantly modulate surface hydrological processes through the extreme precipitation they produce as well as important changes to the surface energy balance. ARs consistently lead to heavier precipitation compared to non-AR events but the impact of ARs on temperature depends on the season. There are also important differences depending on the absence or presence of snow. To better understand the complex impacts of ARs on surface hydrologic processes, precipitation events without an AR are identified as "non-AR" events. Further, precipitation events are classified into three types:

- summer events (denoted as "summer") that happen between 1 April and 30 September;
- winter snow condition events ("winter (snow)") that happen between 1 October and 31 March, with snowpack existing before the events;

- winter dry condition events (“winter (dry)”) that happen between 1 October and 31 March, without snowpack existing before the events.

2.2 Results

2.2.1 Predictability of Extreme Precipitation in Western U.S. Watersheds Based on Atmospheric River Occurrence, Intensity, and Duration

The correlation between AR intensity-duration-area (AR-IDA) and the extreme precipitation amount at the monthly scale is illustrated in Figure 2.2. The performance of different AR-tracking algorithms varied widely, but in general, the Goldenson and two PNNL methods performed better because fewer ARs identified were generally associated with more intense or prolonged ARs and they were more likely to be related to heavy precipitation. We also used other metrics such as Gilbert Skill Scores (GSSs) to compare the different AR-tracking algorithms (Figure 2.3). Based on both GSSs and correlations, we concluded that the Goldenson and PNNL models performed better than the others.

In Figure 2.2, higher correlations (~0.5) were observed between ARs and extreme precipitation events across the western United States especially in the coastal regions, suggesting that ARs can provide useful predictability for extreme precipitation occurrence and magnitude in western United States watersheds. Due to the typical southwest-northeast orientation of ARs, watersheds in the north are more susceptible to AR-induced heavy precipitation. We found that, in general, weak ARs (short duration and low intensity) account for 50–60% of all AR events, but they are weakly correlated with extreme precipitation. This is more obvious for AR-tracking algorithms that identify more ARs.

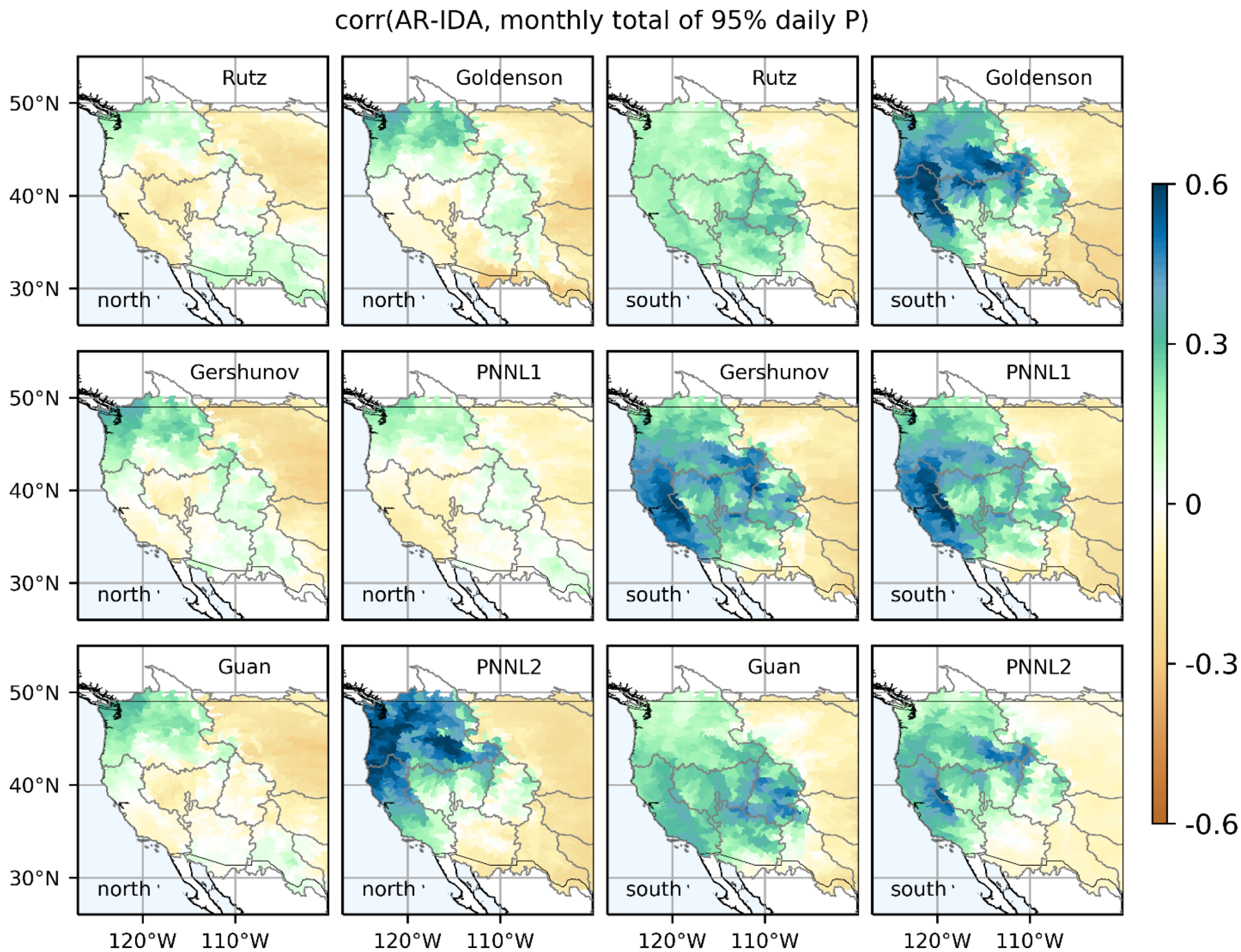

Figure 2.2. Correlation coefficients between AR intensity-duration-area (IDA) and the monthly total of extreme daily precipitation amount. The first and second columns are for ARs in the north (making landfall between 40°N and 60°N) derived from six AR-tracking algorithms. The third and fourth columns are for ARs in the south (making landfall between 25°N and 40°N) (see Chen et al. 2018).

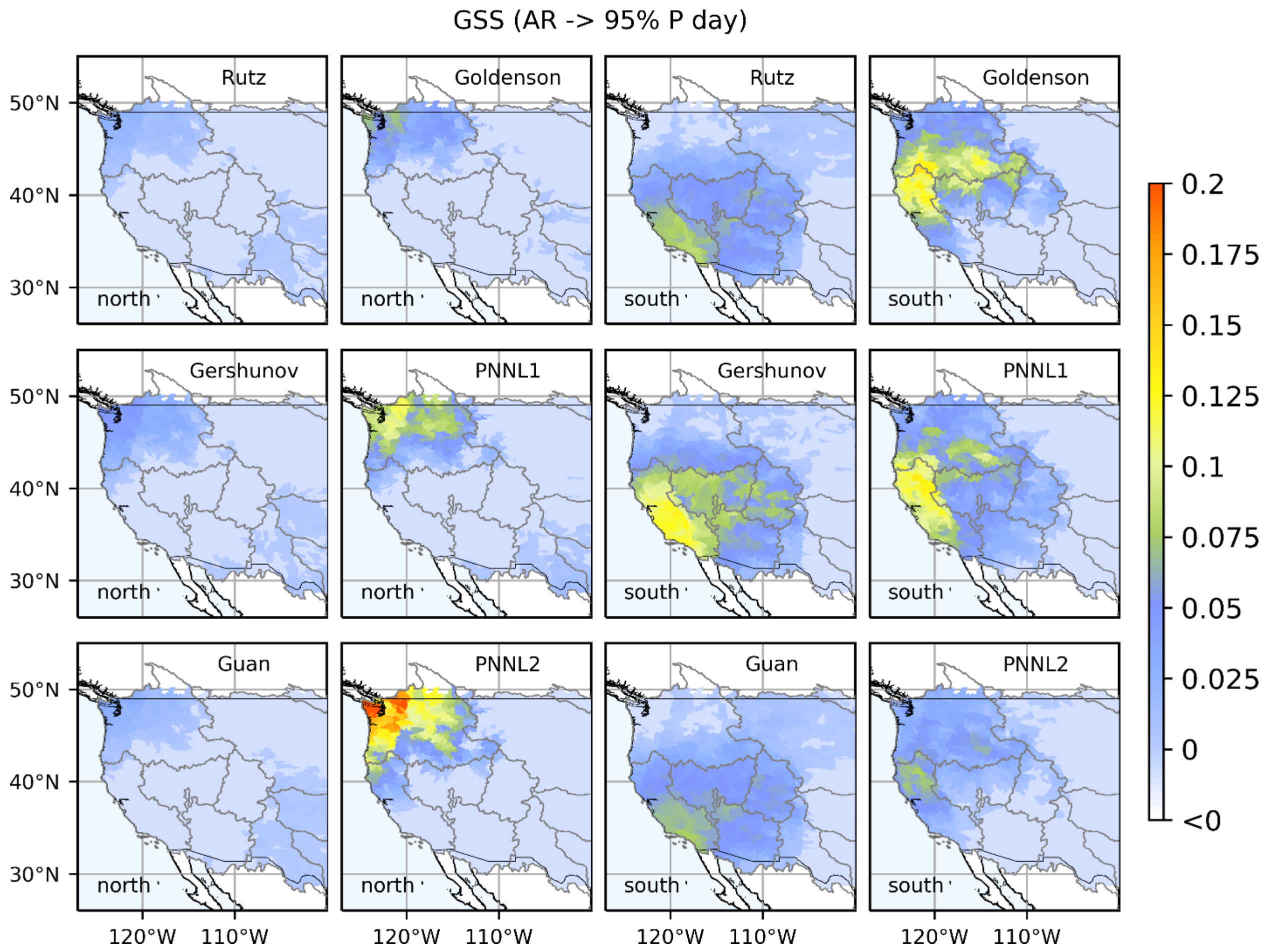

Figure 2.3. Gilbert Skill Scores (GSSs) for predicting the number of extreme precipitation days using ARs. A GSS of zero equals no skill and a GSS of 1 indicates a perfect score (see Chen et al. 2018).

2.2.2 Impact of Atmospheric Rivers on Surface Hydrological Processes in Western U.S. Watersheds

In addition to extreme precipitation, we further investigated the impacts of ARs on watershed water budget using the WRF simulations in the western United States. Large seasonal differences emerged in water budget components in AR events compared to non-AR events. Figure 2.4 presents the overall differences in major water budget components, including precipitation, surface runoff, evapotranspiration (ET), and soil moisture between AR and non-AR events. As expected, precipitation was significantly higher during AR events. Surface runoff resembled the difference in precipitation, where coastal watersheds such as the western Cascades and the Sierra Nevada experienced the largest increase in runoff during ARs. In winter, when not limited by soil moisture, the ET difference mainly reflected the difference in total radiation (Chen et al. 2019). In summer, the ET difference was controlled by radiation and/or soil moisture, depending on whether ET is energy- or moisture-limited in specific areas. The soil moisture increased across all areas during AR events for both the summer and winter seasons, but more spatial heterogeneity was observed for snow water equivalent (SWE). In summer, all precipitation events caused the snow to melt, but ARs led to moderately more snow ablation in the Pacific Northwest, which could be attributed to warmer temperature or increased longwave radiation. In winter, snow generally accumulated during winter non-AR precipitation events, while ARs led to widespread snow ablation (i.e., the mechanisms for rain-on-snow [ROS] events).

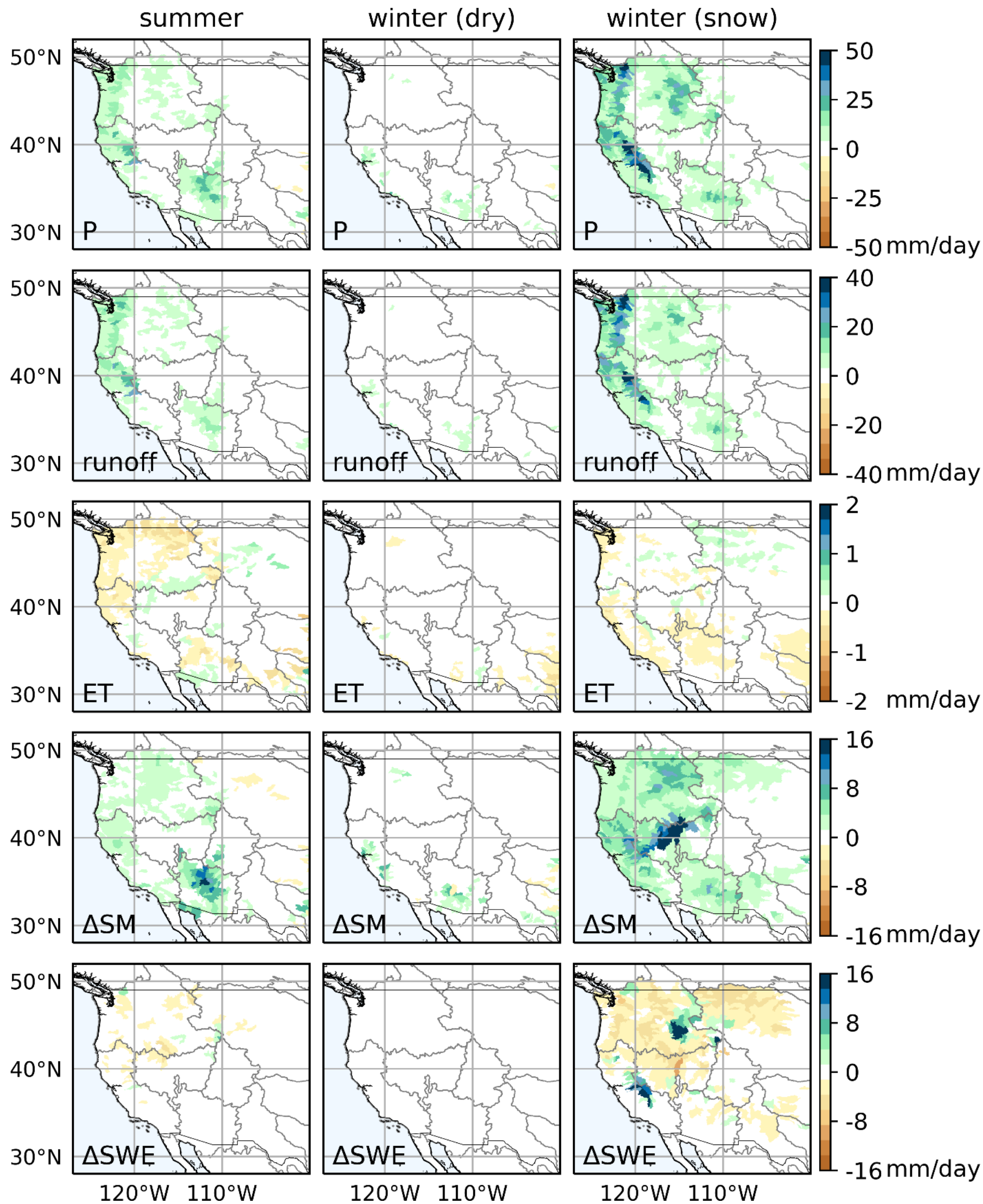

Figure 2.4. The difference in HUC8surface water budget associated with AR and non-AR precipitation events (AR minus non-AR). Top to bottom: precipitation, runoff, evapotranspiration (ET), soil moisture change (ΔSM), and SWE change (ΔSWE) (mm/day). Left to right: summer (1 April to 30 September), winter (dry - 1 October to 31 March, without snowpack existing before the events), winter (snow - 1

October to 31 March, with snowpack existing before the events) (see Chen et al. 2019).

Similar to the “water cycle” chart presented in hydrology textbooks, we developed a “water budget chart” here (Figure 2.5) to illustrate the AR impacts on surface hydrology averaged over the hydrologic unit code (HUC) 8 watersheds in the western United States. In Figure 2.5, it is observed that compared to non-AR events, ARs produced much higher precipitation but slightly suppressed ET. This substantially increased the water input to the surface hydrological system. During ARs, strong radiation and warm temperature increased the likelihood and the magnitude of ROS events, which caused enhanced snow ablation. On average, ΔSWE was −0.1 mm/day (melt) during AR events, while it was 1.46 mm/day (accumulation) during non-AR events. Our regression analyses attributed these differences in snow accumulation and ablation to the change in temperature/radiation during ARs. Specifically, warmer temperature caused snow ablation of 3.49 mm/day and increased net radiation triggered snow ablation of 0.97 mm/day during ARs.

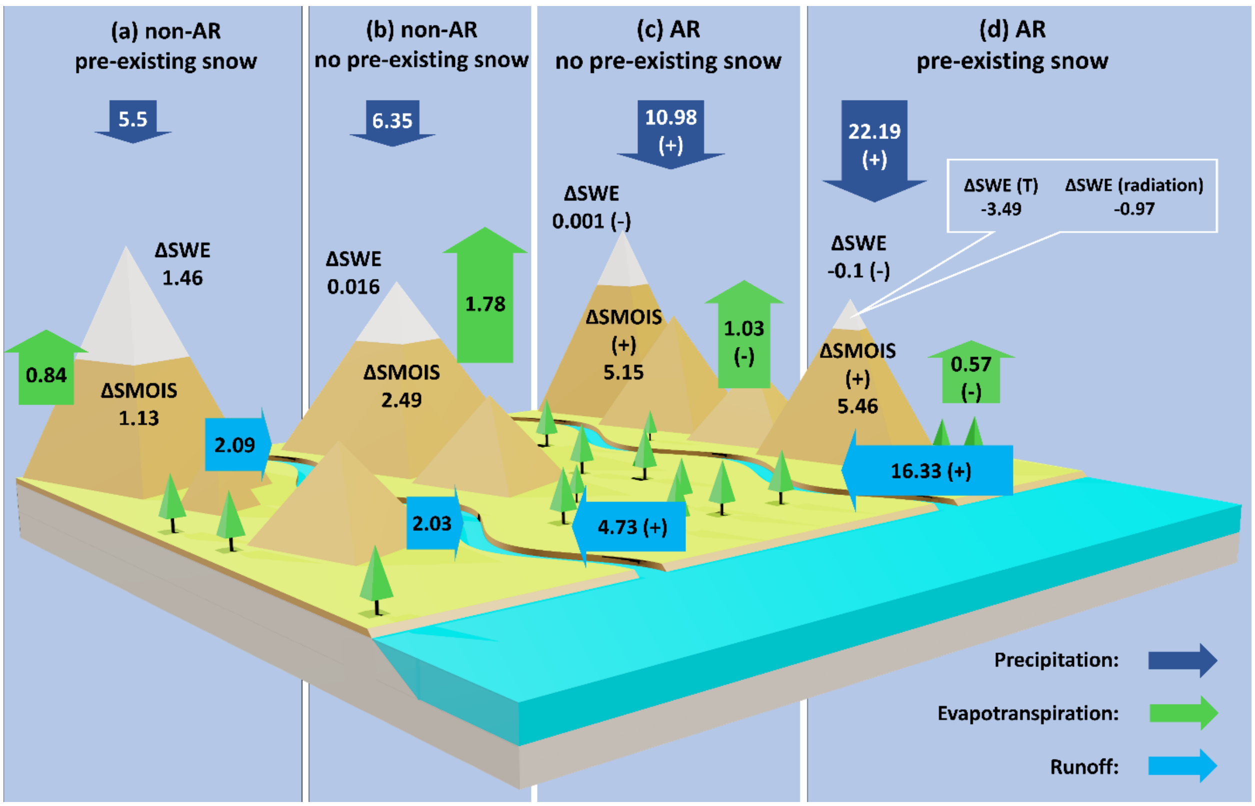

Figure 2.5. Illustration of the surface hydrological response to non-AR and AR precipitation events with and without pre-existing snowpack. Unit: mm/day. SMOIS = soil moisture (See Chen et al. 2019.)

Our major findings include the following (Chen et al., 2019):

- ARs are associated with surface meteorological conditions rather distinct from non-AR events. ARs consistently lead to heavier precipitation compared to non-AR events but the impact of ARs on temperature depends on the season. We found that ARs lead to warming in winter but cooling in summer. Depending on the relative decrease in shortwave radiation and increase in longwave radiation due to cloud cover and increased water vapor, the total radiation at the surface is consistently decreased in summer, but a strong north-south dipole pattern that features an increase in the north while a decrease in the south is found in winter.

- The changes in surface meteorological conditions suppress evapotranspiration and induce stronger snow ablation and a larger increase in soil moisture. As a result, ARs tend to generate much higher runoff in both winter and summer, regardless of whether there is preexisting snowpack.
- Rain-on-snow contributes to an amplification of the runoff (R) response (as represented by the *R*/*P* ratio) during ARs, making snow-covered watersheds/periods more susceptible to floods. With preexisting snowpack, the *R*/*P* ratio is almost doubled from non-AR to AR events in the western United States. Rain-on-snow is important for the runoff response during weak AR events (50–60% of all AR events), while the direct *P*-runoff response is dominant during extreme AR events.
- Rain-on-snow during ARs can be well explained by the warmer air temperature and stronger longwave radiation during ARs, contributing to 3.49 and 0.97 mm/day of snow ablation individually. With preexisting snowpack, instead of snow accumulation of 1.46 mm/day under non-AR events, AR conditions lead to snow ablation of 0.1 mm/day.
- At interannual scale, a large fraction of variability of water availability (as represented by total runoff) can be explained by the number of AR days at watershed scale along the U.S. West Coast. At intraannual scale, more ARs means less snowpack for summer runoff so ARs tend to sharpen the runoff seasonality.

Thus, we identified two physical mechanisms through which ARs produced higher flooding events than non-AR events: (1) ARs produced higher P and modification of initial soil moisture, and (2) ARs enhanced ROS events that provided extra snowmelt water into soil.

2.3 Discussion

ARs provide useful predictability of extreme precipitation occurrence and magnitude in western U.S. watersheds. To improve prediction skill, those AR-tracking algorithms with higher IVT thresholds should be considered. Alternatively, AR classification can be used to effectively filter out the nonsignificant ARs. Due to the typical southwest-northeast orientation of ARs, watersheds in the north are more susceptible to AR-induced heavy precipitation. We found that, in general, weak ARs (short duration and low intensity) account for 50–60% of all AR events, but they are weakly correlated with extreme precipitation. This is more obvious for AR-tracking algorithms that identify more ARs. Future studies should prioritize the intense or prolonged AR events to improve the prediction skills of these events and investigate their meteorological, hydrological, and societal impacts.

Consistent with previous studies, we found that the ROS process can heavily modulate the snowpack response. Here we present a comprehensive analysis of how the surface water balance responds to atmospheric forcing under AR and non-AR conditions, whereas previous studies have focused on the response of individual hydrological processes. Our analysis indicates that the soil moisture response to precipitation events is similar between AR and non-AR events, so the precipitation and snowpack changes are translated directly to changes in runoff. Overall, the runoff response is dominated by the precipitation difference between AR and non-AR events, but the contribution from ROS is roughly 25% of the total runoff response, so it is not negligible. For weak ARs with lower P, the contribution from ROS may become even more significant. For extreme ARs, Establishing the relationship between P and runoff is more important, while for weaker AR events such as the “weak ARs” classified by Chen et al. (2018), focusing on the impact of ROS is more important for improving prediction of flood events.

As discussed above, ROS can account for 25% of the total runoff and increase the *R*/*P* ratio during ARs to nearly double that of non-AR events. Hence, AR frequency explains a large fraction of the interannual variance of annual runoff so management of water resources must consider the variability of ARs for long-term planning. The relationship between the 1 April SWE/*P* ratio and AR days in winter also indicates that ARs could sharpen the seasonality of water resources in watersheds where snow- pack is important for summer water supply, therefore posing challenges to water resource management.

The presented surface hydrological responses vary as a function of space and time with important ramifications on runoff production and water resource management. For example, snowpack cold content differs at different times of the winter season, which will affect the rain-on-snow frequency and magnitude during different times of the snow season. Antecedent soil moisture is also considerably different between wet and dry years, and this will also affect the runoff response. These results were developed at the HUC8 spatial scale (1,080 in the western U.S.) and illustrate the importance of precipitation, air temperature, and surface energy balance components – all of which may show significant variation over relatively short distances (sub-HUC8), particularly in mountainous terrain. We examine these processes at an ultra-fine 90 m spatial resolution in Columbia River Basin (over 80 million DEM grid cells) in Section 5.0).

3.0 Parallelization and Testing of the Distributed Hydrology Soil Vegetation Model (DHSVM)

The downscaled climate model data were used to drive DHSVM at a 90 m spatial resolution and a 3 hour time step. To model the entire Columbia and Connecticut Basin at 90 m, the DHSVM code was parallelized and the MASS1 hydrodynamic model was integrated with DHSVM. Additional detail about DHSVM, the approached used to parallelize the model, and its integration with MASS1 is given below.

3.1 Distributed Hydrology Soil Vegetation Model

The DHSVM (Wigmosta et al. 1994) is a spatially distributed, physics-based hydrology model that simulates the overland and subsurface hydrological processes influenced by climate, topography, soil, and vegetation. DHSVM comprises a two-layer canopy model, an energy-balance two-layer snow model, a multi-layer soil model, and three-dimensional surface and subsurface flow routing models. These models allow for characterization of hydrological processes including canopy and topographic shading, canopy interception, evapotranspiration, snow accumulation and melt, and water movement overland and through the soil to streams and rivers. In an extensive review of 30 hydrological models (Beckers et al. 2009), DHSVM was identified to be best suited for modeling mountain hydrology in forested environments.

Initially developed in the early 1990s (Wigmosta et al. 1994), DHSVM has been applied extensively, particularly in forested, mountainous, snowfall-dominated regions, to characterize the hydrologic regime and project potential changes with changing climate and landscape (Storck et al. 1998; Storck and Lettenmaier 1999; Leung and Wigmosta 1999; Thyer et al. 2004; Cuo et al. 2009; Cristea et al. 2014; Livneh et al. 2015; Cao et al. 2016; Sun et al. 2018). Subsequent adaptations have extended the capability of DHSVM to represent urban landscapes with impervious surfaces and runoff detention (Cuo et al. 2008), glacio-hydrological dynamics (Naz et al. 2014; Frans et al. 2015, 2018), river thermal dynamics (Sun et al. 2015; Cao et al. 2016), urban water quality (Sun et al. 2016), and forest-snow interactions in canopy gaps (Sun et al. 2018).

With the increasing availability of high-resolution satellite products, e.g., LIDAR and advances in high-performance computing systems and data storage, there is evolving interest in exploring hydrologic fluxes and state variables at progressively higher spatial resolutions for applications ranging from regional to global scales (Lettenmaier et al. 2015). High-resolution, spatially distributed modeling capabilities are particularly important for representing complex mountain hydrology that is highly affected by heterogeneous terrain and strong climate gradients with elevation. A spatially lumped modeling approach with sparsely distributed observation networks can limit our ability to understand and predict the implications of changing climate and landscape on available water for extreme runoff events, regional water supplies, and associated reservoir operations for hydropower and other water allocations (Bales et al. 2006).

3.1.1 *Grid Cell Energy/Water Balance*

A DHSVM model grid cell consists of a set of soil layers, a set of snowpack layers (when present), and a multi-level vegetation canopy (Figure 3.1). Meteorological forcing data are used to drive the energy balances in the snowpack, resulting in melt and/or accumulation, and in the vegetation canopy, resulting in evapotranspiration.

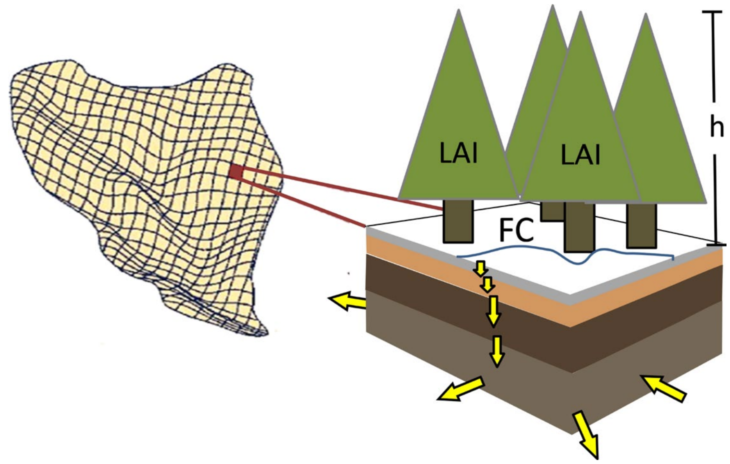

Figure 3.1. Schematic representation of water movement in the DHSVM domain. The DHSVM domain is divided into rectangular cells in which water and energy balance is maintained. Excess surface and subsurface water are routed cell-by-cell to the channel network. LAI is leaf area index, FC stands for fractional cover of forest canopy, and h is canopy height.

Movement of water in the cell's soil layers is simulated. This includes infiltration or exfiltration, evaporation from the soil surface, evapotranspiration from soil layers in which vegetation has roots, vertical saturated and unsaturated water movement between layers, and drainage to a subsurface soil layer.

The DHSVM simulates snow processes on the grid scale with a two-layer canopy model, and a two-layer below-canopy energy and mass balance snow model. The canopy snow model explicitly represents the combined canopy processes that govern snow interception, sublimation, mass release, and melt (Wigmosta et al. 2002). In each model grid, the soil/vegetation class is prescribed through spatial input, and the attribute parameters for the soil/vegetation class are prescribed through the model configuration file. An independent one-dimensional (vertical) coupled energy and water balance is calculated for each grid cell. The snowpack energy balance described in Equation (3.1) determines the net energy input to snowpack (ΔQ):

$$\Delta Q = NSW + NLW + H + LE + M \tag{3.1}$$

where

NSW = net shortwave radiation,
NLW = net longwave radiation,
H = the sensible heat flux,
LE = the latent heat flux from evaporation and sublimation/condensation, and
M = advected heat from rainfall to snowpack.

Conductive heat at the snow-ground interface is neglected. Flow is routed vertically based using a one-dimensional multi-layer soil model, and laterally based on a quasi-three-dimensional saturated subsurface flow model. The core DHSVM model physics and structure in the original version are described in detail by Wigmosta et al. (1994), Storck et al. (1998), and Wigmosta et al. (2002).

3.1.2 *Flow Routing*

The surface and subsurface volumes computed in the cell energy/water balance are routed to neighboring cells (Figure 3.1). The DHSVM routing schemes are documented by Wigmosta et al. (1994), Wigmosta and Lettenmaier (1999), and Wigmosta et al. (2002). Both surface and subsurface routing work with a similar algorithm.

A gradient, based on the ground surface or water (table) surface, is used to determine the direction and magnitude of flow for each cell. In a cell, discharge to each neighboring cell is computed and stored. Surface water flux from active cell *i j* to its *k*th down slope neighbor is computed as

$$q_{oi\,j} = w_{i\,jk}\, v_{i\,jk}\, y_{i\,j}\,(1) \tag{3.2}$$

w_{ijk} is the flow width in the *k* direction, v_{ijk} is the overland flow velocity, and y_{ij} is the overland flow depth. Subsurface flow from active cell *i j* to its *k*th downgradient neighbor is computed as

$$q_{si\,jk} = w_{i\,jk}\, \beta_{i\,jk}\, T_{i\,j} \tag{3.3}$$

where $\beta_{i\,jk}$ is the cell water table or land slope and $T_{i\,j}$ is the soil transmissivity, assuming an exponential decrease in saturated hydraulic conductivity with depth.

After surface and subsurface routing is complete, computed stream channel interception of surface and subsurface flow is accumulated for each cell in which a stream channel lies. The intercepted water volume is summed and used as lateral inflow for each stream segment in the channel network. The lateral inflow is then routed through the network that is represented by a cascade of linear reservoirs (Wigmosta et al. 2002) with a constant flow velocity calculated using Manning's equation with the hydraulic radius in each reach corresponding to channel depth at 75% of the bank full height.

3.2 Methods

3.2.1 DHSVM Code Parallelization

While DHSVM has been under constant development since its inception, it has always been a serial code, e.g. its computational performance has been tied to the performance of a single processor. Parallelization is a good strategy for helping meet current and future simulation needs. Several examples in the literature describe parallel hydrological models. The majority (e.g., Hwang et al. 2014; Liu et al. 2014, 2016; Adriance et al. 2019) seem to favor small shared memory platforms using OpenMP (Dagum and Menon 1998). A few (Vivoni et al. 2011; Kumar and Duffy 2016) target distributed memory systems using the Message Passing Interface (MPI; MPI Forum 2018).

In this work, DHSVM was made into a parallel code while maintaining most of its existing capability. The parallel code development was aimed at large distributed memory clusters, but portability to smaller multiprocessor, shared memory systems, such as desktops and laptops, was maintained. An alternate interprocess communication programming model, Global Arrays (GA, Nieplocha et al. 2006; Manojkumar et al. 2012) was used. GA provides a partitioned global address space (PGAS) and implements one-sided communication protocols. Complete details are provided by Perkins et al. (2019); a brief description is provided below.

3.2.2 *Code Parallelization*

The multiple instruction, multiple data (MIMD; Wilkinson and Allen 1998) parallel model was used. This approach targets large, distributed memory systems (i.e., clusters), but the approach should work fine for smaller, shared memory systems (multi- processor desktops and laptops) without modification. In the MIMD model, each processor is assigned its own data to work on independently and some communication layer is required to exchange data between processors when needed. In this case, each DHSVM process is assigned a non-overlapping rectangular subset of the active cells in the domain.

The goal was to make DHSVM as fast as practical while retaining as much of its existing behavior as possible. DHSVM is a relatively large and complicated code. Resources were not available to design and code a parallel DHSVM from the ground up. This in some ways limited the parallelization approach and results.

3.2.3 *Interprocess Communication*

Interprocess communication in DHSVM was implemented using GA (Nieplocha et al. 2006; Manojkumar et al. 2012). GA is a “partitioned global address space library for distributed arrays.” GA provides a distributed, random access, multi-dimensional array data structure. Such an array is consistent with the internal DHSVM data structures, so most of the serial code structure could be retained. In addition, nearly all the required interprocess communication consists of floating point values, which simplifies coding.

In general, DHSVM interprocess communication is all cell-based numeric values (i.e., rectangular arrays). In a typical communication scenario, a GA structure is created. Transfers of values are made from local memory to the GA (put) and from the GA to local memory (get). Other operations are available, like “accumulate” where values in local memory are summed into the GA.

GA can use several underlying communication protocols, depending on the underlying hardware. The most commonly used are based on MPI and can be used on almost any platform that supports MPI. These range from large clusters to laptops—any shared or distributed memory system for which MPI is available (Dinan et al. 2012). DHSVM relies entirely on the GA application programming interface (API). There are no direct calls to any other parallel communication interface.

3.2.4 *Domain Decomposition*

The most straightforward approach to parallelization was to distribute cell-based calculations across processors. A divide and conquer strategy was implemented that has some similarity to the strategy used by Hwang et al. (2014). Each process was assigned a non-overlapping rectangular region of the original domain. As shown in Figure 3.2, the region assigned to a process may be a collection of rows (STRIPEY) or a collection of columns (STRIPEX). An algorithm similar to Simeone’s (1986) is used to evenly distribute the *active* cells among the processors. When splitting the domain by rows, for example, the number of active cells in each row are summed and summed again into a cumulative histogram. If the rows are to be divided into p groups, the cumulative histogram is searched for the splits closest to $1/p$, $2/p$, . . . , p $1/p$. A similar search of the columns’ active cell cumulative histogram is done to split the columns.

The decomposition described is used *only* for the cell-based calculations. The channel network is *not* divided among processes. Each process is assigned complete representation of the domain's entire channel network.

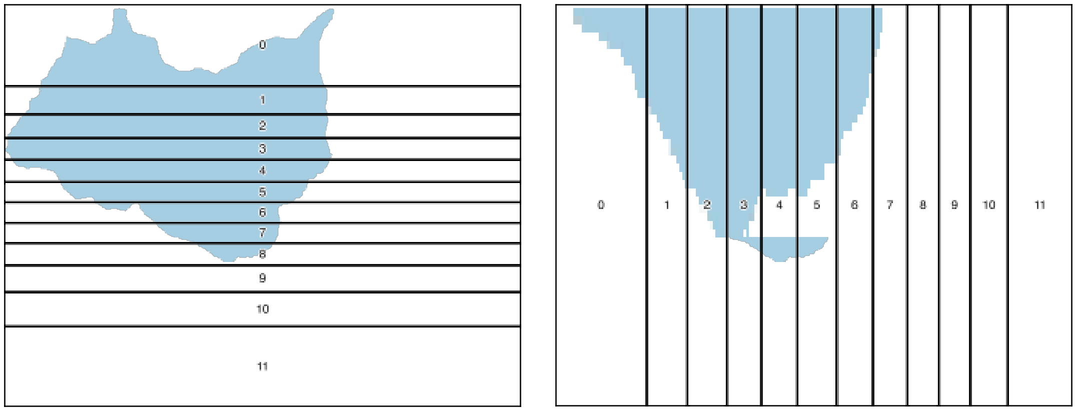

Figure 3.2. DHSVM domain decomposition methods applied to a sample basin for 12 processors: splitting the domain into (left) groups of rows (STRIPEY) or (right) columns (STRIPEX). The default method is chosen depending on which global dimension is larger.

3.2.5 *Input/Output*

A distributed hydrology model like DHSVM requires considerable input data and can produce simulation results of considerable size. The choice of how the data are input and output can significantly affect parallel performance. The input/output (I/O) strategy used here was relatively simple and largely emphasized maintaining existing behavior, such that the serial code structure was mostly maintained. When I/O bottlenecks are identified in future applications, a more complex strategy may be deployed.

All processes read the configuration file, so that, at startup, all processes have a complete description of the simulation without further communication. Other text files, like the stream network description, are also read by all processes. These files are typically small in size, and the time to read them is usually inconsequential.

DHSVM requires several input data sets that vary cell by cell. These data sets are input in the form of a two-dimensional (2D) raster map. In the parallel DHSVM, 2D map data are input through the root process (serially) then distributed via a global array. At the time of this writing, parallel I/O was not used, but may be supported in the future. For this work, DHSVM required considerable reworking of 2D data I/O to be able to work efficiently over a wide range of computational resources.

Two 2D map resolutions are necessary. The first is at the resolution of the DHSVM cell size and contains a single value for each cell. Data sets input at this resolution include the DEM, soil type, and vegetation type. Maps of this resolution are *partitioned* and distributed to processes according to the domain decomposition. The second map resolution is much coarser and not necessarily aligned with DHSVM cell boundaries. This was used for input of meteorological data fields. For data sets at this coarser resolution, the entire 2D map is *mirrored* on all processes, i.e., all processes receive an identical copy of the map. Mirroring the entire map in this way avoids a more complicated decomposition that would require overlapping sub-domains.

A global array is created with a size to store values for the entire domain. A single process opens and reads, serially, a 2D map for the entire domain into local memory. This process then puts those data in the global array. All processes, including the process reading the map data, then get the portion of the global array it has been assigned. In this work, meteorological data were supplied as a series of 2D maps of each required fields. At the beginning of each time step, the maps for that time step are read as described above.

All output, both 2D map data and text files, is through the root process. Writing 2D map data is the reverse of reading. Each process puts its local values in the global array, the root process gets the entire set of values and writes them to a file. Output other than 2D maps, (e.g., mass balance summary) requires a more traditional MPI-like all-reduce operation (using the GA API though).

3.2.6 *Hydrologic Processes Adaptation*

Figure 3.3 shows a simplified depiction of the parallel algorithm for a single simulation time step. Each simulation time step starts with time-step initialization (TSI). Each process prepares the cells it owns for the next time step. The most important part of TSI is the assignment of meteorological data to individual cells. DHSVM has several available approaches to making this assignment, but each of eight meteorological data fields were read as mirrored 2D maps. This is a significant amount of data that needs to be read every time step.

Once cells are initialized, energy/water balance (EWB) calculations proceed. Each process updates the hydrologic and thermal state of the snowpack, vegetation canopy, and soil layers within the active cells assigned to it. The computations for a single cell do not require any communication with its neighbors, so this part of the simulation is most amenable to parallelization.

Unlike the EWB, subsurface and surface routing (SSR and SR) calculations require interaction with neighboring cells, and that interaction needed to extend between processors when neighboring cells were not owned by the same processor. SR and SSR routing have very similar algorithms, so the parallelization of those processes is handled in a similar manner. The key issue with these processes is that a cell assigned to one processor may drain to a cell on another processor. This is handled by extending the calculated local domain by one cell. A temporary array is created on a local processor to hold the results of SR or SSR routing. The array is sized to be one cell larger, in all (valid) directions, than the domain assigned to the processor. That extra cell captures SSR or SR flux to the off-processor cell(s). As routing calculations proceed, surface water is routed to a cell outside the processor’s domain, and the result is stored on the edge of the array.

After all processes complete local SR and SSR calculations, a global array for the entire domain is initialized to zero. Each process then accumulates the local array of routing results into the global array. In this way, water routed outside of the processor’s local domain is correctly captured and delivered to the neighboring domain. A GA get operation returns complete SR or SSR routing results from the global array to each processor’s local memory.

The SR and SSR algorithms compute the lateral inflow into each channel segment. However, each processor only computes lateral inflow contribution from the cells assigned to it and it’s necessary to add contributions from multiple cells (and processes). Consequently, lateral inflow for each channel segment is totaled from the contributions computed by all processes. An all-reduce summation, typically an expensive operation, is used to sum lateral inflow over all processors. After the all-reduce, all processes have an identical array of lateral inflow to all segments.

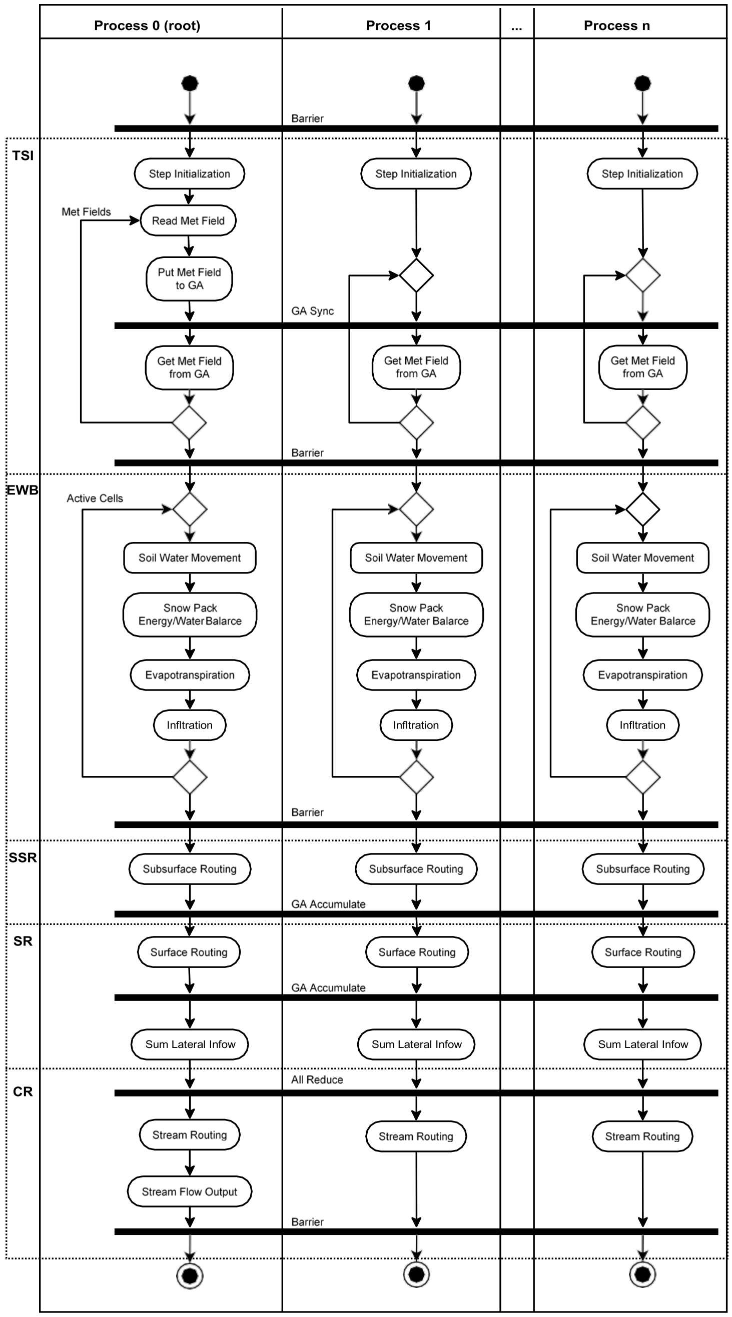

Figure 3.3. Simplified activity diagram for a single time step in parallel DHSVM. The dashed boxes indicate specific tasks discussed in the text: time-step initialization (TSI), energy/water balance (EWB), subsurface routing (SSR), surface routing (SR), and channel routing (CR).

The simulation time step ends with channel routing. The cascade routing approach requires that a segment can only be routed after all upstream segments have been routed. Consequently, it was decided to keep channel routing a serial algorithm and that all processes would carry out identical computations. All processes then perform CR on the same network with the same inflow producing identical results. Only the root process outputs CR results.

3.3 Testing DHSVM Parallelization in the Columbia River Basin

The entire Columbia River Basin and the smaller Clearwater River Basin contained within it were chosen to measure parallel DHSVM performance. The Clearwater River is an upland tributary in the Columbia River Basin located in northern Idaho, USA (Figure 3.4). The basin area is 25,000 km^2, about 4% of the Columbia River Basin, and it produces about 7.5% of the Columbia River Basin's average annual discharge. The Clearwater River Basin DHSVM application was extracted as a subset of the Columbia River Basin, so it has the same computational resolution, 90 m, and uses the same source data. The Clearwater application consisted of about 3 million active cells and 2,600 stream segments. Complete details of the DHSVM application to the Columbia River Basin are provided in Section 5.1.2

The Columbia River Basin was simulated in DHSVM in two ways: 1) in a complete simulation mode where runoff-related computations are made and 2) in a "snow-only" mode where computations are focused on snowpack accumulation and melt. This is useful in snow-dominated applications because it allows for calibration and validation of the snowpack simulation at a significantly lower computational cost.

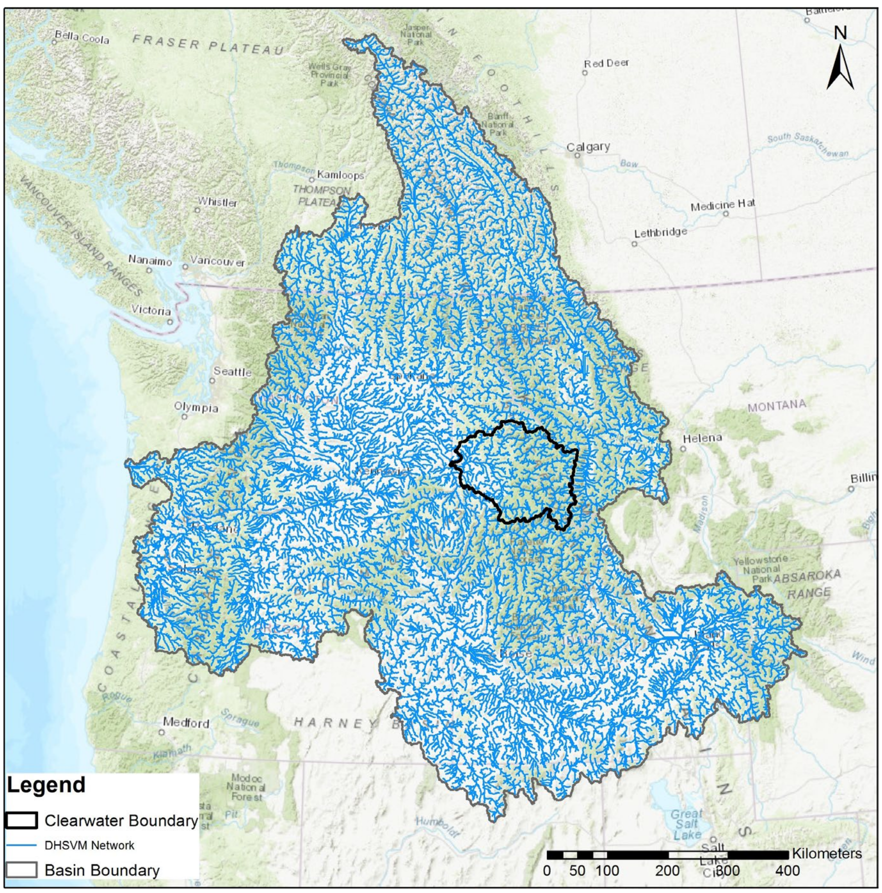

Figure 3.4. Columbia River Basin stream network used in DHSVM, consisting of about 20,800 stream segments. The Clearwater Basin used the 2,600 segments in the area

outlined in black. The network was generated using the DHSVM stream network preprocessing module.

3.4 Results

With the Clearwater simulation, a maximum speedup of about 32 times the serial version was attained using 128 processors (Figure 3.5), about 23,000 active cells per processor. One year's simulation time was reduced from almost 4 hours using a single processor to 8 minutes using 128 processors. Maximum speedup (using 480 processors) for the full Columbia simulation was about 105 times the serial version (Figure 3.5). The 1-year simulation time was reduced from about 19 days with one processor (estimated) to about 4 hours with 480 processors. With four processors, run time was dominated by computational tasks (90%), with the energy-water balance dominating that (67%). At maximum speedup (480 processors), the run time was split with about 60% for computational and 40% for I/O tasks. This is the reverse of the split for the Clearwater at maximum speedup.

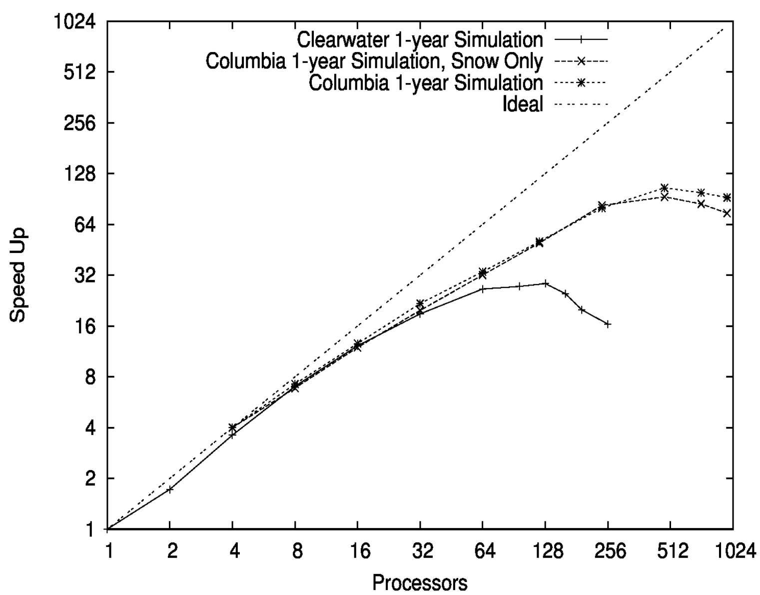

Figure 3.5. Measured DHSVM parallel speedup as a function of the number of processors for one year simulations of the Clearwater Basin, the Columbia Basin of only snow accumulation and melt, and the Columbia Basin with all hydrologic processes.

3.5 Discussion

In this work, we modified DHSVM to run in parallel using GA for interprocess communication targeting large, distributed memory systems. Simulation run times for our test cases were reduced enough to make long-term (decades), ultra-fine (90 m) spatial resolution simulations of significantly sized basins manageable. The second distinction is the straightforward domain decomposition technique.

The parallel performance indicates that running DHSVM at the point of maximum speedup may not be ideal. Run time needs to be balanced with the availability and cost of computational resources. For example, the Columbia simulation had a maximum speedup with 480 processors with a simulation time of about 4 hours. If the same simulation is run with 120 processors, it would take 8 hours. While the run time would be doubled, the computational cost would only be one quarter. Additionally, a set of 480 processors is most likely less available than 120, which may lead to longer job queue times. It may also be more efficient to simulate a case like the Columbia River basin in several large subbasins, particularly for calibration and validation. Once calibrated, the parameters could be used in a “production” simulation of the entire Columbia Basin.

Additional analysis (not reported here) indicates that the way meteorological forcing was read and applied was the largest single obstacle to higher parallel performance. Reading the meteorological data in larger blocks, a day or month at a time, say, rather than one time step at a time, may reduce input time. Reading 2D map data in parallel, instead of through the root process, may also be a solution.

Stream routing took a significant part of the total run time for the Columbia simulation. The choice to keep this a serial process, executed by all processes, may be acceptable for smaller basins, and was acceptable for the cases here, but may become a barrier with larger applications. Parallel methods to perform channel routing will be investigated in future work.

We have used a straightforward and relatively simple domain decomposition scheme here. A more extensive investigation of domain decomposition would likely yield further performance improvements. We have assumed that the simulation of each “active” cell has an equivalent computational cost. This is not strictly true. Cells with snow definitely have a higher computational cost than cells without snow. Such an investigation would require some detailed analysis of run times and how snow increases the computational cost of an active cell.

4.0 DHSVM-MASS1 Integration

In smaller tributaries, riparian vegetation may strongly influence stream temperature through its impact on the energy balance at the water surface. This is especially true during periods of low flow when canopy shading extends over most, or all, of the channel. Many (most) hydrodynamic river models are developed for larger channels and typically ignore the effect of riparian vegetation on stream temperature and linkage to a hydrologic model is generally through inflow to the channel network at a limited number of "nodes", or subbasin outlets. We have addressed these two limitations through the integration of MASS1 into the parallel version of DHSVM as described below.

DHSVM provides the rate and temperature of lateral inflow to the channel network that is represented as a series of stream segments. The Modular Aquatic Simulation System in 1-Dimension (MASS1; Richmond and Perkins 2002) simulates stream flow and water quality (including temperature) in branched stream networks composed of stream segments. Integration of the two models requires a common representation of the channel network. A DHSVM stream segment is specified by (1) a unique segment identifier, (2) a class identifier, (3) a segment length, (4) an average segment slope, and (5) a downstream segment identifier. The stream segments are grouped by "class," which defines rectangular channel properties: (1) width, (2) bank full depth, and (3) Manning's roughness coefficient. DHSVM stream networks are prepared from a stream network GIS layer using a set of stream preprocessing scripts distributed with the DHSVM source code.

After surface and subsurface routing (Perkins et al. 2019) is complete, computed stream channel interception of surface and subsurface flow is accumulated for each cell in which a stream channel lies. The intercepted water volume is summed and used as lateral inflow for each stream segment. This inflow is routed through the stream network using a cascade of linear reservoirs. The outflow rate of segment i at time t + 1 is given by

$$O_i^{t+1} = \left(I_i^{t+1} + L_i^{t+1}\right) - \left(S_i^{t+1} + S_i^t\right)\frac{1}{\Delta t} \tag{4.1}$$

where

I_i^t = the inflow rate at time t to segment i from upstream segment(s),
L_t = the lateral inflow at time t into segment i,
Δt = the time step between t and t + 1, and
S_i = the segment storage at time t, computed using

$$S_i^{t+1} = \frac{1}{K^t}\left(I_i^{t+1} + L_i^{t+1}\right) + X^t\left[S_i^t - \frac{1}{K^t}\left(I_i^{t+1} + L_i^{t+1}\right)\right]) \tag{4.2}$$

in which

$$K^t = \frac{\sqrt{S_o}}{nl}R^{2/3}$$

and

$$X^t = e^{-K^t \Delta t}$$

where

S_o = the segment slope,
n = coefficient,

l = the segment length, and
Δt = the time step.

R is the hydraulic radius, which is assumed constant corresponding to channel depth at 75% of the bank full height so that K^t is constant over time.

Similar to lateral inflow, meteorologic variables used for the stream temperature heat budget are aggregated from those in the cells in which the segment lies. This includes the effects of topographic and riparian shading on short and longwave radiation (Sun et al. 2015).

4.1 MASS1

The Modular Aquatic Simulation System in 1-Dimension (MASS1; Richmond and Perkins 2002) simulates stream flow and water quality in branched stream networks. MASS1 has been applied to a variety of river regulation and water quality problems (e.g., Perkins and Richmond 2001; Richmond et al. 2002; Richmond and Perkins 2002; Tiffan et al. 2002; McMichael et al. 2008; Niehus et al. 2014; Bellgraph et al. 2016; Shuai et al. 2019). MASS1 is coded in object-oriented Fortran 2008. MASS1 code is distributed with DHSVM to ease compilation.

The MASS1 stream network is, like DHSVM, composed of segments organized into a branched network. Points are defined along those segments. At each point, the bathymetry is defined using a cross section, which can be any of a number of prismatic shapes (rectangular, triangular, parabolic, etc.) or a list of station/elevation points.

But, unlike DHSVM, each segment can have a type that determines how hydrodynamic and thermal transport physics are represented, namely “hydraulic,” or “hydrologic”. Both hydraulic and hydrologic segments represent energy exchange with the atmosphere using the same methods.

4.1.1 Hydraulic Segments

MASS1 hydraulic segments provide a detailed representation of the stream channel, both in terms of bathymetry or morphology and physics. Any number of points can be used along the segment and typically measured, general cross sections are used, but prismatic sections are also valid.

MASS1 simulates steady and unsteady flow in hydraulic segments by solving the one-dimensional, cross-section-averaged equations of mass conservation,

$$\frac{\partial A}{\partial t} + \frac{\partial Q}{\partial t} = 0 \tag{4.3}$$

and momentum conservation,

$$\sigma\left[\frac{\partial Q}{\partial t} + \frac{\partial}{\partial x}\left(\alpha\frac{Q^2}{A}\right)\right] + gA\frac{\partial y}{\partial x} + gAS_f = 0 \tag{4.4}$$

where

A = the channel cross-sectional area,
Q = the channel discharge,
Y = the water surface elevation,
G = the gravitational acceleration,

S_f = the friction slope,
α = momentum correction factor,
t = time, and
x = distance along the channel.

Equation (4.4) uses the local partial inertia technique (LPI; Fread et al. 1996), in which σ is used as a numerical filter reducing or eliminating the inertial terms depending on the local Froude number (F_r):

$$\sigma = \begin{cases} 1 - F_r^m & (F_r \leq 1.0, m \geq 1.0) \\ 0.0 & (F_r > 1.0) \end{cases} \tag{4.5}$$

Together, Equations (4.3)) and (4.4 are often referred to as the St. Venant equations (Cunge et al. 1980). The friction slope is expressed in terms of the discharge and channel conveyance (K) as

$$S_f = \frac{Q|Q|}{K^2} \tag{4.6}$$

where K is computed using the Manning equation (Chow 1959) as

$$K = \frac{C_o}{n} A R^{2/3} \tag{4.7}$$

where C_0 is 1.49 for English units or 1.0 for metric units; n is the Manning channel roughness coefficient; and R is the channel hydraulic radius, which is

$$R = \frac{A}{P}$$

where P is the channel wetted perimeter. Equations (4.6) and (4.7) represent the combined effects of variable channel geometry and resistance to flow (roughness).

Hydraulic segments can be used to simulate a wide range of open channel flow regimes. Because the complete representation of momentum (Equation (4.4)) is used, hydraulic segments can simulate flow situations like reverse flow, wave travel, and back water. The use of the LPI technique (Equation (4.5)) allows reliable simulation of trans- and super-critical flow with some loss of accuracy. Hydraulic segments cannot be used if the discharge becomes very low or zero.

Energy transport in hydraulic segments is represented using

$$\frac{\partial(AT)}{\partial t} + \frac{\partial(QT)}{\partial x} = \frac{\partial}{\partial x}\left(K_T A \frac{\partial T}{\partial x}\right) + \frac{B \sum H}{c_p \rho} \tag{4.8}$$

where

$\sum H$ = surface flux of thermal energy,
K_T = the longitudinal dispersion coefficient,
ρ = density of water, and
c_p = specific heat of water.

Temperature can be the transported quantity because c_p is assumed constant. An explicit total variation diminishing (TVD) scheme based on that of Gupta et al. (1991) and a (non-iterative) split-operator method (Carrayrou et al. 2004 for example) is used to solve Equation (4.8) with finite volume discretization.

4.1.2 Hydrologic Segments

Hydrologic segments are limited to two points, upstream and downstream, and both points are required to have the same cross section. Rectangular cross sections were used in this work, but any type of cross section available in MASS1 can be used, including general cross sections described by station-elevation pairs.

Streamflow routing in hydrologic segments is performed as described above for DHSVM, except that the conveyance, *Kt* (Equation (4.1), is computed using the current segment outflow, O_t. To obtain the necessary cross-section properties, normal flow is assumed and an iterative procedure (Shirley and Lopes 1991) is used to determine normal depth from discharge. In this procedure, discharge, *Q*, is

$$Q_o = C_f A^{\alpha} P^{-\beta} \tag{4.9}$$

in which, when Manning's equation is used,

$$C_f = \frac{S_o^{1/2}}{n},\ \alpha = \frac{5}{3},\ \beta = \frac{1}{2} \tag{4.10}$$

where S_o is the channel slope, and *n* is Manning's coefficient. Under some specific conditions, *f* (*y*) is defined as

$$f(y) = A^{-1}\left[\left(\frac{Q_o}{C_f}\right)^{1/\alpha} P(y)^{\beta/\alpha}\right] \tag{4.11}$$

where *A*−1[] is the inverse area function for the cross section (i.e., a function given a cross-section area computes the corresponding stage), and Q_o is the discharge. This can be used iteratively, such that for each iteration *n*,

$$y^{n+1} = f(y^n) \tag{4.12}$$

will be closer to the actual solution, y_o, than y_n. This approach can be used for any cross-section type, provided the inverse area function is available or can be approximated (as with general cross sections). Shirley and Lopes (1991) present simplifications of Equation (4.11) for several cross-section types. For rectangular cross sections, Equation (4.11) reduces to

$$f(y) = a_2(a_1 + y)^{2/5} \tag{4.13}$$

where

$$a_1 = \frac{b}{2}$$

and

$$a_2 = \left[\left(\frac{nQ}{2\sqrt{S_o}}\right)^{3/5}\left(\frac{2}{b}\right)\right]^{1/3}$$

where b is the bottom width.

In this way, the normal depth is estimated at both the inflow (with I_i^t) and outflow (with O_i^t) points. The normal depth is used to compute cross-section properties, most importantly hydraulic radius, *R* and the top width.

Hydrologic segments use a simple compartment model for energy transport, which assumes the segment is a well-mixed volume in which the transported scalar mass is conserved. Mass conservation (ignoring diffusion and internal sources) for scalar *T* in segment *i* is

$$I_i^{t+1}T_{i_{in}}^{t+1} + I_i^{t+1}T_{i_{lateral}}^{t+1} - Q_i^{t+1}T_{i_{out}}^{t+1} = \left(S_i^{t+1}T_i^{t+1} - S_i^tT_i^t\right)\frac{1}{\Delta t}$$

where T_i^t is the temperature at time *t*, and $T_{i_{in}}^t$ and $T_{i_{out}}^t$ are the inflow and outflow temperatures at time *t*. If

$$T_{i_{out}}^{t+1} = T_i^{t+1}$$

is assumed (implicit upwind), then

$$T_i^{t+1} = \left[\Delta t I_i^{t+1}T_{i_{in}}^{t+1} + \Delta t L_i^{t+1}L_{i_{lateral}}^{t+1} + S_i^tT_i^t\right]\frac{1}{S_i^{t+1}+\Delta t O_i^{t+1}} \qquad (4.14)$$

This is very similar to the methods used by Cox and Bolte (2007) and Li et al. (2015).

Consistent with split-operator usage in hydraulic segments, the atmospheric exchange source term is included after transport. The compartment temperature is updated as

$$T_i^{t+1} = \left(T_i^{t+1}\right)^* + \frac{\bar{B}L\sum H}{c_p\rho V}\Delta t = \left(T_i^{t+1}\right)^* + \frac{\sum H}{c_p\rho\bar{d}}\Delta t$$

where

$\left(T_i^{t+1}\right)^*$ = the result of Equation (4.14),
$\bar{B}$ = the average top width of the segment,
L = the segment length,
$\bar{d}$ = the average depth over the segment (i.e., average of up- and downstream depth), and
$\sum H$ = the sum of atmospheric exchange fluxes.

Hydrologic segments provide a robust, numerically stable representation of open channel flow that is very close to the original DHSVM representation. Zero discharge is robustly simulated. The compartment model is very diffusive, but this is less of an issue for temperature because it is source-term dominated.

In both hydraulic and hydrologic segments, heat exchange at the water surface is computed as the net heat flux.

$$\sum H = H_{sn} + H_{an} - (H_b + H_e + H_c)$$

where

H = net surface heat flux,
H_{sn} = net solar short wave radiation,
H_{an} = net atmospheric long wave radiation, H_b long wave back radiation,
H_e = heat flux due to evaporation, and
H_c = heat flux due to conduction, all in W/m^2.

Individual fluxes are estimated as described by Edinger et al. (1974).

4.2 Methods

4.2.1 Flow Routing

Figure 4.1 depicts the MASS1 solution algorithm as it fits into DHSVM. Within a MASS1 time step, streamflow routing is computed using an implicit scheme at the full specified time step.

The MASS1 flow routing algorithm is based on a network composed entirely of hydraulic segments. Equations (4.3) and (4.4) are discretized for each segment using the well-known Priessman four-point implicit finite-difference scheme. The resulting nonlinear equations are solved using the double sweep method. This is a common approach to 1D hydrodynamic routing and described in detail by Cunge et al. (1980), Liggett and Cunge 1975, and others.

This traditional algorithm was modified to include hydrologic segments. Where hydraulic segments connect in the network, conservation of mass is enforced. In addition, water surface elevation is forced to be the same at that point for all connected segments. When hydrologic segments exist in the network, conservation of mass is still enforced. But routing in hydrologic segments depends only upon its own state, the only communication with other segments is inflow from upstream. Conditions in downstream segments have no effect. Consequently, when two or more hydrologic segments connect or a hydrologic segment is upstream of a hydraulic segment, discontinuity in water surface elevation is allowed. If a hydrologic segment is downstream of a hydraulic segment, then equal water surface elevation is enforced.

4.2.2 Temperature Simulation

The network temperature simulation algorithm is also based on a network comprised entirely of hydraulic segments. Because temperature in hydraulic segments is solved using an explicit scheme, in which the time step is limiting and usually required to be much smaller than the streamflow routing time step, a time substepping scheme is used as shown in Figure 4.1. Individual segments are solved in an upstream to downstream order and the sub-time step is computed to satisfy stability criteria (Courant and diffusion numbers) for all segments.

Hydrologic segments are incorporated into this algorithm. Hydrologic segments temperature simulation does not require substepping for stability. Because of the upstream to downstream march, the temperature time step in hydrologic segments downstream of hydraulic segments must be that of the hydraulic segments. However, if the hydrologic segments are upstream, they are solved at the full stream routing time step and their outflow to downstream hydraulic segments interpolated at each substep.

4.2.3 DHSVM/MASS1 Integration

In general, DHSVM/MASS1 can be used by an experienced DHSVM user, with little knowledge of MASS1. MASS1 requires a separate configuration, some of which is overridden by the DHSVM configuration. The original DHSVM stream network input remains necessary. The MASS1 configuration duplicates a representation of the DHSVM network. Care must be taken to confirm the MASS1 network matches the DHSVM network in terms of segment identifiers and connectivity. A simple utility has been supplied that creates a MASS1 configuration from DHSVM stream network files. This utility creates a duplicate MASS1 network from the DHSVM network using hydrologic segments only (Figure 4.1). The MASS1 network can be created for use with DHSVM/MASS1, or with added boundary conditions and lateral inflows specified, it can be run by MASS1 alone.

The integration of DHSVM and MASS1 was primarily done by a coding library with an API around the MASS1 code. For simplicity, MASS1 source code is distributed with DHSVM, but its use is completely optional. The use of MASS1 requires that it be compiled into DHSVM, but even then, the original DHSVM stream network can be used and MASS1 ignored.

At simulation startup, DHSVM causes MASS1 to read its configuration and prepare a network. Figure 4.1 shows a schematic of the DHSVM/MASS1 stream routing process that occurs within a DHSVM time step. After watershed simulation, necessary stream segment inputs and conditions are prepared. Surface runoff and subsurface interception are summed into each segment's lateral inflow.

4.3 Results and Discussion

This effort represents a significant advancement by allowing distributed inflows from the watershed to the channel network and an explicit representation of riparian vegetation of stream temperature. Each cell's meteorological conditions are accumulated and averaged over the segment. This is the same internal facility that was introduced in when integrating the particle tracking stream temperature model River Basin Model (RBM) with DHSVM (Sun et al. 2015; Yearsley et al. 2019), but the accumulated values are not saved to files. Consequently, short and long wave radiation is adjusted for topographical and canopy shading and, if specified, riparian shading as described by Sun et al. (2015). Internally, MASS1 maintains tables of time-varying lateral input (flow and temperature) and meteorological variables for each segment. Each segment is assigned a constant (in time) inflow temperature which can vary spatially. This approach can be improved through the approach of Yan et al. (2021) who assigned a segment inflow temperature of 0.1 degrees Celsius when DHSVM simulated local melt for a river segment exceeded a user-specified depth threshold; inflow temperature was based on air temperature during times without snowmelt.

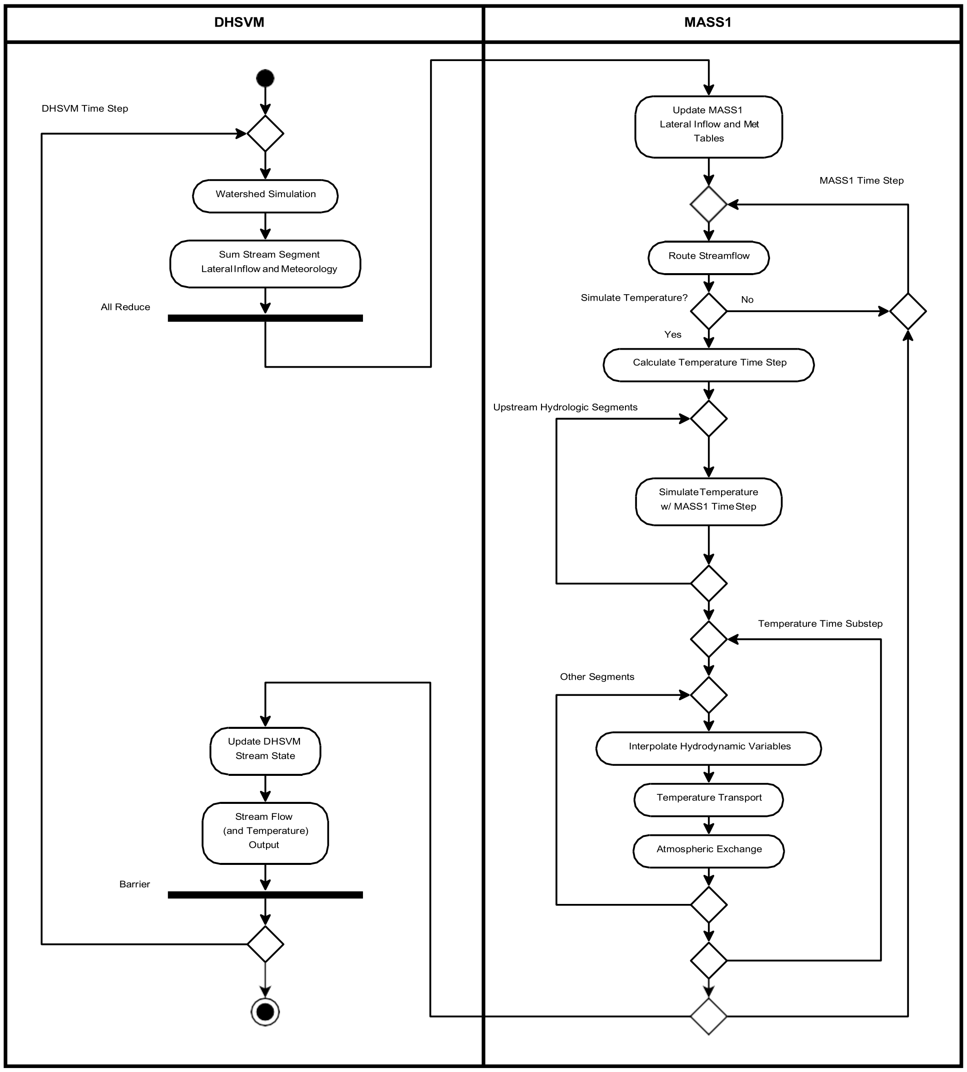

Figure 4.1. Simplified activity diagram depicting streamflow and temperature simulation and the roles of DHSVM and MASS1 code in that simulation.

5.0 Columbia River Unregulated Flow Application

The Columbia River Basin covers 258,000 square miles and includes parts of seven states and one Canadian province. In its 1,200-mile course to the ocean, the river flows through four mountain ranges and drains more water to the Pacific Ocean than any other river in North or South America. The river also provides drinking water to numerous communities along its course and irrigates 600,000 acres of farmland. Between the United States and Canada, the river's 19 hydroelectric dams provide about half the region's supply of electricity, in addition to providing flood control benefits.

In this section, we discuss application of the WRF model and the integrated DHSVM/MASS1 model to the basin under current and future climate conditions. We examine the impacts of climate change on **unregulated** streamflow and water temperature. The insight is complementary to ongoing efforts on the impact of climate change on the basin's hydropower as part of DOE led Secure Water Act focusing on federal hydropower and by the River Management Joint Operating Committee (RMJOC) efforts focusing exclusively on the region.

5.1 Methods

5.1.1 Climate

5.1.1.1 Historical Climate

Preliminary model testing with gridded WRF data indicates that although WRF could represent the basin-scale climate conditions reasonably well, its mesoscale nature limits its performance at the watershed scale where the hydrologic model is applied. To take advantage of the climate performance of the WRF simulation and high temporal resolution while making it suitable at the watershed scale, bias-correction is applied to adjust the WRF model output and make it more consistent with the ground measurements.

Precipitation from WRF (P_{WRF}) was bias-corrected (P_{WRF-BC}) using the Livneh et al. (2013) historical data set and the bias-correct spatial downscaling (BCSD) quantile mapping approach. At a given WRF grid in a given month, all the valid daily precipitation records based on a threshold (i.e., $P > P_0$) from WRF and Livneh are collected (resulting in two 33-month records during 1981–2013), and are used to construct two cumulative distribution functions (CDFs), namely F_{WRF} and F_{Livneh}, respectively. Then we used a quantile mapping approach to find the corresponding $P_{WRF-BC}$for each P_{WRF}, to have the following relationship:

$$F_{WRF}(P_{WRF}) = F_{Livneh}(P_{WRF-BC})$$

We also applied a $P_0 = 0.01mm/day$ as a filter to remove unrealistic "numerical precipitation" (such as the daily precipitation of 10^(-7) mm/day) in the WRF data. Therefore, for any given day with P < 0.01 mm/day, we set all the hourly precipitation that day to zero. For the rest of days, we computed the correspondingP_{WRF-BC}, then applied the ratio P_{WRF-BC}/P_{WRF} to each hourly WRF precipitation record of that day.

The adjustment of temperature (T) follows a procedure similar to that for precipitation. It is also on a grid basis. Because there is no need to filter temperature, the threshold is not used here. For temperature bias-correction, to keep the climate change signal from WRF and make the method applicable to future simulation, we first detrend the time series of daily T at each grid (x,y). We computed the regression as

$$T(x,y) = k(x,y) \cdot t + T_{intercept}(x,y)$$

And then derived the residual as

$$T'(x,y) = T(x,y) - k(x,y) \cdot t - T_{intercept}(x,y)$$

At a given grid and a given month, all the residual records (T') from WRF and Livneh are collected (so two 33-month records during 1981–2013), and are used to construct two CDFs, namely F_{WRF} and F_{Livneh}, respectively. Then we used quantile mapping to find the corresponding T'_{WRF-BC} for each T'_{WRF}, to have the following relationship:

$$F_{WRF}(T'_{WRF}) = F_{Livneh}(T'_{WRF-BC})$$

Adding the regression back, we have the following final adjusted T:

$$T_{WRF-BC} = T'_{WRF-BC} + k_{WRF}(x,y) \cdot t + T_{WRF-intercept}(x,y)$$

Based on our evaluation, WRF has some bias in the simulation of long-term climate ($T_{intercept}(x,y)$). Thus we further improved the bias-corrected T'_{WRF-BC} above by adjusting this long-term climatic bias ($T_{Livneh-intercept}(x,y) - T_{WRF-intercept}(x,y)$) as follows:

$$T_{WRF-BC} = T'_{WRF-BC} + k_{WRF}(x,y) \cdot t + T_{WRF-intercept}(x,y) + (T_{Livneh-intercept}(x,y) - T_{WRF-intercept}(x,y))$$

A comparison of the bias-corrected WRF precipitation and the Livneh data set (2013) indicates that the largest, mostly positive, percent differences occur for the winter months (Figure 5.1). The temperature bias-correction first detrends the data sets using a linear regression and then performs bias-correction on residuals of the data sets. The temperature difference between the bias-corrected WRF and Livneh data show much less seasonality, generally between plus or minus 1 degree Kelvin depending on location (Figure 5.2).

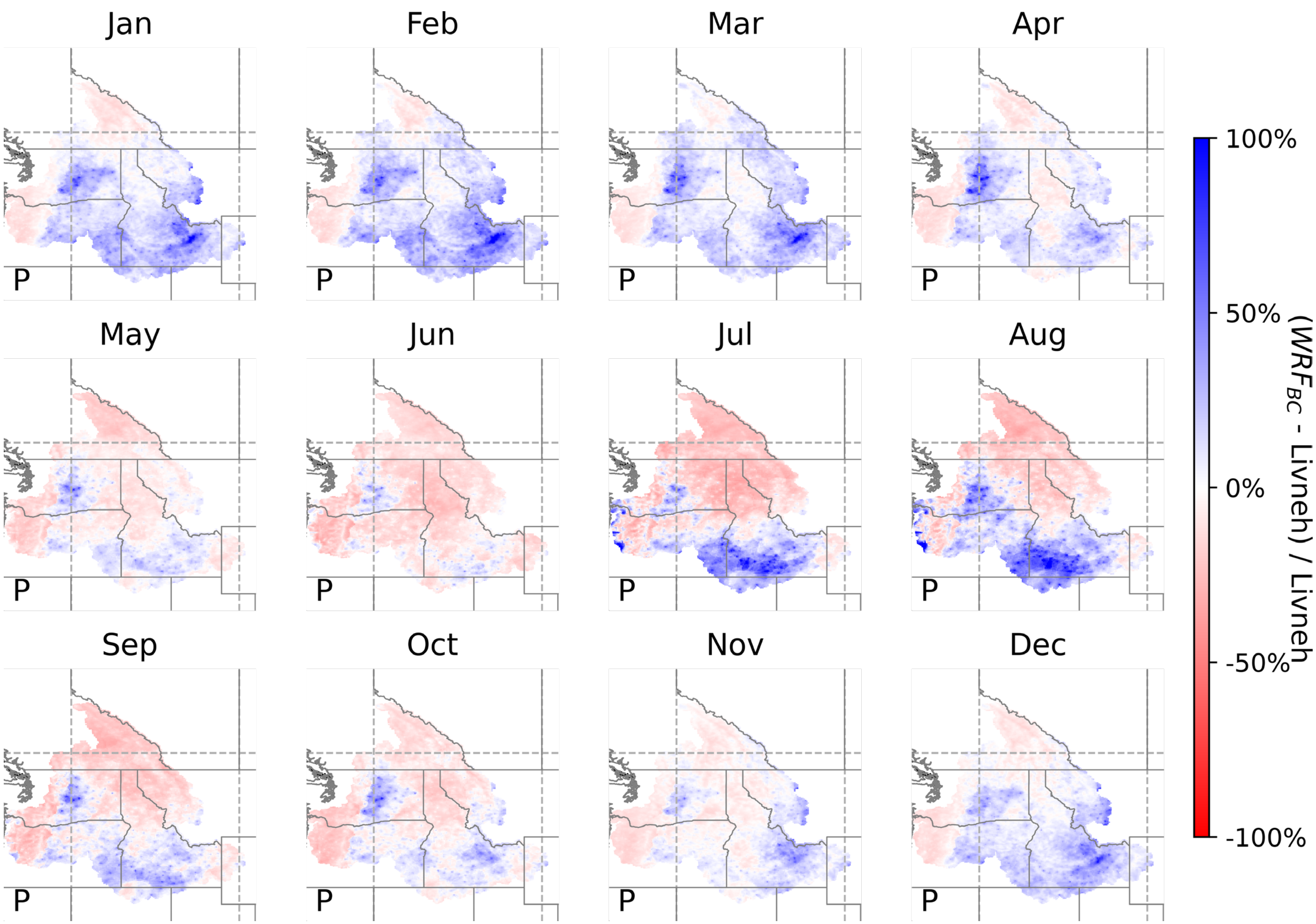

Figure 5.1. Effect of bias correction on WRF precipitation denoted by *P*. Dashed lines define longitudinal and latitudinal grids, solid lines are state boundaries.

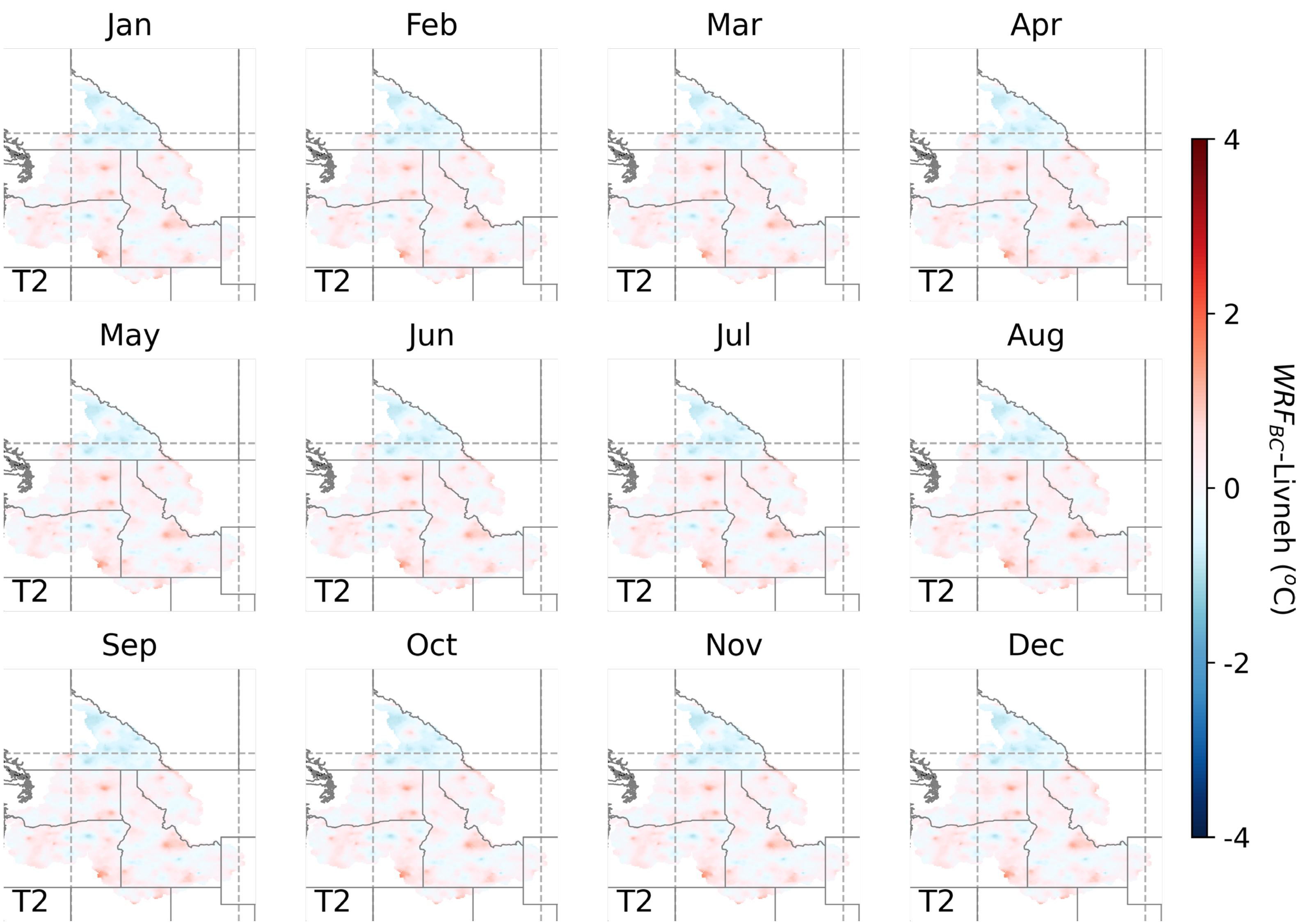

Figure 5.2. Effect of bias correction on projected air temperature at 2m (T2). Dashed lines define longitudinal and latitudinal grids, solid lines are state boundaries.

5.1.1.2 Future Climate

We applied the same percentile-based bias-correction to future climate precipitation and temperature using ratio/delta derived from historical data for all five CMIP5 GCMs: CanESM2, CESM1-CAM5, GFDL-ESM2M, HadGEM2-ES, MPI-ESM-MR (Table 5.1) for the time period of 2040–2070. The assumption of bias-correcting future data is that WRF model biases (in precipitation and temperature) share a similar structure between historical and future periods, thus the ratios (for precipitation) and deltas (for temperature) are applicable to future simulation results. The procedure of adjusting the detrended temperature residuals while keeping the long-term trends maintains the raw climate change signal as reflected in the WRF dynamic simulation, and thus the value of the dynamic simulation.

Table 5.1. Descriptions of GCMs applied in the Columbia River Basin

GCMs	Description
CanESM2	Canadian Earth System Model v2
CESM1-CAM5	Community Atmospheric Model version 5
GFDL-ESM2M	Global Fluid Dynamical Lab Environmental System Model v2
HadGEM2-ES	Hadley Centre Global Environmental Model v2 – Earth Systems
MPI-ESM-MR	Max Planck Institute for Meteorology Earth System Model MR

As shown in Figure 5.3 and Figure 5.4, future precipitation generally exceeds historical (Livneh 2013 and North American Regional Analysis [NARR)] data) with more variation in December and January, while future temperature exceeds historical in all months, by 3–5 degrees depending on the season and GCM.

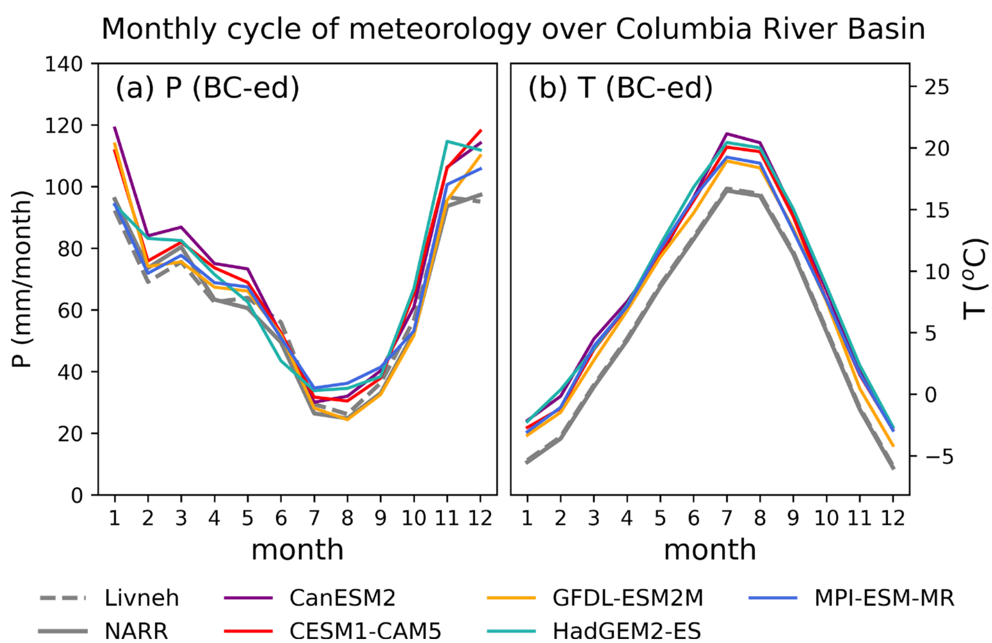

Figure 5.3. Mean monthly precipitation and air temperature over the Columbia River Basin

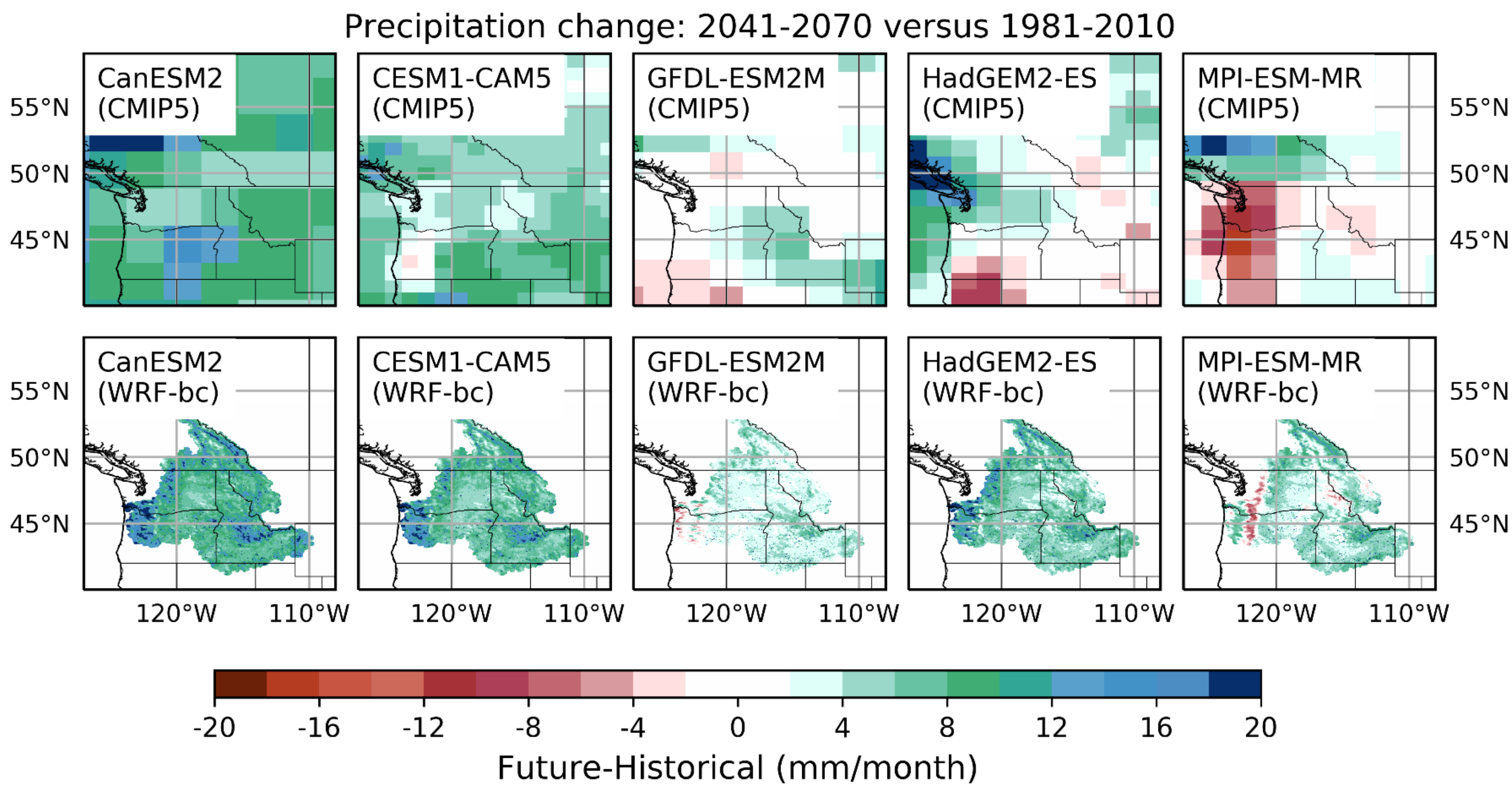

Figure 5.4. Change of long-term mean monthly precipitation between 2041-2070 and 1981-2010, as simulated by the selected CMIP5 models (top row) and the corresponding bias corrected WRF downscaled changes (bottom row).

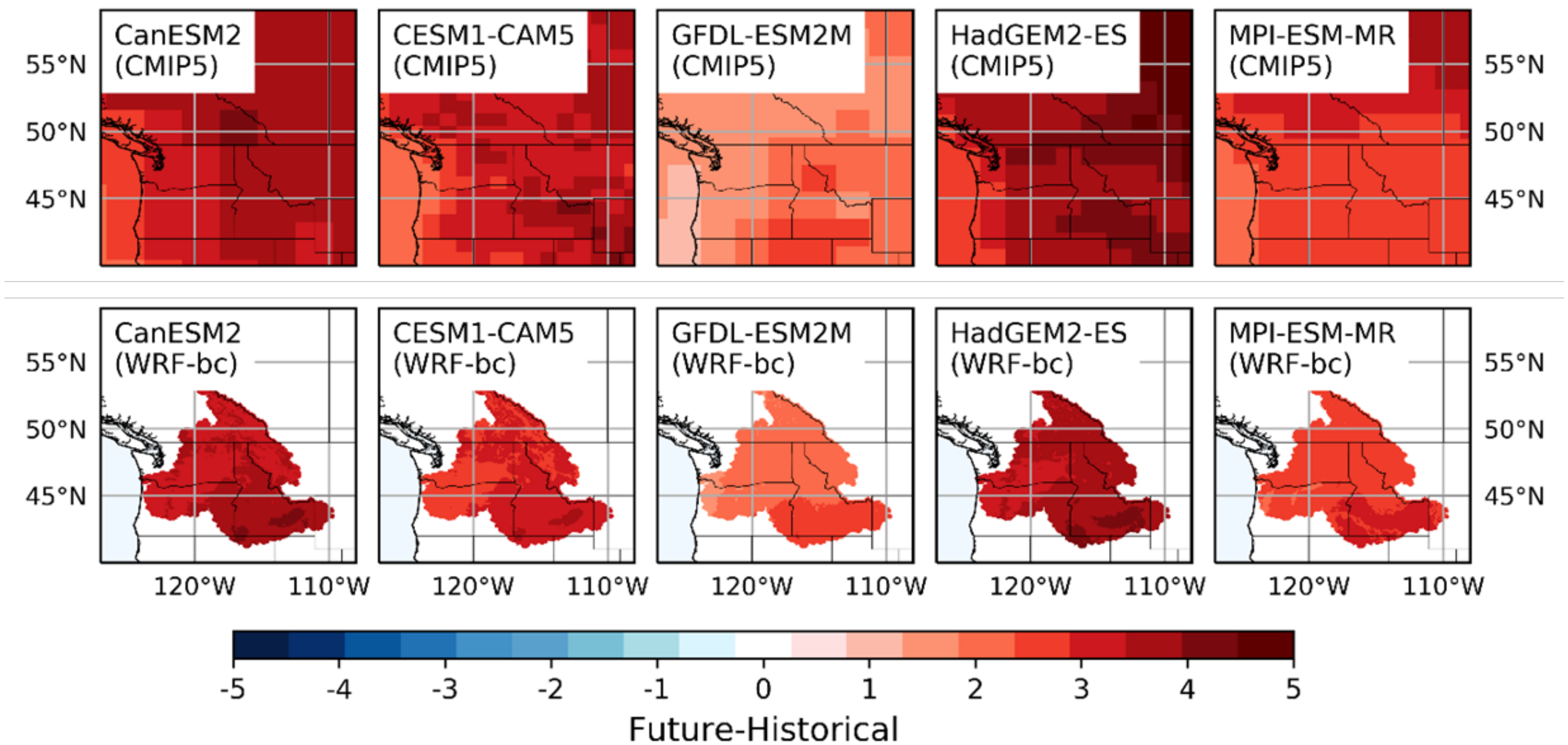

Figure 5.5. Change of long-term mean monthly near-surface temperature between 2041-2070 and 1981-2010, as simulated by the selected CMIP5 models (top row) and the corresponding bias corrected WRF downscaled changes (bottom row).

5.1.2 Watershed Modeling

The integrated DHSVM/MASS1 was applied to the entire Columbia Basin at a 90 m spatial resolution (Figure 3.4) resulting in 83 million active model grid cells and more than 20,000 channel reaches. The basin stream network was generated using the Python-based DHSVM preprocessing module, which calculates and extracts accumulated flow lines based on flow direction as derived from the DEM. Hydrologic segment cross-section sizes were estimated for each channel segment using upstream drainage area and relationships for bank full channel width and depth given by Castro and Jackson (2001). These were grouped into 22 classes. Hydraulic segments were used where river bathymetry, in the form of cross sections, was available to the authors from previous work. This included the Columbia River from the U.S.-Canada border to the mouth, the Snake River from Anatone, Washington, to the mouth, and the Clearwater River from Orofino, Idaho, to the mouth (Richmond et al. 2000; Perkins and Richmond 2001; Perkins et al. 2002; Niehus et al. 2014; and others). The numbers of hydraulic segments and cross sections used for these rivers are shown in Table 5.2. Channel roughness was taken from previous MASS1 simulations.

Table 5.2. Columbia Basin stream network summary based on segment type.

Reach	Number of Segments	Length (km)	Number of Cross Sections
Columbia River	230	1,199.5	1,836
Snake River	40	272.2	387
Clearwater River	11	65.6	78
Total	281	1,537.3	2,301
Remaining	18,543	127,500	
Basin Total	20,844	129,800	

5.2 Results

5.2.1 Streamflow

5.2.1.1 Model Calibration

The meteorological data set of Livneh et al. (2015) was used to drive the model calibration and validation. This data set contains precipitation, maximum and minimum temperature and wind speed; the remaining meteorology forcing needed by the model (longwave, shortwave, and relative humidity) were generated using the MTCLIM microclimate simulation model (Hungerford et al. 1989).

The model was calibrated specifically at eight subbasins (Figure 5.7) to represent basin-specific hydrologic processes that resulted from spatially varied snow, soil, and vegetation parameters. The flows from the subbasins account for approximately 70% of the total flow in the Columbia

River Basin at The Dalles according to the No Regulation-No Irrigation (NRNI; BPA 2017) data set developed by the Bonneville Power Administration (BPA) to represent unregulated flow by removing impacts from irrigation and reservoir regulation. The model calibration period was from WY1983 to 1987 and validation period from WY1988 to 1992. The parameter values for the remainder of the basin were initialized with mean values based on the final parameters from the calibrated basins and were then further refined with additional basin wide model calibration.

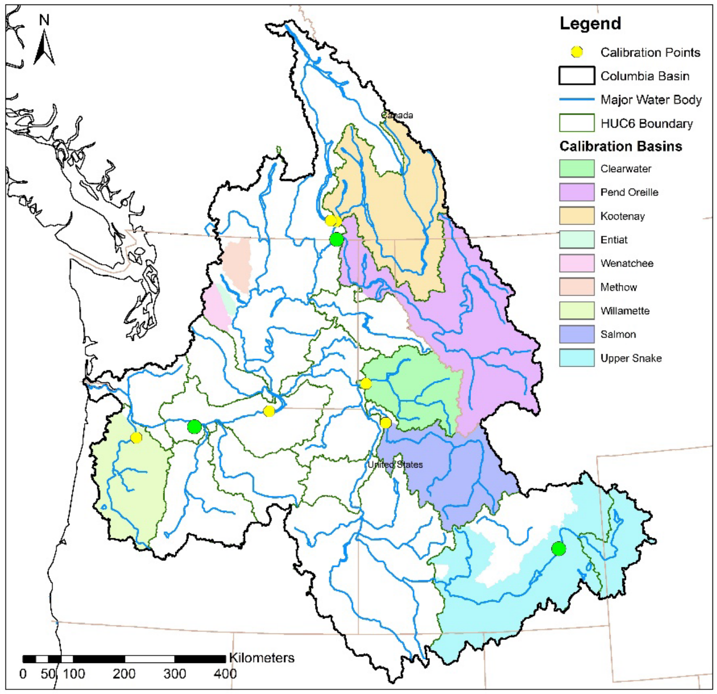

Figure 5.6. Columbia River Basin Model Domain and subbasins considered for calibration.

The simulated daily and monthly hydrograph at The Dalles shows a good match with the reconstructed NRNI streamflow with Nash-Sutcliffe model Efficiency coefficient (NSE) for daily streamflow is 0.696 during calibration and 0.773 during validation. The NSE is commonly used in hydrology to evaluate the agreement between predicted streamflow and observed streamflow. The NSE can range between negative infinity and 1. An efficiency of 1 (NSE = 1) corresponds to a perfect match of modeled discharge to the observed data. An efficiency of 0 (NSE = 0) indicates that the model predictions are as accurate as the mean of the observed data, whereas an efficiency less than zero (E < 0) occurs when the observed mean is a better predictor than the model. The NSE for daily mean and monthly averages simulation results over the period is 0.73 and 0.89 correspondingly (Figure 5.8). Calibrated hydrographs (Figure 5.9) and the of calibration statistics (Table 5.3) for subbasins also shows a good match with the reference NRNI data.

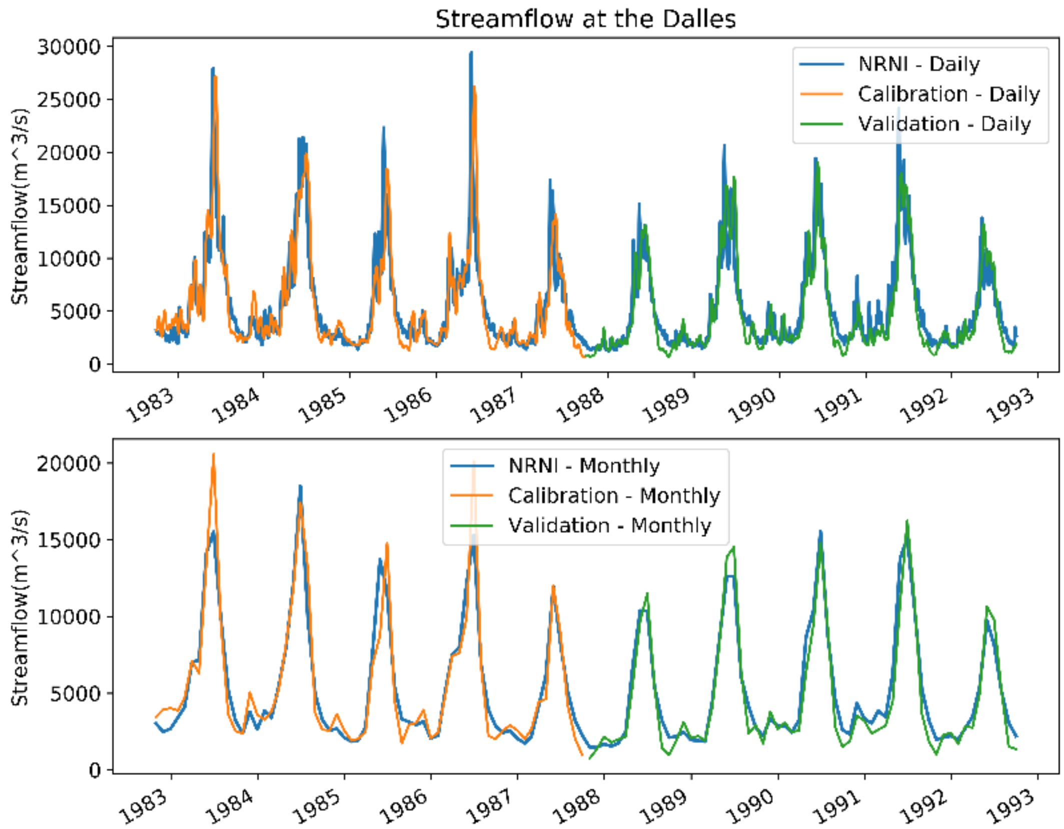

Figure 5.7. Simulated vs. NRNI hydrograph at The Dalles at daily and monthly resolution.

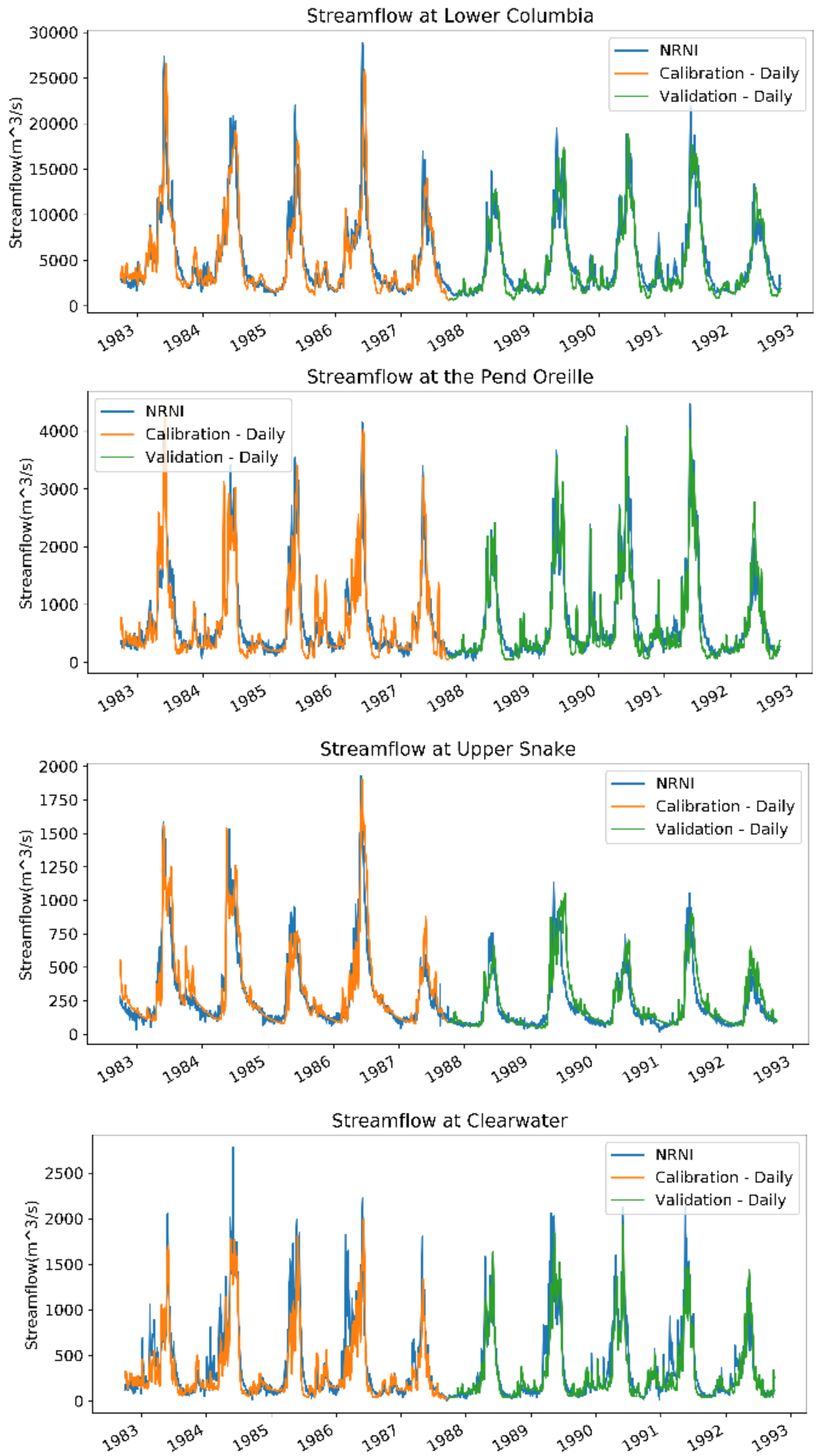

Figure 5.8. Hydrograph of simulated vs. NRNI streamflow at example calibrated watersheds at daily resolution.

Table 5.3. NSE for daily streamflow at sample calibration locations.

	Calibration WY1983 – WY1987	Validation WY1988 – WY1992	Overall WY1983 – WY1992
Subbasins	**NSE**	**NSE**	**NSE**
The Dalles	0.70	0.77	0.73
Lower Columbia	0.74	0.81	0.77
Upper Snake	0.84	0.67	0.81
Pend Oreille	0.80	0.84	0.82
Clearwater	0.80	0.84	0.82

5.2.1.2 Simulated Streamflow using WRF

We then drive the DHSVM model with the bias-corrected WRF historical simulation at hourly time steps for the same 10 years (WY1983–1992) in the major subbasins of the Columbia River Basins (using the calibrated parameter sets based on the Livneh meteorological data). This allows for a more direct comparison between historical and future climate conditions because both are based on the WRF model output. As would be expected, there are some differences in streamflow when using the two different meteorological data sets. For example, the streamflow hydrograph at The Dalles shows a slightly earlier peak and recession with the WRF data (Figure 5.10), which results in a lower NSE and an increased bias (Table 5.4). The performance of bias-corrected WRF data in subbasins is also shown in Figure 5.11 and the NSEs are summarized in Table 5.5.

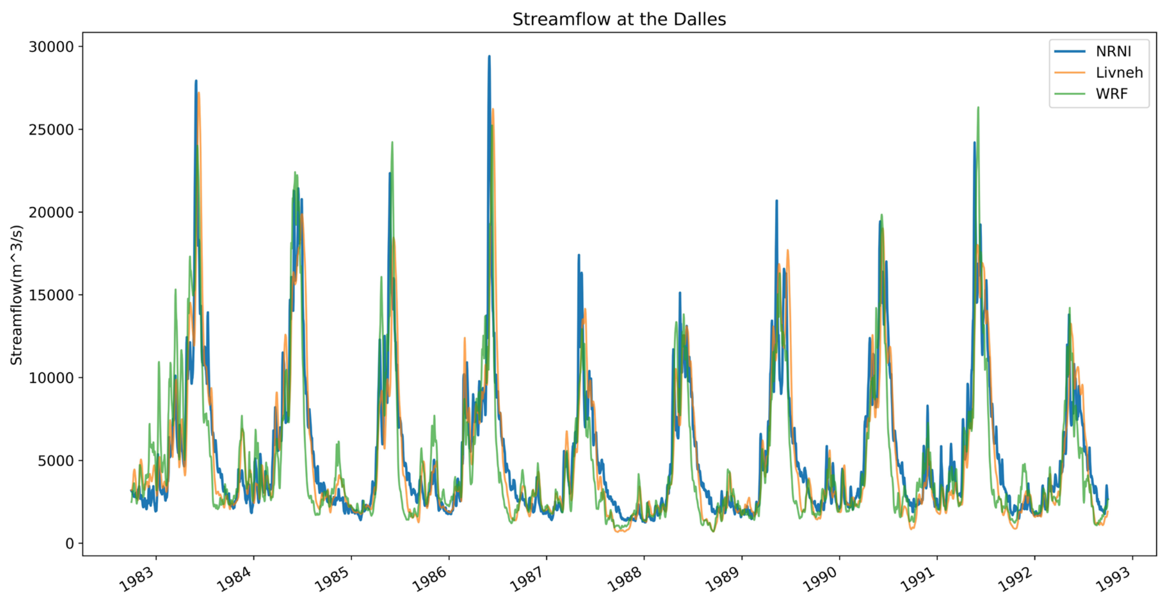

Figure 5.9. Hydrograph for daily streamflow at The Dalles driven by Livneh and WRF.

Table 5.4. Statistics comparison for daily streamflow at The Dalles driven by Livenh and WRF.

Forcing	NSE	Percent Bias	Mean Absolute Error (m^3/s)
Livneh	0.73	-3.16%	1389
WRF	0.70	-7.37%	1655

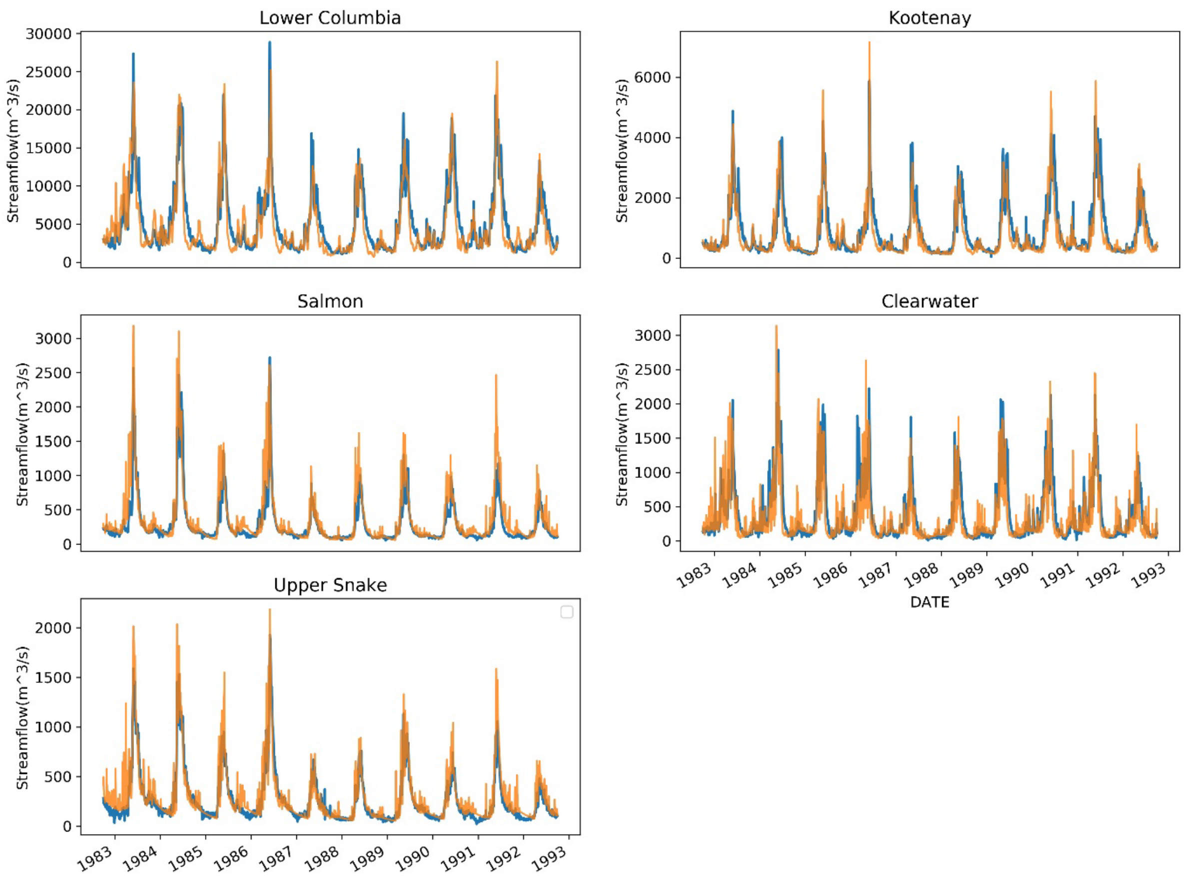

Figure 5.10. Hydrograph for daily streamflow at subbasins driven by bias-corrected WRF data.

Table 5.5. NSEs for daily streamflow at sample calibration locations with bias-corrected WRF forcing.

	Lower Columbia	Kootenay	Salmon	Clearwater	Upper Snake
NSE	0.72	0.76	0.64	0.67	0.81

5.2.1.3 Historical and Future Unregulated Flow

After model calibration and validation, both the historical and future bias-corrected WRF climate forcings were used to drive to the integrated DHSVM/MASS1 model to translate the climate signals to streamflow responses. At most locations, the Columbia River Basin responses to the projected future climate scenarios with shifts in timing, including higher winter flow and lower late spring/early summer flows, with some variation in detailed model response between the future climate ensemble members (Figure 5.12).

The streamflow trends are consistent with the temperature and precipitation trends from the GCMs. For example, the CanESM2 scenario shows the highest flow increase from January through May in Figure 5.12, which is consistent with the precipitation change pattern shown in Figure 5.3. The GFDL-ESM2M scenario shows overall less increase in warming and precipitation, therefore the changes at The Dalles under this scenario also show less of an increase in flow and a minor shift in the timing of the flow peak.

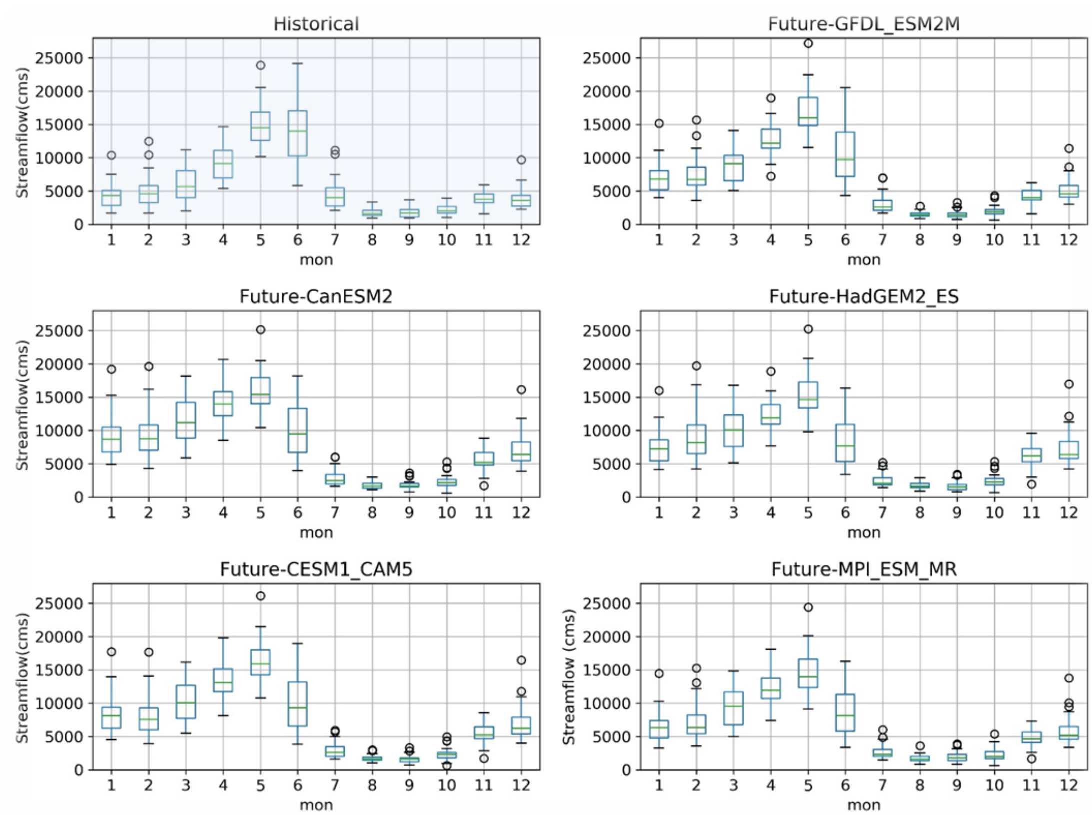

Figure 5.11. Monthly flow statistics at The Dalles for historical and future runs.

The spatial map shows that both GFDL_ESM2M and MPI_ESM_MR yield lower overall precipitation increases, while the monthly precipitation pattern shows GFDL has more monthly variation than MPI (higher increase in winter/spring months while less increase or even decrease in summer months).

The impacts of climate change on streamflow peaks varies by subbasin (Figure 5.13): The Dalles, Upper Snake, Kootenays all show earlier and higher spring peaks among all scenarios. The Clearwater, Pend Oreille, and Salmon show earlier or similar peaks, but of similar magnitude compared to historical flow patterns, with variations of higher or lower by climate ensemble. In the north Cascade region, the Wenatchee shows lower spring peaks while the Entiat shows spring peaks of similar timing and magnitude, with shifts in the timing of the overall flow. The Willamette River Basin is historically rain dominant and peak flows occur in winter months. With changes in climate, the flow in the Willamette Basin shows higher winter flows and peaks, while spring flows show little change or even a slight decrease for late spring months compared with other subbasins.

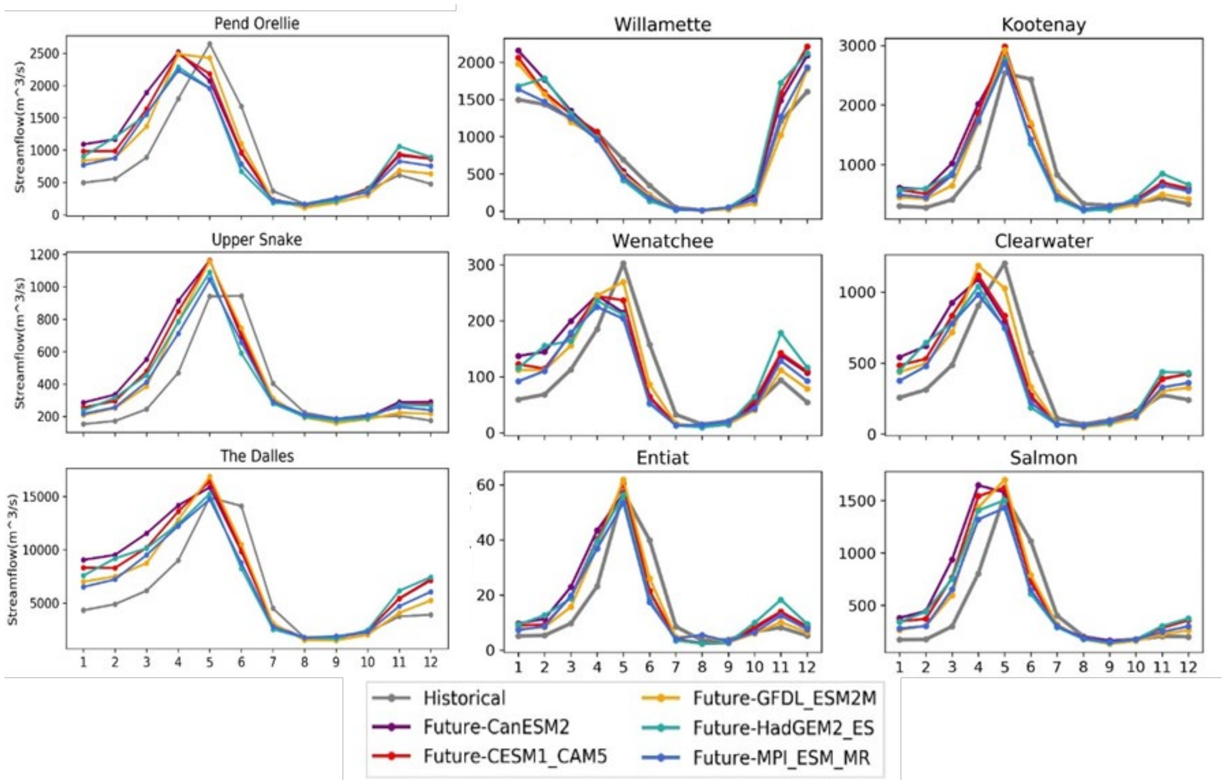

Figure 5.12. Monthly averaged streamflow (in cubic meter per second) for historical and five future GCMs.

5.2.2 Water Temperature

5.2.2.1 Model Calibration

After calibrating and validating streamflow, the simulation of stream temperature was calibrated and validated in a similar manner. As with streamflow, several subbasins were simulated individually (Figure 5.14). In these subbasins, one or more U.S. Geological Survey (USGS) temperature gages on unregulated, or streams with minimal regulation that had at least a 3-year record were chosen. Daily average temperatures from these gages were compared to daily averages of simulated temperatures.

Coefficient sets were established for each of the subbasins. The same coefficient set was assigned to all stream network segments within the corresponding subbasin. Simulations were performed and coefficients adjusted until the bias between observed and simulated daily average temperature was near zero. The subbasin coefficient sets were transferred to the larger stream network for full Columbia Basin simulations. The temperatures of lateral inflow from the land surface were based on average annual air temperature in each subbasin computed from the meteorologic forcing. In most subbasins the inflow temperature was unchanged, however this was also used for calibration in some areas.

After calibration, the entire Columbia Basin was simulated for the available historical period, using the calibrated coefficient sets, and comparison plots and statistics were prepared using the entire record of several temperature gages.

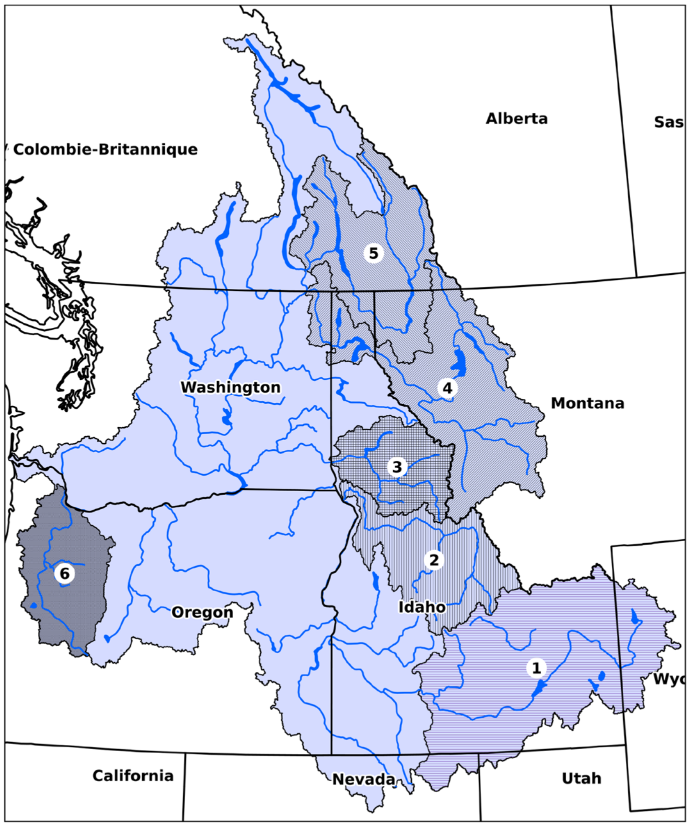

Figure 5.13. Subbasins for which temperature coefficients were calibrated and validated: Upper Snake (1), Salmon (2), Clearwater (3), Pend Oreille (4), Kootenai (5), and Willamette (6).

Temperature calibration and validation resulted in the meteorologic coefficient sets shown in Table 5.6. Figure 5.15 shows time series and scatter plots comparing simulated and observed daily average temperature in a few unregulated, or lightly regulated, streams from across the basin. In general, daily average temperatures in unregulated or lightly regulated streams were simulated with a mean absolute error of 1.5°C and NSEs greater than 0.7.

Constant coefficient sets were applied over relatively large regions. A more extensive calibration would probably require coefficient sets on the order of HUC 8 to at least account for inflow temperature variation. As described above, the temperatures of lateral inflow from the land surface were based on average annual air temperature in each subbasin computed from the meteorologic forcing. This approach can be improved through the approach of Sun et al. (2021) who assigned a segment inflow temperature of 0.1 degrees Celsius when DHSVM simulated local melt for a river segment exceeded a user-specified depth threshold; inflow temperature was based on air temperature during times without snowmelt.

Table 5.6. Calibrated meteorologic coefficients for stream temperature simulation in the Columbia Basin, including inflow temperature. Regions are shown in Figure 5.14. Subbasins for which temperature coefficients were calibrated and validated: Upper Snake (1), Salmon (2), Clearwater (3), Pend Oreille (4), Kootenai (5), and Willamette (6).. a_W, b_W, and C_c are wind function coefficients and the conduction coefficient, respectively.

Region		a_W	b_W	C_c	T_I, °C
1	Upper Snake	0.40	7.8	0.47	10.0
2	Salmon	0.17	3.5	0.47	5.0
3	Clearwater	0.35	6.9	0.47	6.0
4	Pend Oreille	0.65	13.5	0.47	4.0
5	Kootenai	0.24	4.6	0.47	3.0
6	Willamette	0.65	13.5	0.47	8.0
	Elsewhere	0.56	11.5	0.47	5.0

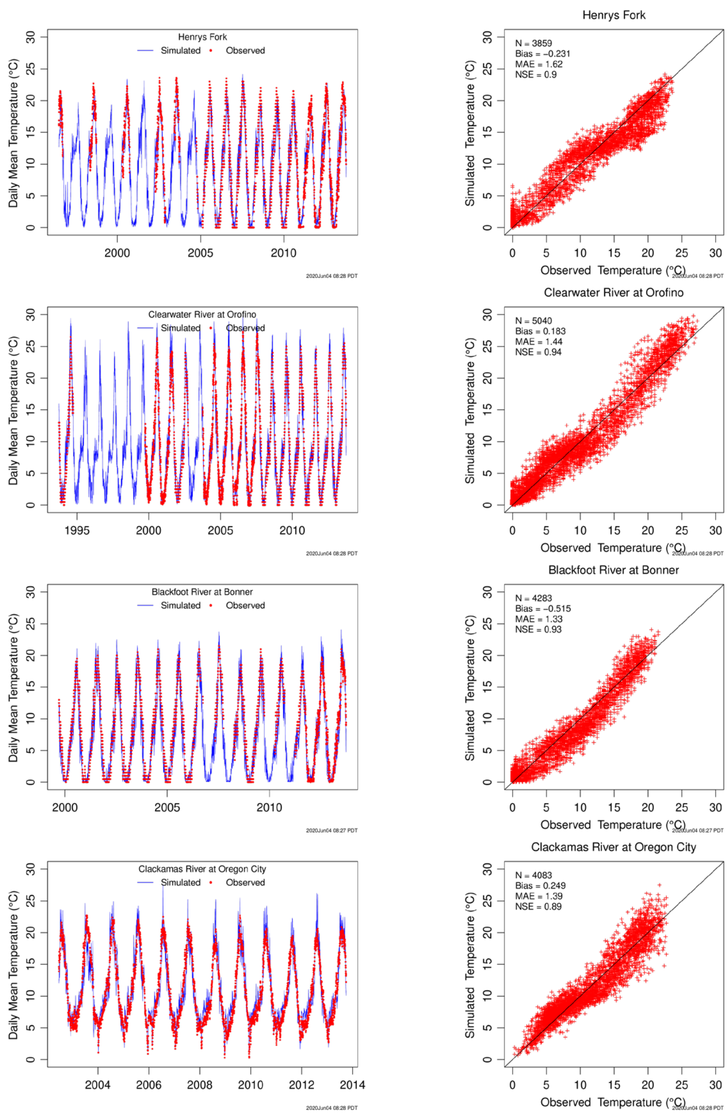

Figure 5.14. Comparison of simulated daily average stream temperature to observed in unregulated or lightly regulated streams. (N = number of observations, R^2 = linear correlation coefficient, RMS = root mean square error, MAE = mean absolute error, NSE = Nash-Sutcliffe model Efficiency coefficient)

5.2.2.2 Historical and Future Unregulated Flow

Once calibrated and validated, DHSVM/MASS1 was used to simulate Columbia River Basin streamflow and temperature for WY1983–2013. This simulation had no representation of regulation, which is pervasive throughout the basin. Water temperature was simulated for the same future climate scenarios as those described above for streamflow. Figure 5.17 compares historical and future day of year median water temperature in several Columbia Basin tributaries. Figure 5.18 compares the same at locations along the major tributaries and mainstem of the Columbia River. Figure 5.19 shows the historical to future change in mean August water temperature for DHSVM/MASS1 output locations. Water temperature is generally increased under the future climate throughout the year at most locations. The greatest increase at most, but not all, stations occurs in August and typically ranges between 1 and 3^{o}C depending on location. Increases of up to 4 degrees occur at a limited number of locations.

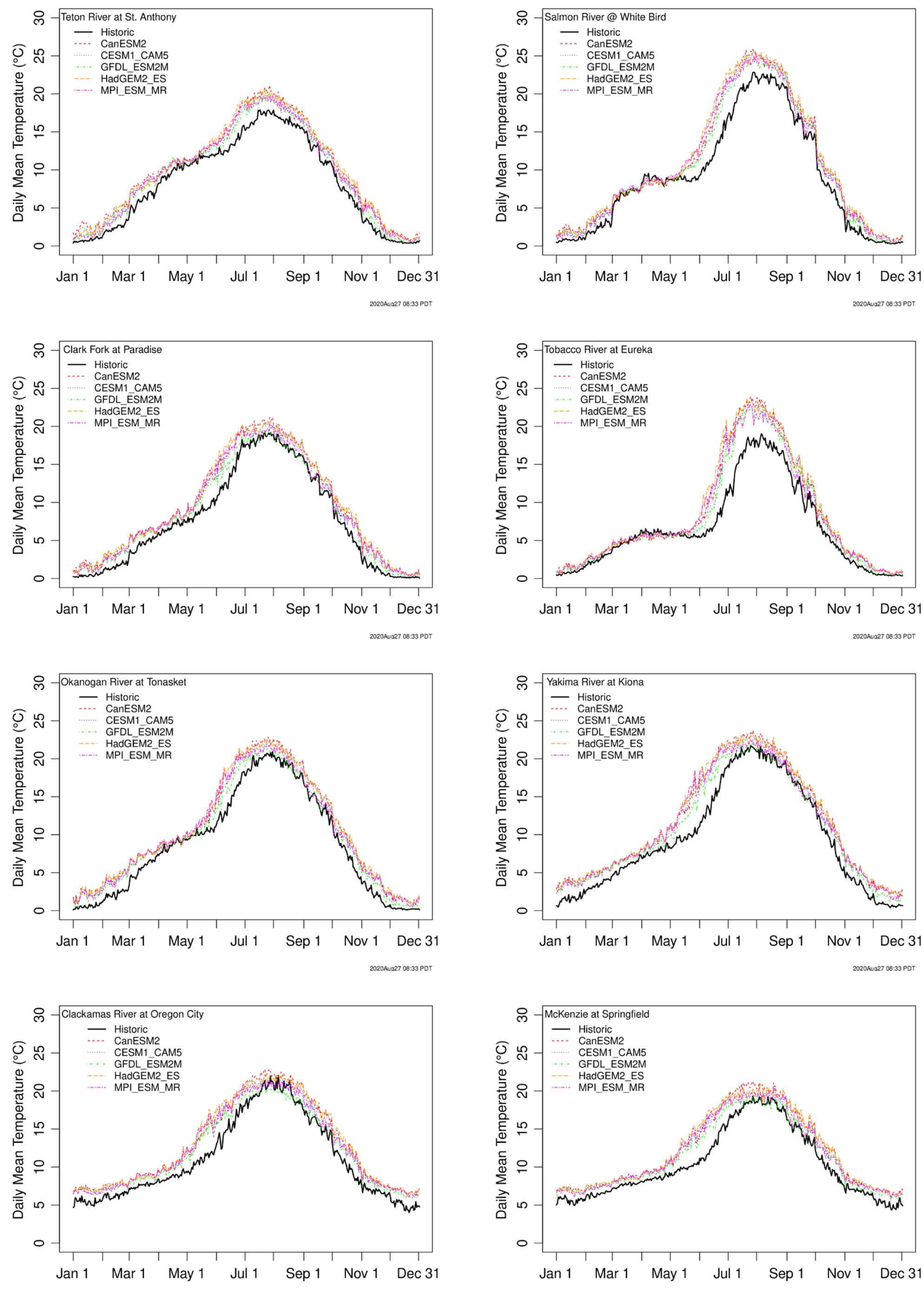

Figure 5.15. Median of simulated daily average temperature for each day of the year from historical and future scenarios in several smaller tributaries in the Columbia Basin.

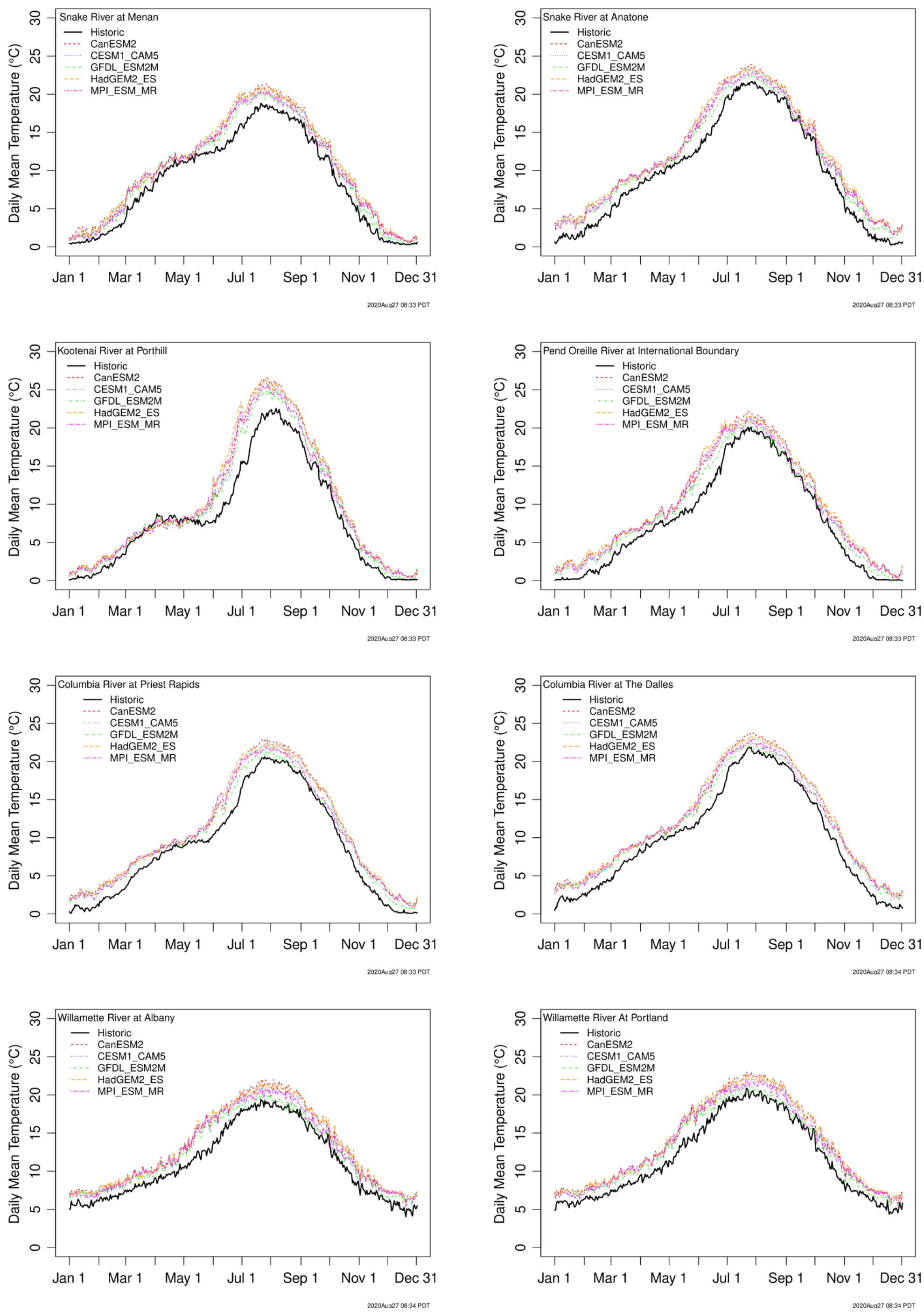

Figure 5.16. Median of simulated daily average temperature for each day of the year from historical and future scenarios at several locations on the Columbia River main stem and major tributaries.

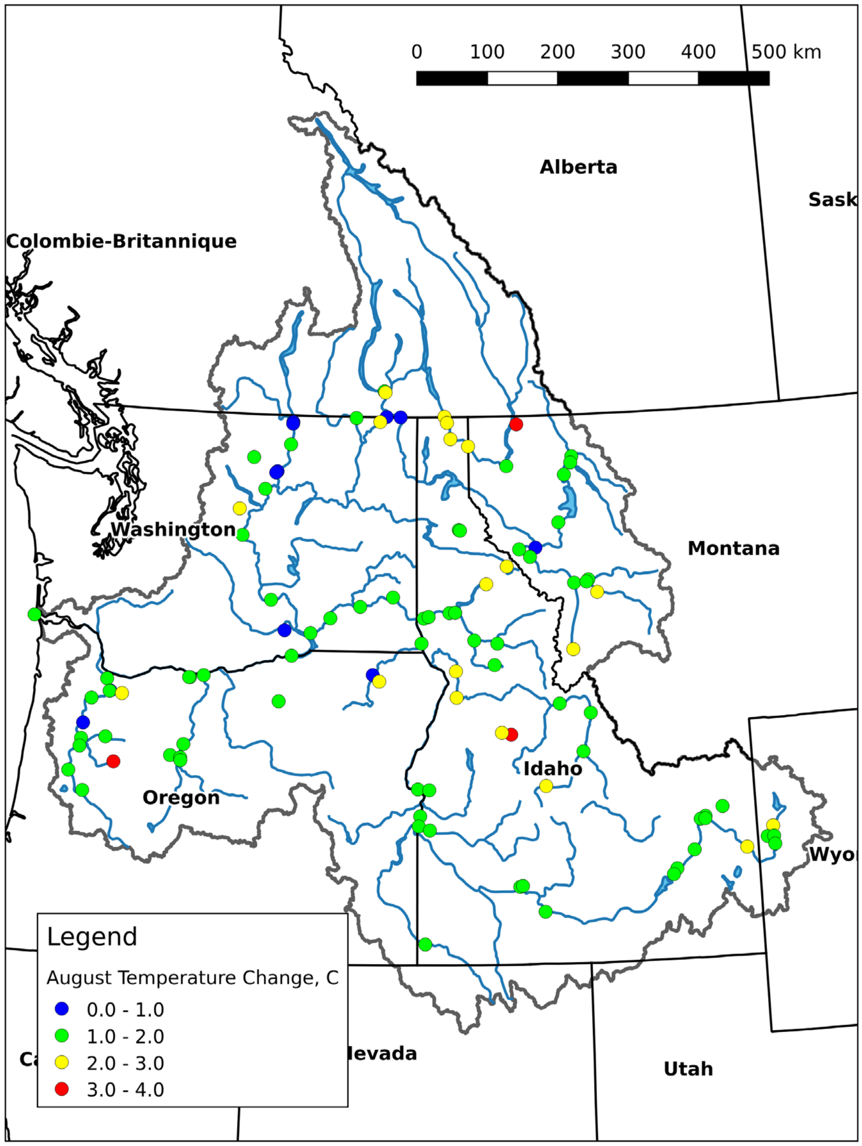

Figure 5.17. Historical to future change in median August water temperature at the DHSVM/MASS1 output locations. The change was computed by averaging the August temperatures from all future scenarios. Each location is colored by the difference between the average and historical.

5.3 Discussion

Generally, the Columbia River Basin responds to the projected future climate scenarios with earlier snowmelt and higher winter/early spring flow between January and April in most mainstem locations, including The Dalles. Flow is generally reduced during the summer, particularly in June and July. Higher January through April flows would generate more hydropower and produce more spill at most dams. Hydropower production would decline at the same time increased temperatures drive greater summer power use.

A shift in the timing of the peak inflow was also observed in some but not all subbasins. When present, that shift showed peak inflow occurring about one month earlier than historical timing.

The increase in cool-season system inflow to reservoirs will likely lead to an increase in typical cool-season water storage at the beginning of April. However, reduced inflow during the warm season may lead to a greater reliance on stored water resulting in a decline in end-of-month water storage volumes by the end of the summer.

Flood risk management procedures will need to anticipate increased cool season runoff with an earlier peak in some locations. Earlier releases of water from reservoirs at the flood risk management projects may be needed to capture the early runoff. Impacts to the timing of federal hydro system operations could also impact other spring and summer objectives such as flows for fish.

Unregulated water temperature in the Columbia River Basin is generally increased under the future climate conditions throughout the year at most locations. The greatest increase at most, but not all, stations occurs in August and typically ranges between 1 and 3ºC depending on location. Increases up to 4 degrees occur at a limited number of locations. Ecological impacts from projected future increases in temperature could have profound effects on aquatic species and physiology.

6.0 Connecticut River Unregulated Flow Application

The Connecticut River Basin, located in the northeastern United States, has a drainage area of 11,100 square miles (28,748 sq km) that flows across Connecticut, Massachusetts, New Hampshire, and Vermont (Figure 6.1, left). It contains 14 HUC 8 level subbasins that range from 1,990 sq mi to 391 sq mi. The river has more than 1,000 dams on its tributaries and 16 dams spanning its main stem, 12 of which are hydropower projects (CRC 2020).

6.1 Methods

6.1.1 Climate Simulations

As with the Columbia River Basin, we use the Livneh et al. (2015) daily gridded meteorological data set to represent historical conditions (Figure 6.1, right).

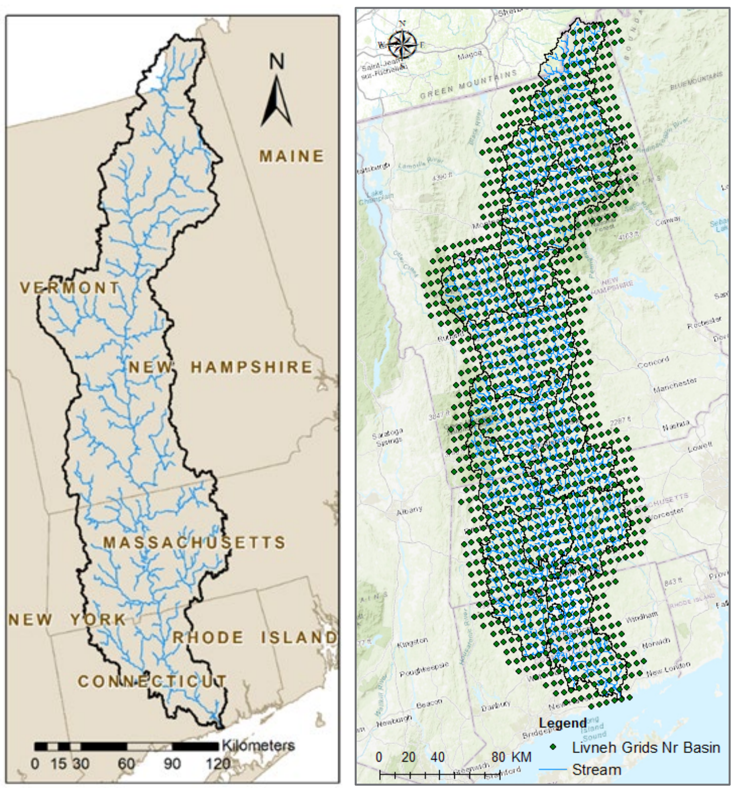

Figure 6.1. Connecticut River Basin (left); Livneh 2015 meteorology forcing grids in vicinity of the model domain.

For future climate in the Connecticut Basin we used the MACA statistically downscaled products from the Climatology Lab at the University of Idaho (Abatzoglou and Brown 2012). MACA is a multi-step procedure that uses bias-correction procedures and a constructed analogs approach for developing the fine-scale spatial pattern using a library of observed patterns. MACA is similar in construction to other constructed analogs but uses an observational data set to remove historical bias and fit appropriate spatial patterns in the output. Based on the 6 km meteorological data of Livneh (2013), the Climatology Lab downscaled and archived 20 CMIP5 GCMs under RCP4.5 and RCP8.5 for the conterminous United States (CONUS) and the Canadian portion of the Columbia River Basin for the period of 2006–2099. They also provided the GCM downscaled data for the historical period 1950–2005. The MACAv2-LIVNEH data set includes downscaled data for maximum temperature, minimum temperature, maximum and minimum relative humidity, precipitation accumulation, downward surface shortwave radiation, wind velocity, and specific humidity. In this project, we selected the following five GCMs that were shown to represent divergence for future changes in temperature and precipitation for the RCP8.5 emission scenario for the CONUS (Naz et al. 2016):

- the second-generation Canadian Earth System Model (*CanESM2*),
- the fourth version of the Community Climate System Model (CCSM4),
- the Geophysical Fluid Dynamics Laboratory Earth System Model Version 2M (GFDL_ESM2M),
- the Hadley Global Environment Model 2-Earth System (HadGEM2_ES), and
- the Meteorological Research Institute Coupled Global Climate Model Version Three (MRI-CGCM3).

The downscaled projections of the climate of the 2040–2070 period show generally higher precipitation across the basin, while air temperature increases by 2–5°C depending on location and GCMs.

6.1.2 Watershed Modeling

The Connecticut River Basin was modeled at a 3 hour time step and a 90 m resolution following the Columbia River Basin modeling practices. This yielded a domain size of 1,432 columns and 5,131 rows, and 3.59 million active grid cells (~4% the size of the Columbia River Basin).

The spatial model input for DHSVM is shown in Figure 6.2. The DEM data were resampled from the 30 m National Elevation Dataset (USGS 2017). Soil types were generated using the Soil Survey Geographic Database (SSURGO; NRCS 2019a). Vegetation land cover was derived from the National Land Cover Data set (USGS2014). The stream network was generated using the Python-based DHSVM preprocessing module, which calculates and extracts accumulated flow lines based on flow direction as derived from the DEM.

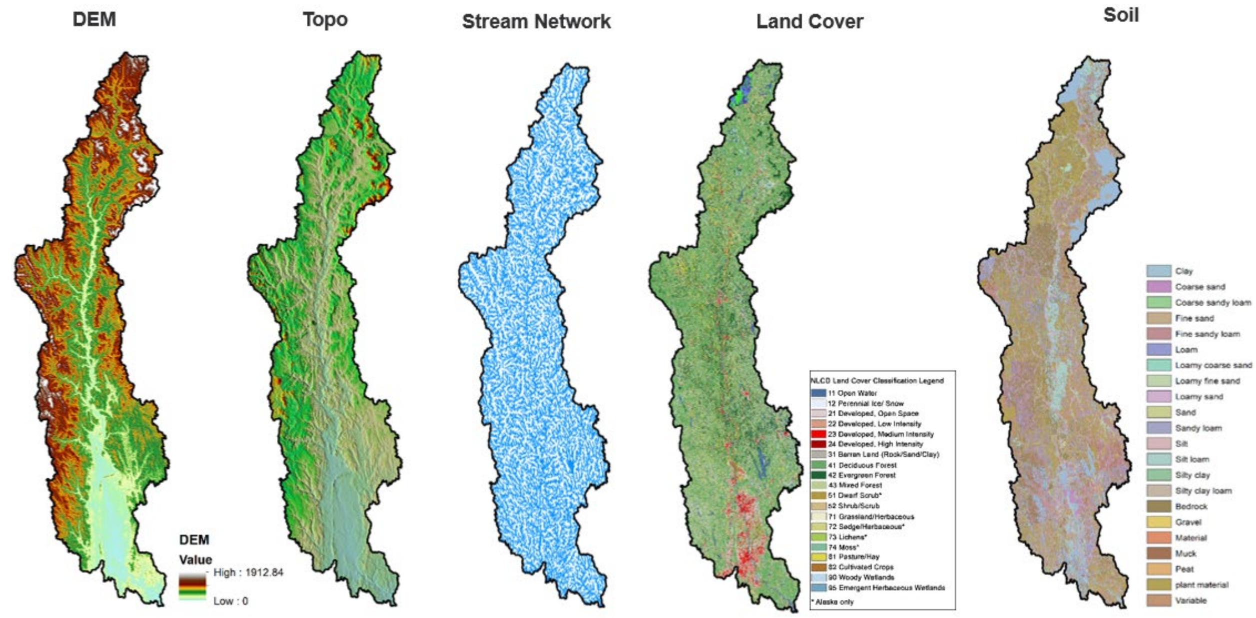

Figure 6.2. Spatial model input of Connecticut River Basin.

6.2 Results

6.2.1 Streamflow

6.2.1.1 Model Calibration and Validation

The Connecticut River Basin is a heavily regulated river basin, therefore the selected USGS gages for calibration are mostly located near headwater locations to minimize the impacts of hydrologic regulations/operations (Figure 6.3 and Table 6.1). Previous DHSVM model applications in the same domain were also used to reference the selection of such locations.

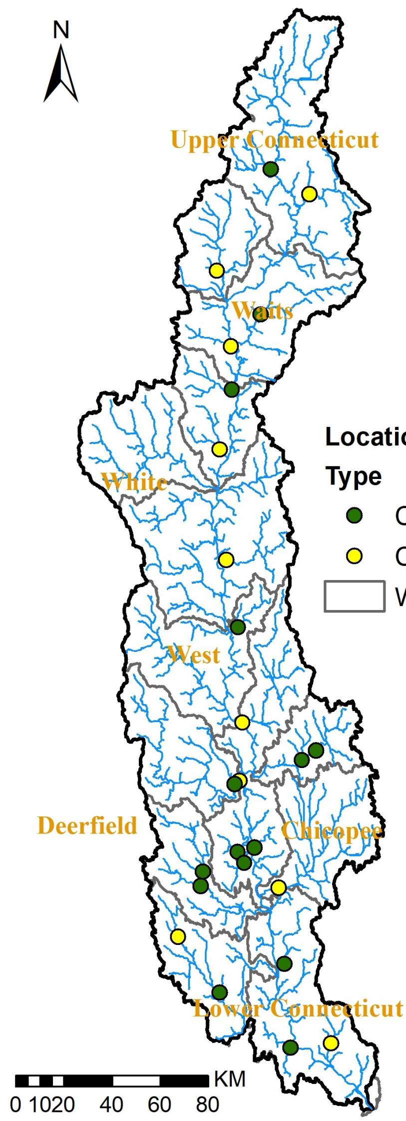

Figure 6.3. Subbasins of Connecticut River Basin showing USGS gauges used for DHSVM streamflow calibration/validation (yellow) and additional validation by the Connecticut River UnImpacted Streamflow Estimator (CRUISE).

Table 6.1. Summary of selected USGS stations for calibration.

Station	Basin	River	Town, State	Latitude	Longitude
1130000	Upper Conn	Upper Ammonoosuc River	Groveton, NH	44.625	-71.4694
1135300	Passumpsic	Sleepers River	St. Johnsbury, VT	44.43528	-72.0389

Station	Basin	River	Town, State	Latitude	Longitude
1139000	Waits	Wells River	Wells River, VT	44.15028	-72.0656
1141500	Mascoma	Ompompanoosuc River	UNION VILLAGE, VT	43.79	-72.2553
1152500	Black/Ottau	Sugar River	West Claremont, NH	43.38746	-72.3635
1169000	Deerfield	North River	Montague City, MA	42.58022	-72.5745
1177000	Chicopee	Chicopee River	INDIAN ORCHARD, MA	42.16056	-72.5144
1161000	Middle Conn	Ashuelot River	Hinsdale, NH	42.78583	-72.4867
1185500	Farmington	West Branch Farmington	New Boston, MA	42.07433	-73.0666
1193500	Lower Conn	Salmon River	East Hampton, CT	41.55222	-72.4497

The model was driven with Livneh meteorological data for 5 years in each subbasin for calibration and 10 years for validation at 3 hour time steps. The time period for calibration and validation varies slightly based on available records for each station (Table 6.2). To represent the characteristics of each subbasin while enabling a basin-wide model run, the model was calibrated at the subbasin scale with a combination of fixed (base) basin-wide parameters and parameters calibrated to each subbasin. The base parameters were kept consistent among the subbasins while the calibration parameters differ by basin to represent spatial heterogeneity. Examples of calibration parameters are temperature lapse, snow/rain threshold, soil lateral conductivity, overstory fractional cover, and leaf area index. While having the same base parameters allows for basin-wide modeling, it also placed limitations on the performance of the model in each subbasin to some extent. The model generally performed well; the NSEs for the calibration and validation for each subbasins are listed in Table 6.2 and their hydrographs are shown in Figure 6.4.

Table 6.2. Summary of hydrological statistics of model calibration and validation.

		Calibration			Validation		
Station	Basin	Period (5 yr)	NSE	MAE (cms)	Period (10 yr)	NSE	MAE (cms)
1130000	Upper Conn	1998-2002	0.74	5.11	1994-2003	0.72	5.08
1135300	Passumpsic	1998-2002	0.71	0.78	1993-2002	0.70	0.82
1139000	Waits	1998-2002	0.66	1.52	1998-2008	0.66	1.70
1141500	Mascoma	1985-1989	0.66	1.93	1980-1990	0.51	2.34
1152500	Black/Ottau	1998-2002	0.72	3.86	1998-2008	0.74	4.68
1169000	Deerfield	1981-1985	0.68	2.33	1981-1990	0.67	2.36
1177000	Chicopee	1998-2002	0.73	5.85	1998-2007	0.66	7.69
1161000	Middle Conn	1985-1989	0.70	6.75	1984-1994	0.72	6.85
1185500	Farmington	1981-1985	0.71	2.57	1981-1990	0.70	2.57
1193500	Lower Conn	1981-1985	0.72	2.26	1981-1990	0.72	2.06

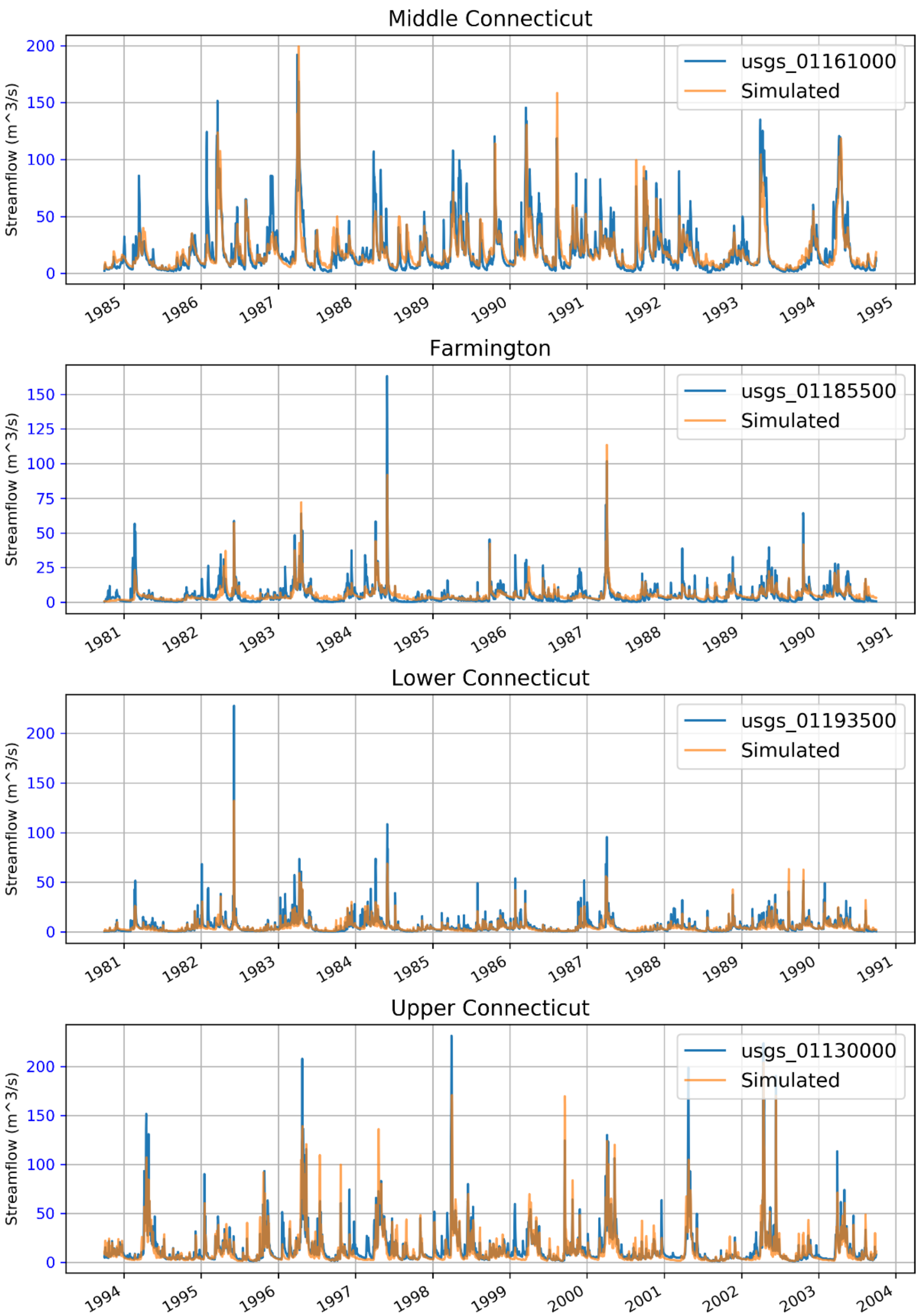
Middle Connecticut
usgs_01161000
Simulated
Streamflow (m^3/s)
0
50
100
150
200
1985
1986
1987
1988
1989
1990
1991
1992
1993
1994
1995
Farmington
usgs_01185500
Simulated
Streamflow (m^3/s)
0
25
50
75
100
125
150
1981
1982
1983
1984
1985
1986
1987
1988
1989
1990
1991
Lower Connecticut
usgs_01193500
Simulated
Streamflow (m^3/s)
0
50
100
150
200
1981
1982
1983
1984
1985
1986
1987
1988
1989
1990
1991
Upper Connecticut
usgs_01130000
Simulated
Streamflow (m^3/s)
0
50
100
150
200
1994
1995
1996
1997
1998
1999
2000
2001
2002
2003
2004

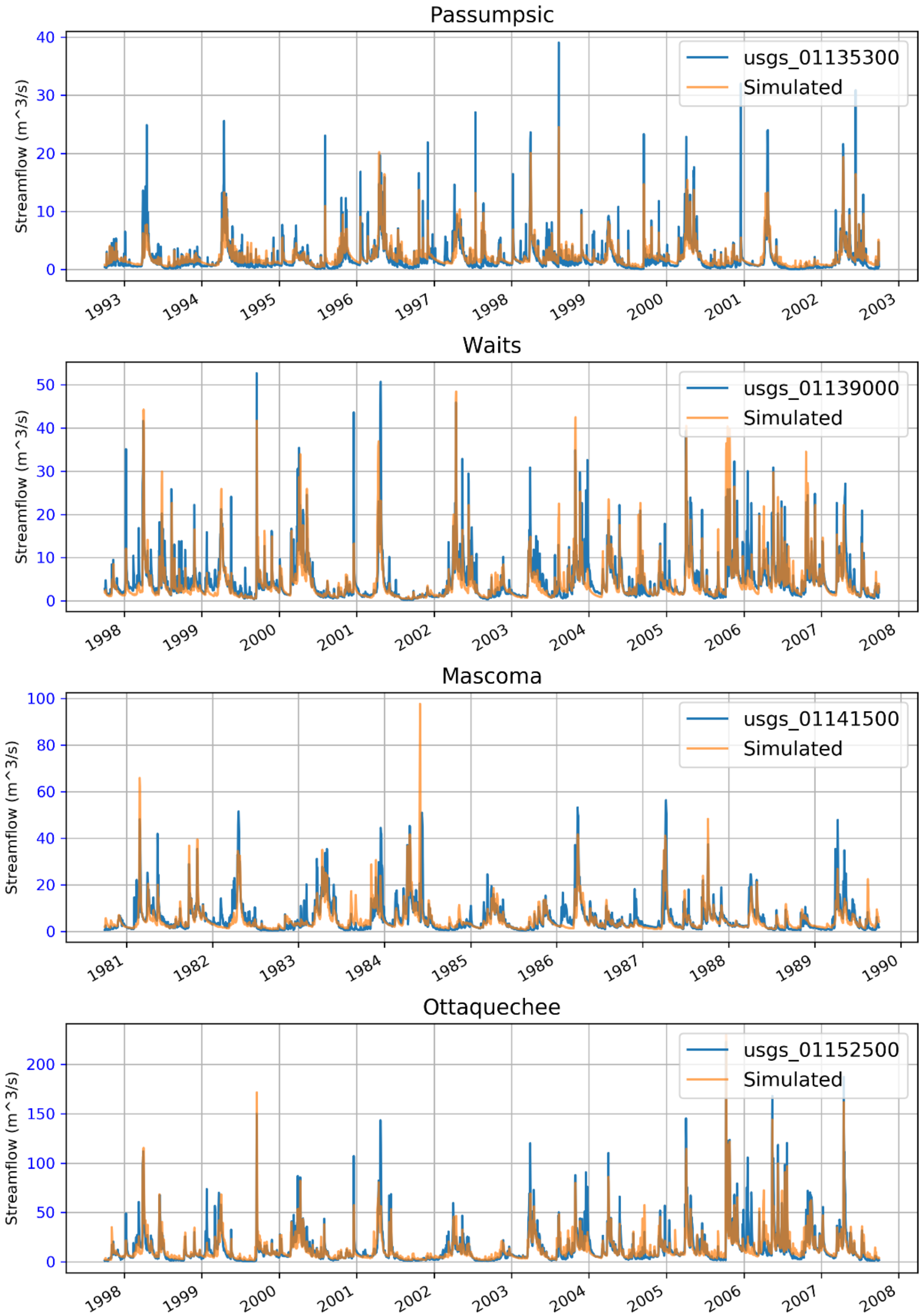
Passumpsic
usgs_01135300
Simulated
Streamflow (m^3/s)
Waits
usgs_01139000
Simulated
Streamflow (m^3/s)
Mascoma
usgs_01141500
Simulated
Streamflow (m^3/s)
Ottaquechee
usgs_01152500
Simulated
Streamflow (m^3/s)

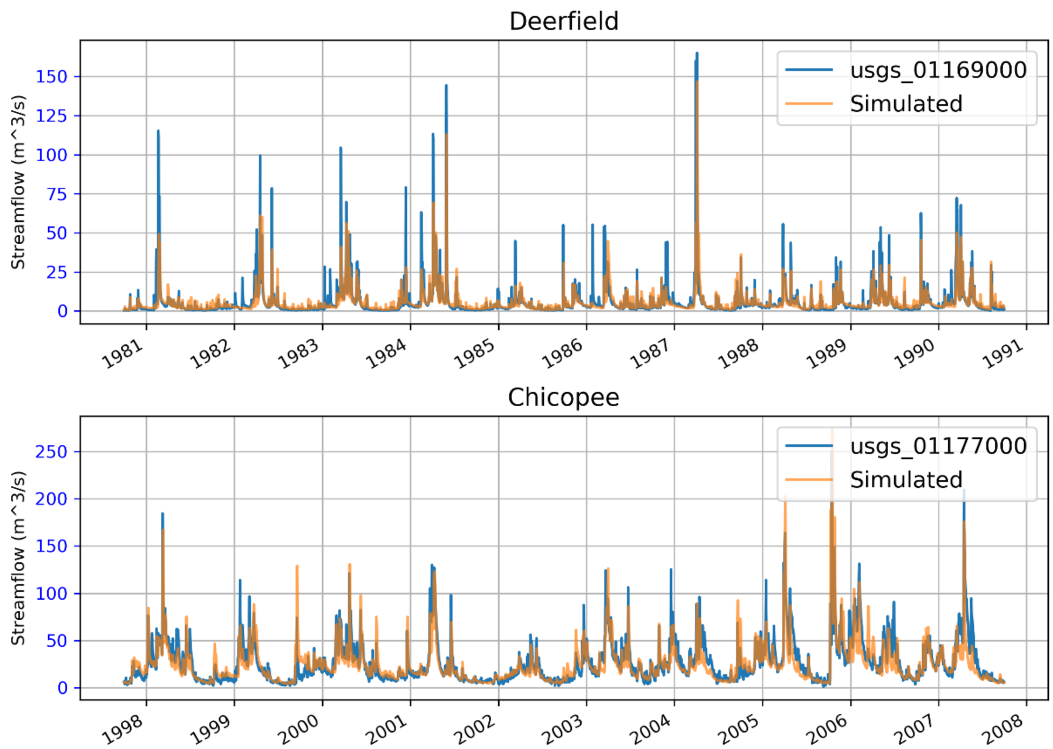

Figure 6.4. Connecticut River Basin model calibration and validation at subbasins.

The area of calibrated subbasins is limited to a portion of the basin. Therefore, to further validate our parameter sets, we used the Connecticut River UnImpacted Streamflow Estimator (CRUISE) tool and expanded the domain of model validation at additional ungaged locations in the basin, as shown in Figure 6.3 and Listed in Table 6.3.

The CRUISE tool was developed by the USGS (Archfield et al. 2009, 2013) to estimate impaired flow duration curves and simulate daily incremental unregulated hydrographs at ungaged locations in the Connecticut River Basin. Given that the estimated hydrograph using CRUISE is derived data based on adjacent USGS stations and empirical equations instead of observation, we evaluate simulated flow against the CRUISE flow at a monthly resolution. The model generally performed well as demonstrated by the validation hydrograph and their statistics shown in Figure 6.5

Table 6.3. Additional locations for model validation in the Connecticut River Basin (lat/lon indicates approximate watershed outlet location).

RefID	Basin	Lat	Long	Drainage Area (sq km)
1282	Upper Connecticut	44.75112	-71.6326	376
2416	Upper Connecticut	44.59599	44.49043	350
3884	Waits	44.23797	-71.8758	635
4843	Upper Connecticut -Mascoma	43.99498	-72.1173	404
01155000	West	43.13214	-72.3898	216
11888	Millers	42.59691	-72.2397	190

RefID	Basin	Lat	Long	Drainage Area (sq km)
01164000	Millers	42.61792	-72.1579	492
12490	Deerfield	42.57203	-72.6026	232
01181000	Westfield	42.23713	-72.8958	243
01179500	Westfield	42.28587	-72.8668	420
01171500	Middle Connecticut	42.32646	-72.6719	133
13999	Middle Connecticut	42.32676	-72.5835	142
14429	Middle Connecticut	42.27969	-72.6531	182
16688	Farmington	41.83592	-72.9304	798
16317	Lower Connecticut	41.881	-72.5803	262
17501	Lower Connecticut	41.57309	-72.6525	282

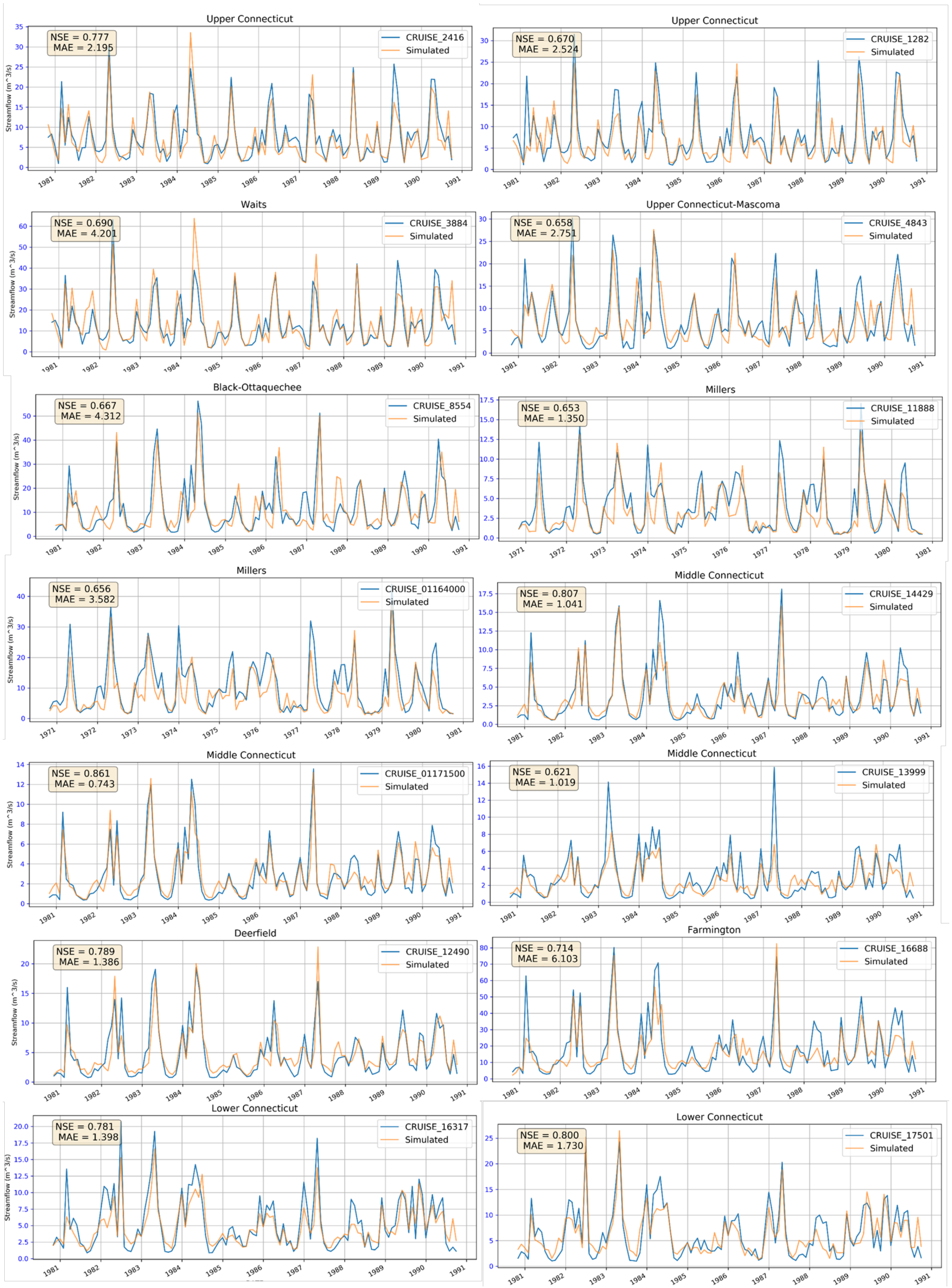

Figure 6.5. The Connecticut River Basin subbasin hydrographs compared with simulated hydrographs using the CRUISE tool at monthly resolution.

6.2.1.2 Historical and Future Unregulated Flow

The calibrated and validated model was first driven with historical climate data simulated from the CanESM2, CCSM4, and FDL_ESM2M GCMs to check for consistency with the historical Livneh data. The historical GCM driven simulations show slight differences, but generally similar flow patterns to those driven by the historical Livneh data (Figure 6.6).

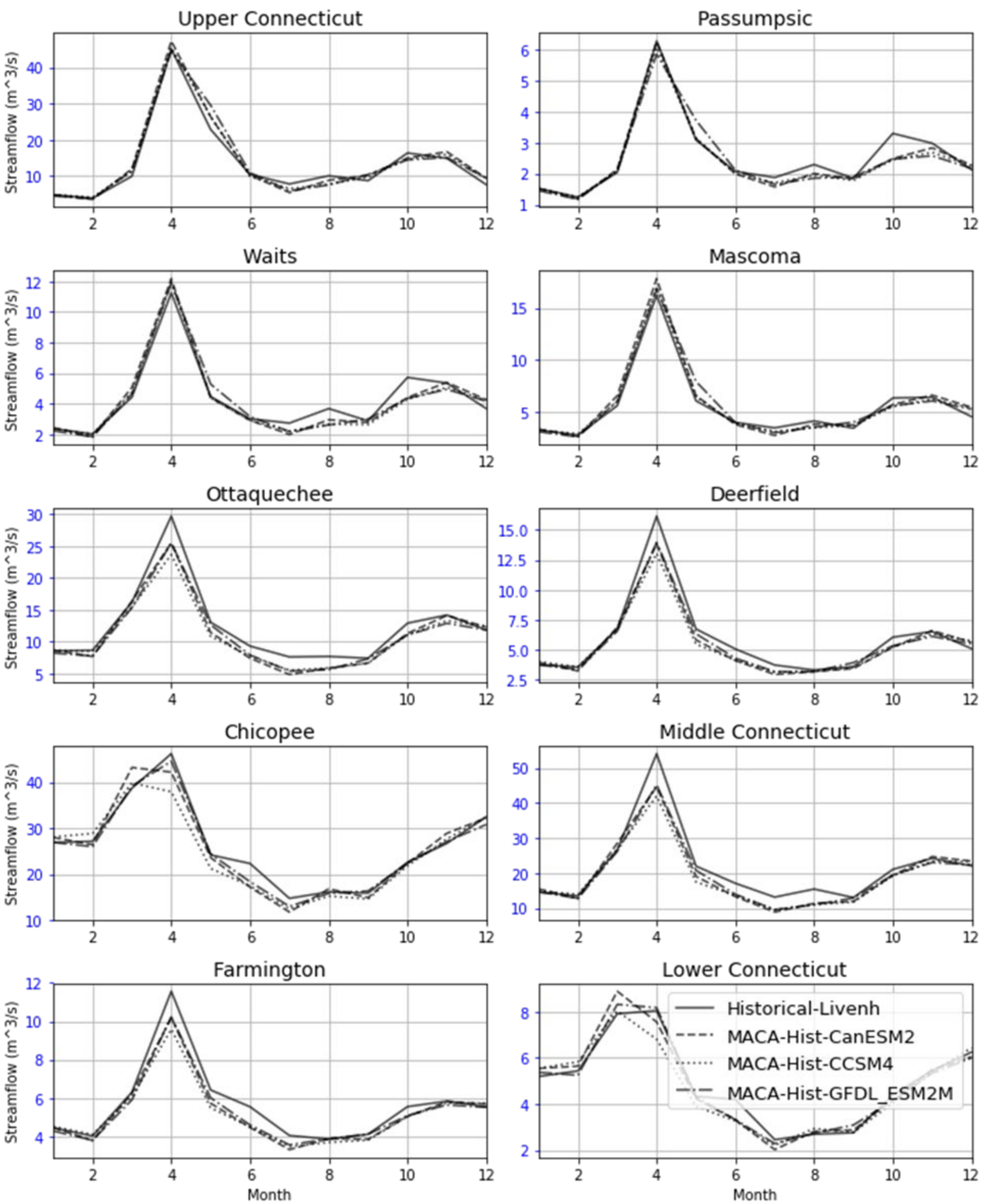

Figure 6.6. Simulated monthly flow of historical Livneh and historical MACA-Livneh GCMs.

Future climate data from all five GCMs were then applied to the integrated DHSVM/MASS1 model. The resulting winter flows in the Connecticut Basin are generally increased under future climate conditions, while the flow is reduced in the spring (Figure 6.7). At many locations, the seasonal peak flow is earlier and reduced in the future. Some spatial patterns are also present. The Upper Connecticut subbasin has similar peak flow magnitudes under future climate and the historical climate, while the timing of the flow has shifted with increases in the flow from November to March and decreased flow observed in May, September, and October; Similar timing shifts can be found in the Passumpsic, Waits, and Mascoma subbasin, while they also witnessed slight decrease in peak flow with future climate. For the middle and lower part of the watershed (Ottaquechee, Deerfield, Chicopee, Middle Connecticut, and Farmington), the peak flow has shifted to an earlier date, companied with higher winter flows and lower summer flows among most of the future climate GCMs. The Lower Connecticut subbasin has the earliest peak flow among all subbasins under historical climate, and it will also experience an increase in flow during the fall and a decrease in the summer.

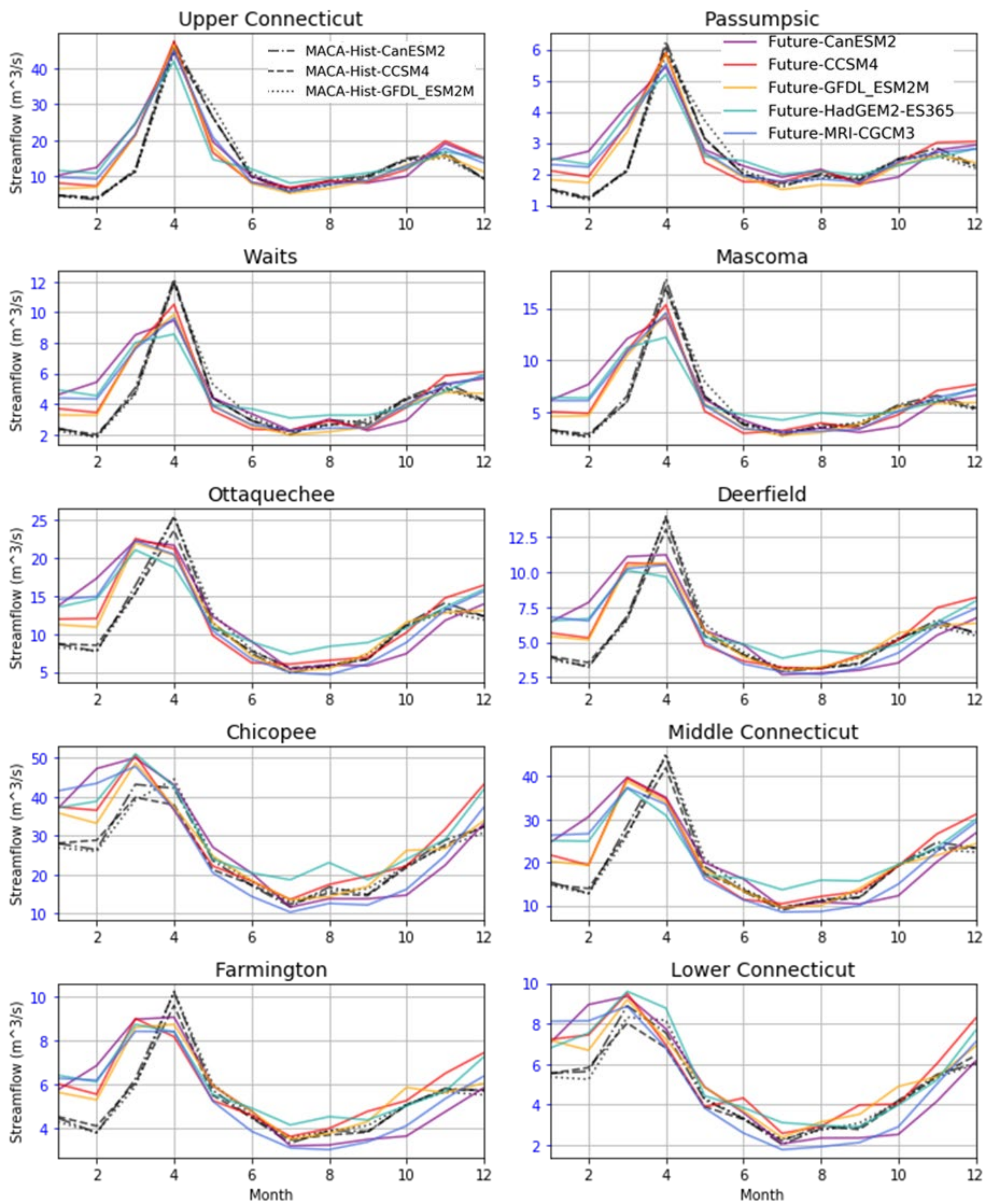

Figure 6.7. Monthly averaged streamflow (in cubic meters per second) for historical and five future GCMs.

6.2.2 Water Temperature

6.2.2.1 Model Calibration

After calibrating and validating the streamflow, DHSVM/MASS1 was calibrated for stream temperature. Meteorologic coefficients were tuned for each HUC8 subbasin (Figure 6.8). Observed data were obtained from the USGS and the Spatial Hydro-Ecological Decision System (SHEDS) for the stations shown in Figure 6.9. In general, few continuous temperature records were available, and these were mostly in the state of Connecticut. Consequently, a classic calibration and validation could not be performed. Calibration coefficients were tuned using the entire simulation record. In general, the lateral inflow temperature was kept at the computed annual average air temperature (Figure 6.8), but in a few subbasins it was adjusted. Calibrated meteorologic coefficients are shown in Table 6.4. Figure 6.10 compares daily average water temperature for a few selected locations. The model generally performs well as illustrated in Table 6.5 which lists calibration statistics for all gages used for calibration.

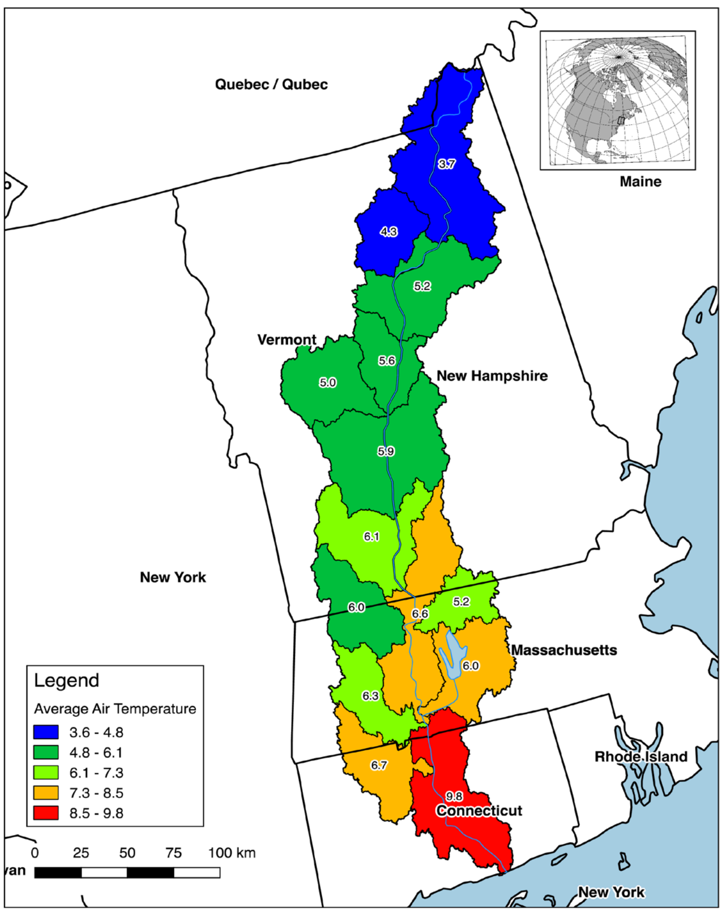

Figure 6.8. HUC 8 subbasin boundaries in the Connecticut River Basin and the average annual air temperature computed from Livneh meteorological forcing data within each HUC 8 boundary.

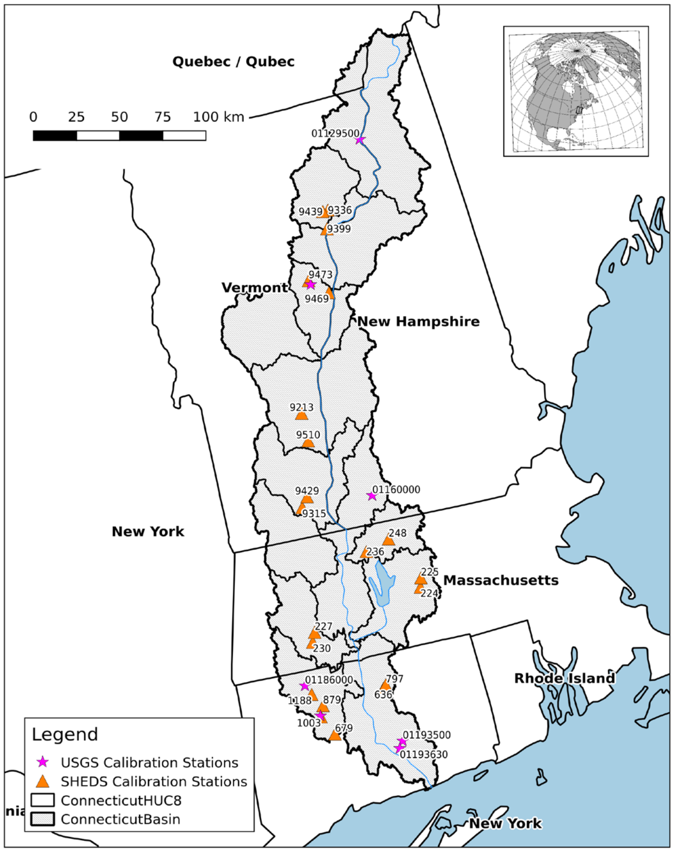

Figure 6.9. USGS and SHEDS stations used for Connecticut River Basin stream temperature calibration.

Table 6.4. Calibrated water temperature coefficients for the Connecticut River Basin. HUC 8 boundaries are shown in Figure 6.9. a_W, b_W, and C_c are wind function coefficients and the conduction coefficient, respectively. T_I is inflow temperature.

HUC8	a_W	b_W	C_c	T_I, °C
01080101	0.35	6.9	0.47	3.7
01080102	0.06	1.2	0.47	4.3
01080103	0.46	9.2	0.47	5.2
01080104	0.46	9.2	0.47	5.6
01080105	0.69	13.8	0.47	5.0
01080106	0.23	4.6	0.47	5.9
01080107	0.35	6.9	0.47	6.1
01080201	0.35	6.9	0.47	6.6
01080202	0.69	13.8	0.47	5.2
01080203	0.46	9.2	0.47	6.0
01080204	0.35	6.9	0.47	6.0
01080205	0.35	6.9	0.47	9.8

HUC8	a_W	b_W	C_c	T_l, °C
01080206	0.69	13.8	0.47	6.3
01080207	0.12	2.3	0.47	6.7

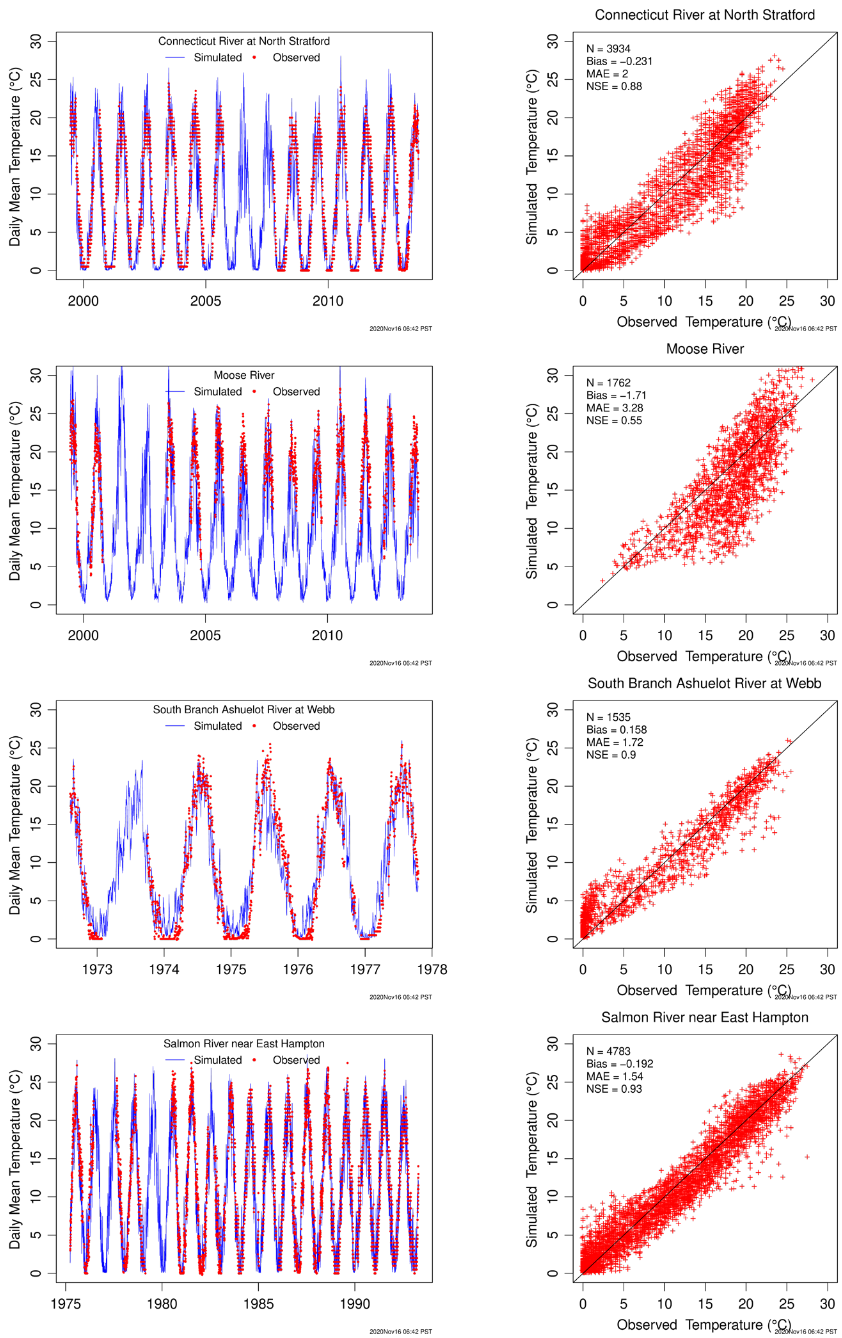

Figure 6.10. Comparison of simulated daily average stream temperature to observed at several locations along the heavily regulated Connecticut River Basin. (N = number of observations, R^2 = linear correlation coefficient, RMS = root mean square error, MAE = mean absolute error, NSC = Nash-Sutcliffe coefficient).

Table 6.5. Statistics from comparison of simulated and observed stream temperature in the Connecticut basin. (*N* = number of observations, R^2 = linear correlation coefficient, RMS = root mean square error, MAE = mean absolute error, NSE = Nash-Sutcliffe model Efficiency coefficient.

HUC8	Agency	ID	Description	*N*	Bias (ºC)	RMS (ºC)	AME (ºC)	NSE
01080101	USGS	01129500	Connecticut River at North Stratford	3934	-0.23	2.63	2.00	0.88
01080102	VTFWD	9439	Sleepers River	1589	0.30	3.59	2.90	0.60
	VTFWD	9336	Moose River	1762	-1.71	4.13	3.28	0.55
	VTFWD	9399	Passumpsic River	1448	-0.46	4.03	3.22	0.58
01080104	VTFWD	9473	Waits River at U36	259	-0.54	2.04	1.60	0.77
	VTFWD	9469	Waits River at RT25B	266	-0.80	1.91	1.56	0.83
	USGS	01139838	Pike Hill Brook at Pike Hill Rd	645	-0.28	3.19	2.69	0.69
01080106	VTFWD	9213	Black River	232	-0.32	2.36	1.83	0.85
	VTFWD	9510	Williams River	418	0.47	2.61	2.14	0.88
01080107	VTFWD	9429	Rock River at Duke Rd	1166	0.12	2.17	1.72	0.91
	VTFWD	9315	Marlboro Branch	237	0.15	2.42	1.91	0.67
01080201	USGS	01160000	South Branch Ashuelot River at Webb	1535	0.16	2.28	1.72	0.90
01080202	MAFW	236	Gulf Brook	815	1.20	4.09	2.86	0.74
	MAFW	248	Whetstone Brook	813	0.44	2.64	1.85	0.88
01080204	MAFW	224	Maynard Brook	782	-0.26	2.55	2.18	0.83
	MAFW	225	Parkers Brook	782	-0.70	1.99	1.52	0.91
01080205	USGS	01193630	Salmon River at Leesville	3625	0.20	2.32	1.7	0.91
	USGS	01193500	Salmon at East Hampton	4783	-0.19	1.98	1.54	0.93
	CTDEEP	636	Hockanum River at Dart Hill	1708	-0.70	2.47	2.05	0.9
	CTDEEP	797	Hockanum River at West Street	1368	0.20	2.89	2.36	0.86
01080206	MAFW	227	Roaring Brook	990	1.78	4.16	2.57	0.77
	MAFW	230	Stage Brook	991	2.35	5.36	3.25	0.70
01080207	CTDEEP	679	Pequabuck River	2705	-0.16	3.65	2.90	0.78
	CTDEEP	879	Cherry Brook at RT44	1110	-0.81	3.27	2.65	0.67

6.2.2.2 Historical and Future Stream Temperature

Connecticut Basin water temperature was also simulated for the historical and future scenarios described above. Figure 6.11 compares the median water temperature for each day of the year simulated in the **unregulated** historical and future scenarios. Figure 6.12 depicts the change in August mean water temperature from historical to future scenarios. Unregulated water temperature is increased under the future climate throughout the year at most locations. The greatest increase at most, but not all, stations occurs in August and typically ranges between 3 and 5ºC depending on location. Increases up to 6 degrees occur at a limited number of locations.

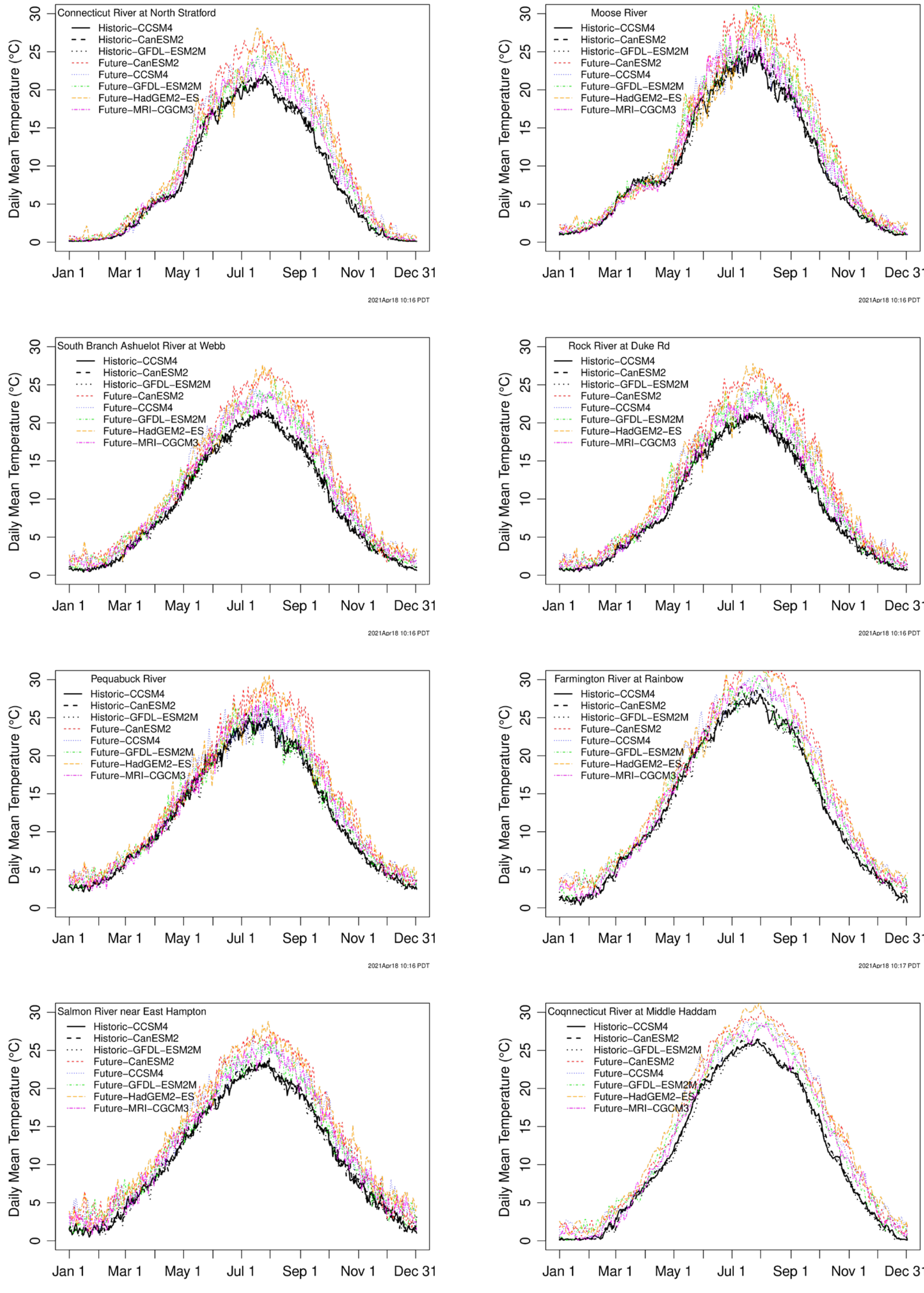

Figure 6.11. Comparison of median water temperature by day of year simulated in the historical and future climate scenarios for some locations in the Connecticut River Basin.

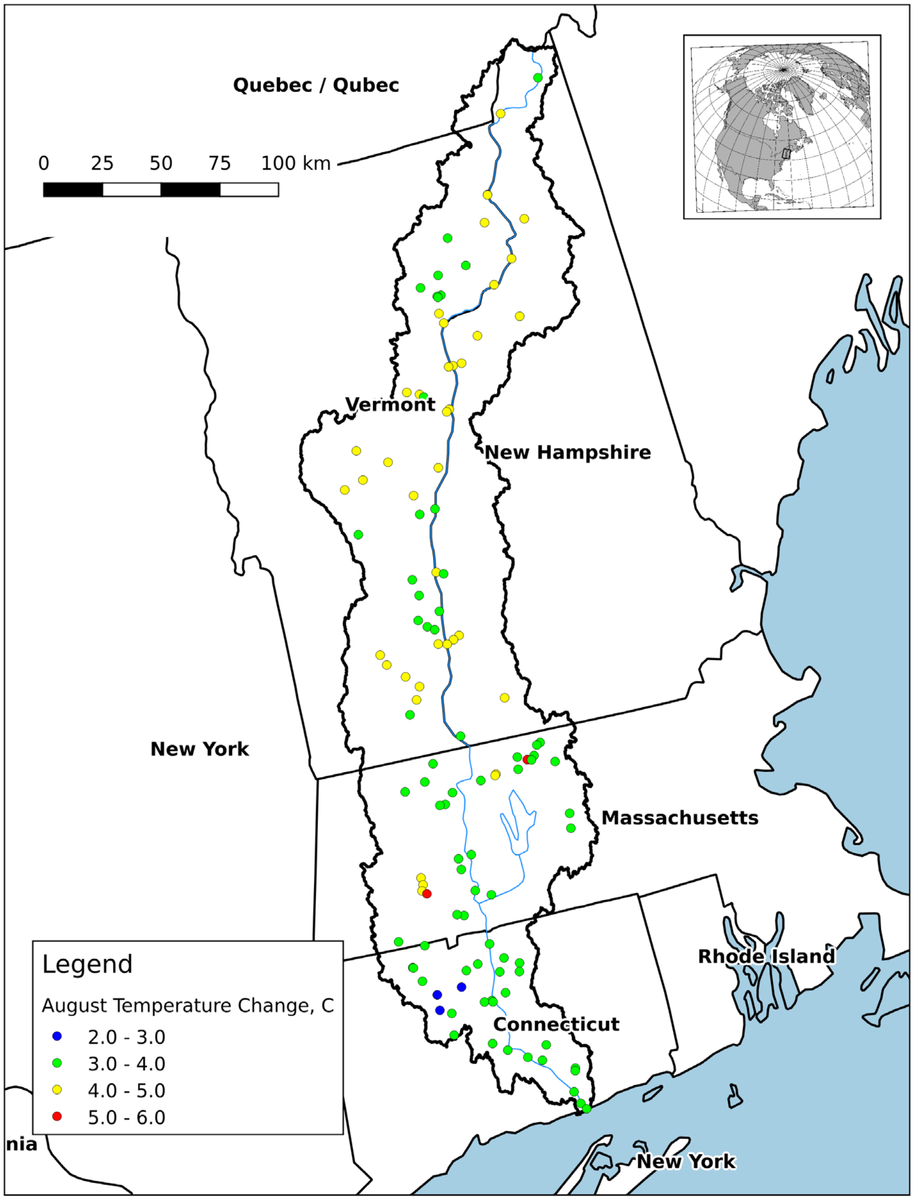

Figure 6.12. Historical to future change in median August water temperature at the DHSVM/MASS1 output locations. The change was computed by averaging the August temperatures from all historical and future changes. Each location is colored by the difference between averages.

6.3 Discussion

Unregulated winter flows in the Connecticut Basin are generally increased under future climate conditions, while the flow is reduced in the spring. At many locations, the seasonal peak flow is earlier and reduced in the future. The Upper Connecticut subbasin has similar peak flow magnitudes under future climate and the historical climate, while the timing of the flow has shifted with increases in the flow from November to March and decreased flow observed in May, September, and October. For the middle and lower portion of the watershed, the peak flow has shifted to an earlier date, accompanied by higher winter flows and lower summer flows among most of the future climate GCMs. The Lower Connecticut subbasin has the earliest peak flow among all subbasins under historical climate, and it will also experience an increase in flow during the fall and a decrease in the summer under future climate conditions.

Unregulated water temperature is increased under the future climate throughout the year at most locations. The greatest increase at most, but not all, stations occurs in August and typically ranges between 3 and 5°C depending on location. Increases up to 6 degrees occur at a limited number of locations.

7.0 Summary

7.1 Summary of Results

The goal of this research is to test a new modeling framework for examining the impacts of climate change on streamflow and water temperature at large basin scales. This goal was achieved by enhancing key existing fine resolution hydrology and stream temperature models and transferring them to a high-performance computing environment to provide a high-spatiotemporal resolution, multi-scale modeling framework. Consistent with the study objectives, the main conclusions of the project are provided in Table 7.1.

Table 7.1. Research Objectives and Results.

Objective	Results
1) Impacts of Atmospheric Rivers	We found that the monthly extreme precipitation amount in West Coast watersheds is closely related to AR intensity with the strongest relationship in the Pacific Northwest and California. ARs can be classified into three categories: weak ARs, flash ARs, and prolonged ARs. Flash ARs and prolonged ARs, though accounting for less than 50% of total AR events, are more important in controlling extreme precipitation patterns and should be prioritized for future studies of hydrological extreme events. ARs can significantly modulate surface hydrological processes through the extreme precipitation they produce. ARs produce heavy precipitation but suppress evapotranspiration. Snowpack ablates more during ARs, and higher air temperature and increased longwave radiation play the primary and secondary roles, respectively. When the local air temperature is in the 0°C to 10°C range, ARs increase the probability of snow ablation from 0.33 to 0.57. The runoff-to-precipitation ratio during AR events is primarily controlled by antecedent soil moisture, but it almost doubles in the northwestern watersheds because of the intensification of snow ablation during AR events. Precipitation, temperature, and radiation are identified as the key drivers that distinguish the hydrologic responses between AR and non-AR events. Lastly, analysis of ARs and total runoff at an annual scale and 1 April snowpack and winter precipitation shows that ARs explain 30% to 60% of the variability of annual total runoff and sharpen the seasonality of water resources availability in the West Coast mountain watersheds
2) DHSVM parallelization	The DHSVM code was successfully parallelized for distributed memory computers using the Global Arrays (GA) programming model. Parallel code speedup was significant at 90 m resolution in the Clearwater (a watershed within the Columbia River Basin; 25,000 km^2) and the full Columbia (668,000 km^2)

	River basins. Run times for 1-year simulations were reduced by an order of magnitude for both test basins. A maximum parallel speedup of 105 times was attained with 480 processors while simulating the Columbia River Basin. Simulation run times were reduced enough to make long-term (decades), ultra-fine (90 m) spatial resolution simulations of significantly sized basins such as the Columbia manageable. This allows the modeling framework to represent critical small-scale biophysical processes that show significant spatial variation with local meteorology, vegetation, soils, and topography (elevation, slope, aspect, etc.).
3) DHSVN/MASS1 integration	MASS1 was added to DHSVM, bringing full hydrodynamic routing and stream temperature simulation to the integrated model. This represents a significant advancement by allowing distributed inflows from the watershed to the channel network and an explicit representation of the impacts of riparian vegetation on stream temperature. This provides a seamless capability for analysis over a range of spatial scales.
4) Framework Application to the Columbia River Basin	In simulations of unregulated flows, the Columbia River Basin generally responds to the projected future climate scenarios with earlier snowmelt and higher winter/early spring flow between January and April in most mainstem locations, including The Dalles. Flow is generally reduced during the summer, particularly in June and July. A shift in the timing of the peak inflow was also observed in some but not all subbasins. When present, that shift showed peak inflow occurring about one month earlier than historical timing. Water temperature in the Columbia River Basin is generally increased under the future climate conditions throughout the year at most locations during simulations of unregulated flows. The greatest increase at most, but not all, stations occurs in August and typically ranges between 1 and 3°C depending on location. Increases up to 4 degrees occur at a limited number of locations. Ecological changes will vary based on the projected rate of temperature increase as well as site-specific increases in temperature.
5) Framework Application to the Connecticut River Basin	Unregulated winter flows in the Connecticut River Basin are generally increased under future climate conditions, while the flow is reduced in the spring. At many locations, the seasonal peak flow is earlier and reduced in the future. Water temperature is increased under the future climate conditions throughout the year at most locations. The greatest increase at most, but not all, stations occurs in August and typically ranges between 3 and 5°C depending on location. Increases up to 6 degrees occur at a limited number of locations.

7.2 Future Work

The coarse modeling scale currently employed for national-scale assessments is inconsistent with current national data products such as 30 m digital elevation model (DEM), soils, and vegetation data required to represent key hydrologic processes at scales appropriate for this project. The structure and process representation in these models precludes the appropriate use of these current data products anywhere near their native scale; significant data aggregation is required for use by these models along with associated smoothing and loss of fidelity. This data/model discrepancy will increase dramatically as next-generation data come online. In addition, current national-scale approaches to routing flow and computing water temperatures are insufficient for evaluating operational and structural modifications of water and power systems at scales relevant for water quality analyses (e.g., 401 certification).

To address discrepancies between operational scales and streamflow assessment scales, we have ported the integrated DHSVM/MASS1 model to a high-performance computing environment and demonstrated the capability to model the entire Columbia River Basin at a 90 m spatial resolution. However, there remains additional opportunities to improve DHSVM/MASS1 model performance to meet operational needs:

- The parallel performance indicates that running DHSVM at the point of maximum speedup may not be ideal. Run time needs to be balanced with the availability and cost of computational resources. It may also be more efficient to simulate a case like the Columbia River basin in several large subbasins, particularly for calibration and validation. Once calibrated, the parameters could be used in a "production" simulation of the entire Columbia Basin.
- The way meteorological forcing was read and applied was the largest single obstacle to higher parallel performance. Reading the meteorological data in larger blocks, a day or month at a time, say, rather than one time step at a time, may reduce input time. Reading 2D map data in parallel, instead of through the root process, may also be a solution.
- Stream routing took a significant part of the total run time for the Columbia simulation. The choice to keep this a serial process, executed by all processes, may become a barrier with larger applications. Parallel methods to perform channel routing should be investigated in future work.
- We have used a straightforward and relatively simple domain decomposition scheme assuming that the simulation of each "active" cell has an equivalent computational cost. However, cells with snow have a higher computational cost than cells without snow. Decomposition based on actual computational cost may significantly increase computational efficiency.

Climate-induced hazards, such as wildfire, will also impact operations through significant changes in vegetation and soil properties that directly impact snowpack, runoff, streamflow, and the delivery of eroded sediment and debris to downstream reservoirs. Standard vegetation data sets are only updated every few years while modern remote-sensing platforms and methodologies may provide a high-spatiotemporal surface characterization of physical spatial and temporal hydrologic parameters. In the near future, it should be possible to use a new generation of satellite sensors and machine learning methods to produce high-fidelity observational hydrologic parameters. Utilization of these evolving data production should be given a high priority to provide the most current updates to relevant biophysical models.

Model validation in this and most studies were limited to measurements of streamflow, water temperature, and SWE at an extremely limited number of locations. Of particular importance is the growing ability for data assimilation of evolving remotely sensed products, such as (30m) LIDAR estimates of snow depth, at their native scales without having to aggregate and lose important spatial information. For example, some utilities in California are currently using ultra-high-resolution NASA/JPL airborne snow data (3–50m) to estimate snowpack water storage.

Atmospheric Rivers (ARs) have a significant impact on hydrologic processes in many basins in the western U.S. through extreme precipitation and changes to the near-surface energy balance. We found ARs provide useful predictability of extreme precipitation occurrence and magnitude in western U.S. watersheds. To improve prediction skill, those AR-tracking algorithms with higher Integrated Vapor Transport (IVT) thresholds should be considered. We found that, in general, weak ARs (short duration and low intensity) account for 50–60% of all AR events, but they are weakly correlated with extreme precipitation. Future studies should prioritize the intense or prolonged AR events to improve the prediction skills of these events and investigate their meteorological, hydrological, and societal impacts.

Regional climate models such as WRF provide the necessary information to drive physics-based spatially distributed hydrologic models such as the DHSVM. However, we found it necessary to correct the raw WRF meteorological data for biases in precipitation and air temperature to better match observations. The remaining parameters (e.g., humidity, solar radiation, etc.) were unadjusted, to a certain extent physically decoupling them from the altered precipitation and air temperature. These corrections developed based on historical conditions, by necessity, were assumed to apply under future climate conditions, thereby reducing some of the perceived advantages in dynamical downscaling over statistical downscaling.

There are a limited number of meteorological observations whose distribution is often dictated by ease of access for installation and maintenance (hence, few in snow-dominated mountainous locations). Many of these stations only measure daily rainfall (snowfall is notoriously difficult to measure) and maximum/minimum air temperature. Some locations measure additional variables such as humidity, wind, and solar radiation at relatively fine time intervals – many fewer stations measure incoming longwave radiation, a key component of the energy budget. Hydrologic studies without the benefit of RCM data are forced to interpolate or extrapolate required data and estimate key meteorologic information (e.g., longwave radiation) from the available parameters that were measured. This lack of data also limits the ability to inform statistical downscaling methods and improve process representation and validation of dynamic downscaling.

To maximize the use of existing data for improved hydrologic modeling, there is a need to further test and improve physics-based methods to estimate the full suite of energy-balance input parameters from limited datasets. Many of the existing methods are location-specific and developed using a limited number of years. Much of the required data are likely being collected in experimental watersheds, or related flux measurement programs such as the AmeriFlux network. It would be necessary to complete a comprehensive inventory of available data and look for gaps in spatial coverage that could be filled with additional data collection.

8.0 References

Abatzoglou, J.T., Brown, T.J., 2012. A comparison of statistical downscaling methods suited for wildfire applications. Int. J. Climatol. 32, 772–780. https://doi.org/10.1002/joc.2312

Adriance, A., Pantoja, M., Lupo, C., 2019. Acceleration of Hydrology Simulations Using DHSVM for Multi-thousand Runs and Uncertainty Assessment, in: Meneses, E., Castro, H., Barrios Herna´ndez, C.J., Ramos-Pollan, R. (Eds.), High Performance Computing, Springer International Publishing. pp. 179–193.

Bales, R.C., Molotch, N.P., Painter, T.H., Dettinger, M.D., Rice, R., Dozier, J., 2006. Mountain hydrology of the western United States. Water Resour. Res. 42, W08432. https://doi.org/10.1029/2005WR004387

Beckers, J., Smerdon, B., Wilson, M., 2009. Review of hydrologic models for forest management and climate change applications in British Columbia and Alberta, FORREX Series 25. Forum for Research and Extension in Natural Resources Society, Kamloops, British Columbia, Canada.

Bellgraph, B., Perkins, W.A., Richmond, M.C., Serkowski, J.A., Harding, S.F., 2016. Lake Roosevelt White Sturgeon Modeling Support. Technical Report PNNL-26056. Pacific Northwest National Laboratory. Richland, WA.

Bonneville Power Administration (BPA) (2017). No Regulation No Irrigation flows (1929 – 2008). Available online at: https://www.bpa.gov/p/Power-Products/Historical-Streamflow-Data/Pages/No-Regulation-No-Irrigation-Data.aspx

Carrayrou, J., Mose´, R., Behra, P., 2004. Operator-splitting procedures for reactive transport and comparison of mass balance errors. Journal of Contaminant Hydrology 68, 239–268. doi:10.1016/S0169-7722(03)00141-4.

Cao Q, N Sun, J Yearsley, B Nijssen, and DP Lettenmaier. 2016. "Climate and Land Cover Effects on the Temperature of Puget Sound Streams." Hydrological Processes 30(13):2286-2304. DOI: 10.1002/hyp.10784 https://dx.doi.org/0.1002/hyp.10784

Chen, X., Leung, L.R., Gao, Y., Liu, Y., Wigmosta, M., Richmond, M., 2018. Predictability of Extreme Precipitation in Western U.S. Watersheds Based on Atmospheric River Occurrence, Intensity, and Duration. Geophys. Res. Lett. 45, 11,693-11,701. https://doi.org/10.1029/2018GL079831

Chen, X., Leung, L.R., Wigmosta, M., Richmond, M., 2019. Impact of Atmospheric Rivers on Surface Hydrological Processes in Western U.S. Watersheds. J. Geophys. Res. Atmos. 124, 8896–8916. https://doi.org/10.1029/2019JD030468

Chow, V., 1959. Open Channel Hydraulics. McGraw-Hill.

Cristea, N.C., J.D. Lundquist, S. P. Loheide II, C.S. Lowry, and C.E. Moore, Modelling how vegetation cover affects climate change impacts on streamflow timing and magnitude in the snowmelt dominated upper Tuolumne Basin, Sierra Nevada, *Hydrol. Process*. 28, 3896–3918 (2014) DOI: 10.1002/hyp.9909

Connecticut General Assembly (CGA). 2021. Chapter 494, Connecticut River Atlantic Salmon Compact, Sec. 26-302. Available: https://www.cga.ct.gov/current/pub/chap_494.htm

Cox, M.M., Bolte, J.P., 2007. A spatially explicit network-based model for estimating stream temperature distribution. Environmental Modelling & Software 22, 502–514. doi:10.1016/j.envsoft.2006.02.011.

Cunge, J.A., F.M. Holly, J., Verwey, A., 1980. Practical Aspects of Computational Hydraulics. Pitman Advanced Publishing Program.

Cuo L, DP Lettenmaier, M Alberti, and JE Richey. 2009. "Effects of a Century of Land Cover and Climate Change on the Hydrology of the Puget Sound Basin." Hydrological Processes 23(6):907-933. DOI: 10.1002/hyp.7228 https://onlinelibrary.wiley.com/doi/pdfdirect/10.1002/hyp.7228?download=true

Dagum, L., Menon, R., 1998. OpenMP: An Industry-Standard API for Shared-Memory Programming. IEEE Comput. Sci. Eng. 5, 46–55. doi:10.1109/99.660313.

Daly, C., Halbleib, M., Smith, J. I., Gibson, W. P., Doggett, M. K., Taylor, G. H., et al. (2008). Physiographically sensitive mapping of cli- matological temperature and precipitation across the conterminous United States. *International Journal of Climatology*, *28*(15), 2031–2064. https://doi.org/10.1002/joc.1688

Dinan, J., Balaji, P., Hammond, J.R., Krishnamoorthy, S., Tipparaju, V., 2012. Supporting the global arrays PGAS model using MPI one-sided communication, in: 2012 IEEE 26th International Parallel and Distributed Processing Symposium, IEEE, Shanghai, China. pp. 739–750. doi:10.1109/IPDPS.2012.72.

Edinger, J.E., Brady, D.K., Geyer, J.C., 1974. Heat Exchange and Transport in the Environment. Publication No. 74-049-00-3. Electric Power Research Institute (EPRI). Palo Alto, CA.

DOE (U.S. Department of Energy), 2013. Effects of Climate Change on Federal Hydropower, U.S. Department of Energy Report to Congress, August, 2013

Elliot, J.M. 1991.Tolerance and resistance to thermal stress in juvenile Atlantic salmon, Salmo salar. Freshwater Biology 25:61–70.

Elsner, M.M., L.C. Cuo, N. Voisin, J.S. Deems, A.F. Hamlet, J.A. Vano, K.E.B. Mickelson, S-Y Lee, and D.P. Lettenmaier. 2010. Implications of 21st century climate change for the hydrology of Washington State, Climatic Change, (102) 225-260.

Frans, C., Istanbulluoglu, E., Lettenmaier, D. P., Fountain, A. G., & Riedel, J. (2018). Glacier recession and the response of summer streamflow in the Pacific Northwest United States, 1960–2099.Water Resources Research, 54,6202–6225. https://doi.org/10.1029/2017WR021764Received 1 SEP 2017Accepted 9 AUG 2018Accepted article online 16 AUG 2018Published online 10 SEP 2018©2018. American Geophysical Union. All Rights Reserved.

Frans, C., Istanbulluoglu, E., Lettenmaier, D. P., Clarke, G., Bohn, T. J., & Stumbaugh , M. (2016). Implications of decadal to century scale glacio-hydrological change for water resources of the Hood River basin, OR, USA. Hydrological Processes, 30(23), 4314 –4329

Fread, D.L., Jin, M., Lewis, J.M., 1996. An LPI Numerical Implicit Solution for Unsteady Mixed-Flow Simulation, in: North American Water and Environment Congress & Destructive Water, ASCE. pp. 322–327.

Gao, Y., Lu, J., Leung, L. R., Yang, Q., Hagos, S., and Qian, Y. (2015). Dynamical and thermodynamical modulations on future changes of landfalling atmospheric rivers over western North America. Geophysical Research Letters, 42(17), 7179–7186. https://doi.org/10.1002/2015GL065435

Gelaro, R., McCarty, W., Suárez, M. J., Todling, R., Molod, A., Takacs, L., et al. (2017). The Modern‐Era Retrospective Analysis for Research and Applications, version 2 (MERRA‐2). Journal of Climate, 30(14), 5419‐5454. https://doi.org/10.1175/JCLI‐D‐16‐0758.1

Goniea, T.M., M.L. Keefer, T.C. Bjornn, C.A. Peery, D.H. Bennett, and L.C. Stuehrenberg. 2011. Behavioral thermoregulation and slowed migration by adult Fall Chinook salmon in response to high Columbia River water temperatures. Transactions of the American Fisheries Society 135.

Gupta, A.D., Lake, L.W., Pope, G.A., Sepehrnoori, K.T.U., King, M.J.B.R., 1991. High-resolution monotonic schemes for reservoir fluid flow simulation. In Situ; (United States) 15:3.

Hayes, D.B., B.J. Bellgraph, B.M. Roth, D.D. Dauble, and R.P. Mueller. 2013. Timing of redd construction by fall Chinook salmon in the Hanford Reach of the Columbia River. River Research and Applications 30:1110–1119.

Hawkins, E., Sutton, R., 2009. The Potential to Narrow Uncertainty in Regional Climate Predictions. Bull. Am. Meteorol. Soc. 90, 1095–1108. https://doi.org/10.1175/2009BAMS2607.1

Hungerford, R.D., Nemani, R.R. ,Running, S.W., Coughlan, J.C., 1989. MTCLIM: a mountain microclimate simulation model. U.S. Forest Service Intermountain Research Station Research Paper Int-414. Ogden, UT

Hwang, H.T., Park, Y.J., Sudicky, E.A., Forsyth, P.A., 2014. A parallel computational framework to solve flow and transport in integrated surface–subsurface hydrologic systems. Environmental Modelling & Software 61, 39–58. doi:10.1016/ j.envsoft.2014.06.024.

Julian, D.W., J.T. Hickey, W.L. Fields, L. Ostadrahimi, K.M. Maher, T.G. Barker, C.L. Hatfield, K. Lutz, C.O. Marks, S. Sandoval-Solis, and J.R. Lund. 2015. Decision Support System for Water and Environmental Resources in the Connecticut River Basin. Journal of Water Resources Planning and Management 142(1).

Kennedy, K., K. Lutz, C. Hatfield, L. Martin, T. Barker, R. Palmer, L. Detwiler, J. Anleitner, J. Hickey. 2018. The Connecticut River Flow Restoration Study: A watershed-scale assessment of the potential for flow restoration through dam re-operation. The Nature Conservancy, U.S. Army Corps of Engineers, and University of Massachusetts Amherst. Northampton, MA. Available: http://nature.org/ctriverwatershed

Kumar, M., Duffy, C.J., 2016. Exploring the role of domain partitioning on efficiency of parallel distributed hydrologic model simulations. Journal of Hydrogeology & Hydrologic Engineering 2015. doi:10.4172/2325-9647.1000119.

Lettenmaier, D.P., Alsdorf, D., Dozier, J., Huffman, G.J., Pan, M., Wood, E.F., 2015. Inroads of remote sensing into hydrologic science during the WRR era. Water Re- sources Research 51, 7309–7342. doi:10.1002/2015WR017616.

Leung LR, and MS Wigmosta. 1999. "Potential Climate Change Impacts on Mountain Watersheds in the Pacific Northwest." JAWRA Journal of the American Water Resources Association 35(6):1463-1471. DOI: 10.1111/j.1752-1688.1999.tb04230.x https://onlinelibrary.wiley.com/doi/abs/10.1111/j.1752-1688.1999.tb04230.x

Li, H.Y., Leung, L.R., Tesfa, T., Voisin, N., Hejazi, M., Liu, L., Liu, Y., Rice, J., Wu, H., Yang, X., 2015. Modeling stream temperature in the Anthropocene: An earth system modeling approach. Journal of Advances in Modeling Earth Systems 7, 1661–1679. doi:10.1002/2015MS000471.

Liggett, J.A., Cunge, J.A., 1975. Numerical Methods of Solution of the Unsteady Flow Equations, in: Unsteady Flow in Open Channels. volume 1, pp. 69–182.

Liu, J., Zhu, A.X., Liu, Y., Zhu, T., Qin, C.Z., 2014. A layered approach to parallel computing for spatially distributed hydrological modeling. Environmental Modelling & Software 51, 221–227. doi:10.1016/j.envsoft.2013.10.005.

Liu, J., Zhu, A.X., Qin, C.Z., Wu, H., Jiang, J., 2016. A two-level parallelization method for distributed hydrological models. Environmental Modelling & Software 80, 175–184. doi:10.1016/j.envsoft.2016.02.032.

Livneh, B., Rosenberg, E.A., Lin, C., Nijssen, B., Mishra, V., Andreadis, K.M., Maurer, E.P., Lettenmaier, D.P., Wood, A.W., Adam, J.C., Lettenmaier, D.P., Nijssen, B., 2013. A Long-Term Hydrologically Based Dataset of Land Surface Fluxes and States for the Conterminous United States: Update and Extensions. J. Clim. 26, 9384–9392. https://doi.org/10.1175/JCLI-D-12-00508.1

Livneh B, JS Deems, B Buma, JJ Barsugli, D Schneider, NP Molotch, K Wolter, and CA Wessman. 2015. "Catchment Response to Bark Beetle Outbreak and Dust-on-Snow in the Colorado Rocky Mountains." Journal of Hydrology 523:196-210. DOI: 10.1016/j.jhydrol.2015.01.039 https://dx.doi.org/10.1016/j.jhydrol.2015.01.039

Manojkumar, K., Palmer, B., Vishnu, A., Krishnamoorthy, S., Daily, J., Chavarria, D., 2012. The Global Arrays User Manual. Technical Report PNNL-13130. Pacific Northwest National Laboratory. Richland, WA.

Mantua N, Tohver I, Hamlet A.F., 2010. Climate change impacts on streamflow extremes and summertime stream temperature and their possible consequences for freshwater salmon habitat in Washington State, Climatic Change, 102(1-2) 187-223DOI: 10.1007/s10584-010-9845-2.

McMichael, G.A., Richmond, M.C., Perkins, W.A., Skalski, J.R., Buchanan, R.A., Vucelick, J.A., Hockersmith, E.E., Beckman, B.R., Westhagen, P.N., Ham, K.D., Welch, I.D., Bellgraph, B.J., Titzler, P.S., Sandford, B.P., 2008. Lower Monumental Reservoir Juvenile Fall Chinook Salmon Behavior Studies, 2007. PNWD-3959. Battelle-Pacific Northwest Division. Richland, WA.

Mearns, L.O., Sain, S., Leung, L.R., Bukovsky, M.S., McGinnis, S., Biner, S., Caya, D., Arritt, R.W., Gutowski, W., Takle, E., Snyder, M., Jones, R.G., Nunes, A.M.B., Tucker, S., Herzmann, D., McDaniel, L., Sloan, L., 2013. Climate change projections of the North American Regional Climate Change Assessment Program (NARCCAP). Clim. Change 120, 965–975. https://doi.org/10.1007/s10584-013-0831-3.

Mesinger, F., DiMego, G., Kalnay, E., Mitchell, K., Shafran, P. C., Ebisuzaki, W., et al. (2006). North American Regional Reanalysis. *Bulletin of the American Meteorological Society*, *87*(3), 343–360. https://doi.org/10.1175/BAMS-87-3-343

Mote, P.W. and E.P. Salathe Jr., 2010. Future climate in the Pacific Northwest, Climatic Change, (102) 29-50.

MPI Forum. 2018. Message Passing Interface (MPI) Forum Home Page. http://www.mpi-forum.org/ (Sept. 2018).

Naz, B.S., Kao, S.-C., Ashfaq, M., Rastogi, D., Mei, R., Bowling, L.C., 2016. Regional hydrologic response to climate change in the conterminous United States using high-resolution hydroclimate simulations. Glob. Planet. Change 143, 100–117. https://doi.org/10.1016/j.gloplacha.2016.06.003

Niehus, S.E., Perkins, W.A., Richmond, M.C., 2014. Simulation of Columbia River Hydrodynamics and Water Temperature from 1917 through 2011 in the Hanford Reach. Final Report PNWD-3278. Battelle-Pacific Northwest Division. Richland, Washington 99352. doi:10.13140/RG.2.1.5146.8409. prepared for Public Utility District No. 2 of Grant County.

Nieplocha, J., Palmer, B., Tipparaju, V., Krishnan, M., Trease, H., Apra`, E., 2006. Advances, applications and performance of the global arrays shared memory programming toolkit. The International Journal of High Performance Computing Applications 20, 203–231. doi:10.1177/1094342006064503.

O'Brien, T.A., M. F. Wehner,A. E. Payne,C. A. Shields,J. J. Rutz,L.-R. Leung,F. M. Ralph,A. Collow,I. Gorodetskaya,B. Guan,J. M. Lora,E. McClenny,K. M. Nardi,A. M. Ramos,R. Tomé,C. Sarangi,E. J. Shearer,P. A. Ullrich,C. Zarzycki,B. Loring,H. Huang,H. A. Inda-Díaz,A. M. Rhoades,Y. Zhou, 2021. Increases in Future AR Count and Size: Overview of the ARTMIP Tier 2 CMIP5/6 Experiment. JGR Atmospheres, https://doi.org/10.1029/2021JD036013.

Parr, D., G. Wang, and K.F. Ahmed. 2015. Hydrological changes in the U.S. Northeast using the Connecticut River Basin as a case study: Part 2. Projects of the future. Global and Planetary Change 133:167-175.

Perkins WA, Z Duan, N Sun, MS Wigmosta, MC Richmond, X Chen, and LR Leung. 2019. "Parallel Distributed Hydrology Soil Vegetation Model (DHSVM) using global arrays." *Environmental Modelling and Software*, doi.org/10.1016/j.envsoft.2019.104533.

Perkins, W., Richmond, M., Rakowski, C., Coleman, A., Guensch, G., 2002. Effects of Wanapum and Priest Rapids Impoundments on Columbia River Temperature. PNWD-3269.

Battelle Pacific Northwest Division. P.O. Box 999, Richland, Washington 99352. doi:10.13140/RG.2.1.3967.1920. prepared for Grant County Public Utility District.

Perkins, W.A., Richmond, M., 2001. Long-term, One-Dimensional Simulation of Lower Snake River Temperatures for Current and Unimpounded Conditions. Technical Report PNNL-13443. Pacific Northwest National Laboratory. P. O. Box 999, Richland, Washington, 99352.

Reclamation (2011), *SECURE Water Act Section 9503(c) – Reclamation Climate Change and Water, Report to Congress, 2011.*

Rice, R.J. 2019. Annual Costs of Wild Salmon Restoration Efforts in the Columbia River Basin. Capstone Project Paper, Department of Fisheries and Wildlife, Oregon State University, Corvallis, Oregon. 24 pp. Available: https://osu-wams-blogs-uploads.s3.amazonaws.com/blogs.dir/2961/files/2020/09/Rice-Capstone-Paper-Salmon-Restoration-Costs-2019.pdf

Richmond, M., Perkins, W., 2002. Regional scale simulation of water temperature variations in the Columbia river basin, in: Research and Extension Regional Water Quality Conference Program and Proceedings, Washington State University, Pull- man, Washington, February 20-21, Vancouver, Washington.

Richmond, M., Perkins, W., Chien, Y., 2000. Numerical Model Analysis of System- wide Dissolved Gas Abatement Alternatives. Technical Report PNWD-3245. Battelle Pacific Northwest Division. P.O. Box 999, Richland, Washington, 99352. Pre- pared for the U.S. Army Corps of Engineers, Walla Walla District under Contract DACW68-96-D-0002.

Richmond, M.C., Perkins, W.A., Chien, Y., 2002. Regional scale simulation of water temperature and dissolved gas variations in the Columbia river basin., in: Hydro-Vision 2002 Technical Papers, HCI Publications, Kansas City, Missouri, July 29 through August 2, Portland, Oregon.

Rupp, D. E., Abatzoglou, J. T., Hegewisch, K. C., and Mote, P. W. (2013). Evaluation of CMIP5 20th century climate simulations for the Pacific Northwest USA. Journal of Geophysical Research: Atmospheres, 118(19), 10,810-884,906. https://doi.org/10.1002/jgrd.50843

Shields, C. A., Rutz, J. J., Leung, L.-Y., Ralph, F. M., Wehner, M., Kawzenuk, B., et al. (2018). Atmospheric River Tracking Method Intercomparison Project (ARTMIP): Project goals and experimental design. *Geoscientific Model Development*, *11*(6), 2455–2474. https://doi.org/10.5194/gmd-11-2455-2018

Shirley, E.D., Lopes, V.L., 1991. Normal-Depth Calculations in Complex Channel Sections. Journal of Irrigation and Drainage Engineering 117, 220–232. doi:10. 1061/(ASCE)0733-9437(1991)117:2(220).

Shuai, P., Chen, X., Song, X., Hammond, G.E., Zachara, J., Royer, P., Ren, H., Perkins, W.A., Richmond, M.C., Huang, M., 2019. Dam Operations and Subsurface Hydro- geology Control Dynamics of Hydrologic Exchange Flows in a Regulated River Reach. Water Resources Research 55, 2593–2612. doi:10.1029/2018WR024193.

Simeone, B., 1986. An asymptotically exact polynomial algorithm for equipartition problems. Discrete Applied Mathematics 14, 283–293. doi:10.1016/ 0166-218X(86)90032-6.

Spear, M.C. and J.D. Kieffer. 2016. Critical thermal maxima and hematology for juvenile Atlantic (*Acipenser oxyrinchus* Mitchill 1815) and shortnose (*Acipenser brevirostrum* Lesueur, 1818) sturgeons. Journal of Applied Ichythyology 32:251–257.

Storck P, L Bowling, P Wetherbee, and D Lettenmaier. 1998. "Application of a GIS-Based Distributed Hydrology Model for Prediction of Forest Harvest Effects on Peak Stream Flow in the Pacific Northwest." Hydrological Processes 12(6):889-904.

Storck, P., and D. P. Lettenmaier, Predicting the effect of a forest canopy on ground snow accumulation and ablation in maritime climates, in Troendle, C, Ed., Proc. 67th Western Snow Conf, Colorado State University, Fort Collins, 1-12, 1999.

Sun, N., Wigmosta, M., Zhou, T., Lundquist, J., Dickerson-Lange, S., Cristea, N., 2018. Evaluating the functionality and streamflow impacts of explicitly modelling forest-snow interactions and canopy gaps in a distributed hydrologic model. Hydrol. Process. 32, 2128–2140. https://doi.org/10.1002/hyp.13150

Sun N, J Yearsley, M Baptiste, Q Cao, DP Lettenmaier, and B Nijssen. 2016. "A Spatially Distributed Model for Assessment of the Effects of Changing Land Use and Climate on Urban Stream Quality." Hydrological Processes 30(25):4779-4798. DOI: 10.1002/hyp.10964https://dx.doi.org/10.1002/hyp.10964

Sun N, J Yearsley, N Voisin, and DP Lettenmaier. 2015. "A Spatially Distributed Model for the Assessment of Land Use Impacts on Stream Temperature in Small Urban Watersheds." Hydrological Processes 29(10):2331-2345. DOI: 10.1002/hyp.10363 https://dx.doi.org/10.1002/hyp.10363

Taylor, K.E., Stouffer, R.J., Meehl, G.A., 2012. An Overview of CMIP5 and the Experiment Design. Bull. Am. Meteorol. Soc. 93, 485–498. https://doi.org/10.1175/BAMS-D-11-00094.1

Thyer M, J Beckers, D Spittlehouse, Y Alila, and R Winkler. 2004. "Diagnosing a Distributed Hydrologic Model for Two High-Elevation Forested Catchments Based on Detailed Stand- and Basin-Scale Data." Water Resources Research 40(1). DOI: 10.1029/2003wr002414 https://agupubs.onlinelibrary.wiley.com/doi/pdfdirect/10.1029/2003WR002414?download=true

Tiffan, K.F., Garland, R.D., Rondorf, D.W., 2002. Quantifying flow-dependent changes in subyearling fall chinook salmon rearing habitat using two-dimensional spatially explicit modeling. North American Journal of Fisheries Management 22, 713–726.

Tohver, I.M., A.F. Hamlet, S. Lee. 2014. Impacts of 21-st Century Climate Change on Hydrologic Extremes in the Pacific Northwest Region of North America. Journal of the American Water Resources Association 50:1461–1476.

U.S. Congress, 1940. United States Code: Federal Power Act, 16 U.S.C. §§ 791-825r. [Periodical] Retrieved from the Library of Congress, https://www.loc.gov/item/uscode1940-001016012/

Vivoni, E.R., Mascaro, G., Mniszewski, S., Fasel, P., Springer, E.P., Ivanov, V.Y., Bras, R.L., 2011. Real-world hydrologic assessment of a fully-distributed hydrological model in a parallel computing environment. Journal of Hydrology 409, 483–496. doi:10.1016/j.jhydrol.2011.08.053.

Wigmosta, M.S., Vail, L.W., Lettenmaier, D.P., 1994. A distributed hydrology-vegetation model for complex terrain. Water Resour. Res. 30, 1665–1679. https://doi.org/10.1029/94WR00436

Wigmosta, M.S., Storck, P., Lettenmaier, D.P., 2002. The distributed hydrology soil vegetation model, in: Mathematical Models of Small Watershed Hydrology and Ap- plications. Water Resource Publications, Littleton, CO, pp. 7–42.

Wigmosta, M.S., Lettenmaier, D.P., 1999. A comparison of simplified methods for routing topographically driven subsurface flow. Water Resources Research 35, 255– 264. doi:10.1029/1998WR900017.

Wilkinson, B., Allen, M., 1998. Parallel Programming: Techniques and Applications Using Networked Workstations and Parallel Computers. Prentice Hall.

Yan, H., Sun, N., Fullerton, A., Baerwalde, M., 2021. Greater vulnerability of snowmelt-fed river thermal regimes to a warming climate. Environmental Research Letters 161– 13. Doi: 10.1088/1748-9326/abf393.

Yearsley, J.R., Sun, N., Baptiste, M., Nijssen, B., 2019. Assessing the impacts of hydrologic and land use alterations on water temperature in the Farmington River basin in Connecticut. Hydrology and Earth System Sciences 23, 4491–4508. doi:10. 5194/hess-23-4491-2019. publisher: Copernicus GmbH.

Pacific Northwest National Laboratory

902 Battelle Boulevard
P.O. Box 999
Richland, WA 99354
1-888-375-PNNL (7665)

www.pnnl.gov